

1

ELECTRON SPECTROSCOPIC STUDIES
ON
METAL OXIDE VARISTORS

A Thesis
submitted to

THE UNIVERSITY OF POONA

for

The Degree of
DOCTOR OF PHILOSOPHY
In Physics

By

SUDHAKAR R. SAINKAR,
M. Sc.

Physical Chemistry Division
National Chemical Laboratory
Poona 411 008 (India).

*

1981

ACKNOWLEDGEMENT


I am greatly indebted to Dr. A.P.B. Sinha, F.N.A., Head, Physical Chemistry Division, National Chemical Laboratory, Pune, for suggesting this interesting research problem and for his inspiring guidance during the course of this investigation.

My sincere thanks are due to Dr. S. Badrinarayanan, Dr. S.K. Date and all my colleagues for their whole-hearted cooperation during the course of this work.

I am also thankful to my wife Shobha for her many sacrifices in returning to the life of a Ph.D. student's wife.

Finally, I am grateful to the Director, National Chemical Laboratory, Pune, India, for allowing me to submit this work in the form of a thesis.

Pune
December 1981


S. R. SAINKAR

C O N T E N T S

	Page No.
<u>CHAPTER - I : INTRODUCTION</u>	
<u>A. Varistor</u>	1
1.1 What is a varistor ?	1
1.2 Varistor characteristics	2
1.3 Applications	4
1.4 Different types of varistors	6
1.5 Review of literature on ZnO varistors	13
<u>B. Electron Spectroscopy</u>	24
1.1 History	25
1.2 Basic principles	28
1.3 Chemical shift	29
1.4 Escape depth	31
1.5 Satellite lines	32
1.6 Line broadening	34
1.7 Sample charging	35
Purpose of the present study	37
<u>CHAPTER - II : EXPERIMENTS AND TECHNIQUES</u>	
2.1 Preparation of samples	40
2.2 Measurements of the current-voltage characteristics	42

	Page No.
2.3 Electron spectrometer	43
2.4 Scanning electron microscope	60
2.5 Electron probe microanalysis using energy dispersive X-ray spectrometer	65
2.6 X-ray diffractometer	71
 <u>CHAPTER - III : RESULTS AND DISCUSSION</u>	
3.1 ZnO + Bi ₂ O ₃ (ZB) varistor system	72
3.2 ZnO + Sb ₂ O ₃ (ZS) varistor system	91
3.3 ZnO + Bi ₂ O ₃ + CoO (ZBC) varistor system	106
3.4 ZnO + Bi ₂ O ₃ + Sb ₂ O ₃ + CoO + MnO + Cr ₂ O ₃ (ZBSCMCr) varistor system	124
 <u>REFERENCES</u>	 145
 <u>SUMMARY</u>	 157
 <u>APPENDIX - I</u>	
List of publications	164

CHAPTER - I : INTRODUCTION

A. VARISTOR

B. ELECTRON SPECTROSCOPY

A. VARISTORS

In recent years, studies of metal oxide type varistors have evoked keen interest in view of their wide applications in protecting electronic circuits and components. These varistors are not only economical but also easy to fabricate into suitable shapes and sizes for their applications in different circuits.

1.1 WHAT IS A VARISTOR ?

The varistor is a resistor, whose resistance is a function of the applied voltage. At low applied voltage, the varistor looks like an open circuit, so it blocks the current flow. At voltages above a certain value, its resistance decreases which enables a large current to flow, whereby the varistor effectively becomes short-circuited. A varistor is thus a voltage dependent resistor (VDR).

Metal oxide varistor is a two electrode zinc oxide based ceramic semiconductor device, with a highly non-linear current-voltage characteristic similar to back-to-back Zener diodes, but with much greater current and energy handling capabilities.

1.2 VARISTOR CHARACTERISTICS

1.2.1 I-V Characteristics

The most important property for a varistor is its non-linear current-voltage characteristic, which has the form shown in fig. 1.1. It is clearly seen from the graph, that at low applied voltages, the variation in the current is linear (ohmic) similar to any linear resistor, but at high voltages it becomes non-linear (non-ohmic). This non-linear current-voltage characteristic of a varistor is expressed by the following empirical equation, similar to that for the silicon carbide varistors [1] :

$$I = \left(\frac{V}{C} \right)^\alpha \quad \dots\dots (1.1)$$

where V is the voltage across the varistor body, I is the current flowing through the body, C is a constant corresponding to the non-linear resistance and is defined by a voltage per unit length (V/mm) when 1 mA/cm² of current flows through the body, α is a non-linear exponent.

The equation (1.1) may also be written as,

$$I = K.V^\alpha \quad \dots\dots (1.2)$$

$$\text{or } V = C.I^{\frac{1}{\alpha}} \quad \dots\dots (1.3)$$

$$\text{where } K = \frac{1}{C^\alpha} \quad \text{and} \quad \alpha = \frac{1}{\beta}$$

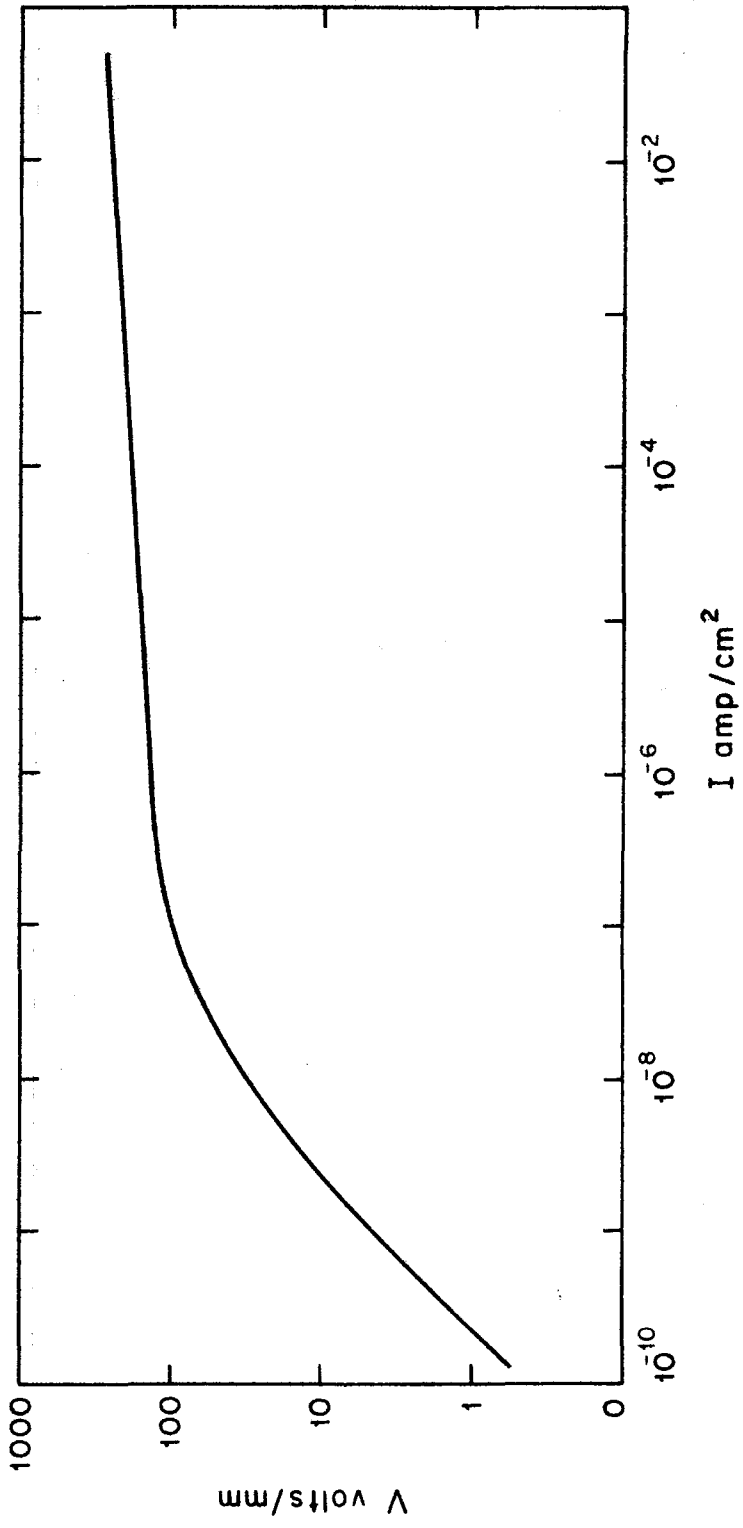


FIG. 1.1 : TYPICAL I-V CHARACTERISTICS OF A VARISTOR.

where β is equal to the slope of the voltage-current characteristic when plotted using logarithmic scales. Either α or β can be used to indicate the non-linearity coefficient, however since the metal oxide varistors have large α values it is customary to use α . If the voltage and current characteristics of a varistor are known at two points, α can be determined from the equation :

$$\alpha = \log_{10} (I_2/I_1) / \log_{10} (V_2/V_1) \quad \dots (1.4)$$

where V_1 and V_2 are the voltages at the currents I_1 and I_2 respectively.

1.2.2 Resistance of a Varistor

From Ohm's law, the resistance of a varistor is given by

$$R = \frac{V}{I} = \frac{V}{K.V^\alpha} = \frac{1}{K.V^{\alpha-1}} \quad \dots (1.5)$$

or using equation (1.3)

$$R = \frac{V}{I} = \frac{C.I^\beta}{I} = \frac{C}{I^{1-\beta}} \quad \dots (1.6)$$

From these equations, it is evident that the resistance value of a varistor is not constant, but depends on the values of voltage and current.

1.2.3 Power Dissipation

The power dissipation in varistor is given by

$$W = V.I = V.K.V^\alpha = K.V^{\alpha+1} \quad \dots\dots (1.7)$$

1.3 APPLICATIONS

This non-linear voltage-current characteristic found in the varistor has been responsible for its applications in the field of electronics.

Diener [2] of Bell Laboratories first used the varistors in telephone sets. Here they serve as equalizers to compensate for differences of transmission and reception levels caused by different lengths of lines.

Proost et al. [3] showed that varistors give good results when protecting the contacts of relays for making and breaking inductive circuits. When the contacts open, the energy stored in the inductance of the relays is dissipated in the varistor and the voltage across the contacts is limited to a safe value (fig. 1.2).

Uno [4,5] has used the varistor as a phase shift resistor in a phase shift oscillator circuit, where the frequency of the oscillator can be controlled by the magnitude

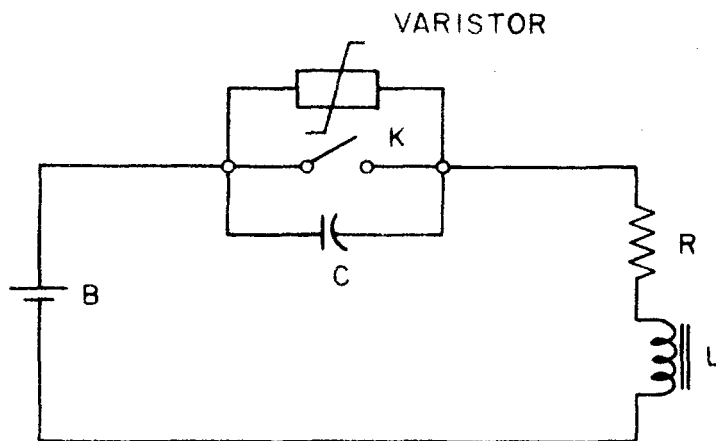


FIG. 1-2 : THE USE OF VARISTOR TO SUPPRESS SPARKS IN CONTACTS OF RELAYS .

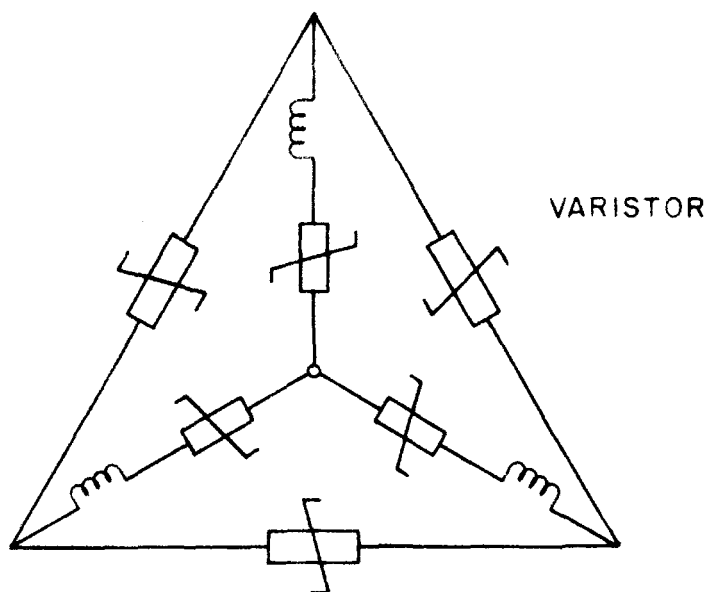


FIG. 1-3 : UTILIZATION OF VARISTORS IN A MICROMOTOR .

of the voltage applied to the varistor.

Lamb et al. [6] has used a varistor-network in a function generator circuit.

A typical application for quenching sparks is one for micromotors. The sparking brush contacts in a small battery operated motor, limit the commutator life and also cause interference. A varistor in parallel with each rotor winding prevents sparking, eliminates interference and increases the commutator life. Varistors for micromotors are manufactured in a three pole configuration (fig. 1.3) so that they can be easily mounted on the commutators of micromotors. Varistors are used in large quantities in tape recorders for micromotor noise absorption.

Varistors are also used in television receiving circuit for peak voltage limitation, oscillation damping, rectification to obtain a negative voltage for stabilizing the picture width and the e.h.t. against supply voltage variations and against ageing of tubes.

When a step-down transformer is switched on, it can impress severe transients on any components connected to its secondary winding due to its interwinding capacitance. Installing a varistor across the secondary winding (fig. 1.4) can eliminate this start up transient.

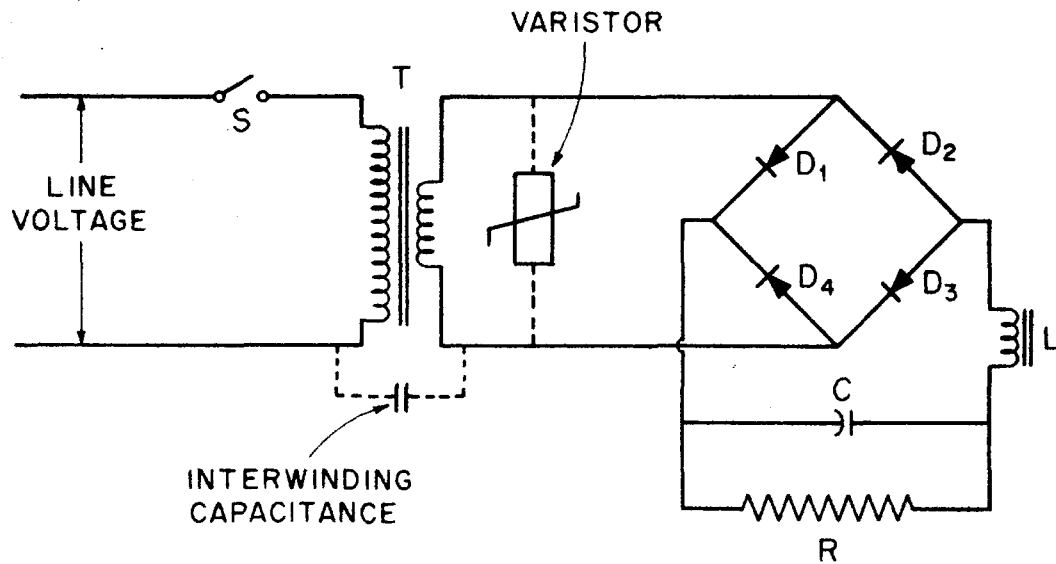


FIG. 1-4 : VARISTOR CAN ELIMINATE THE START - UP TRANSIENTS

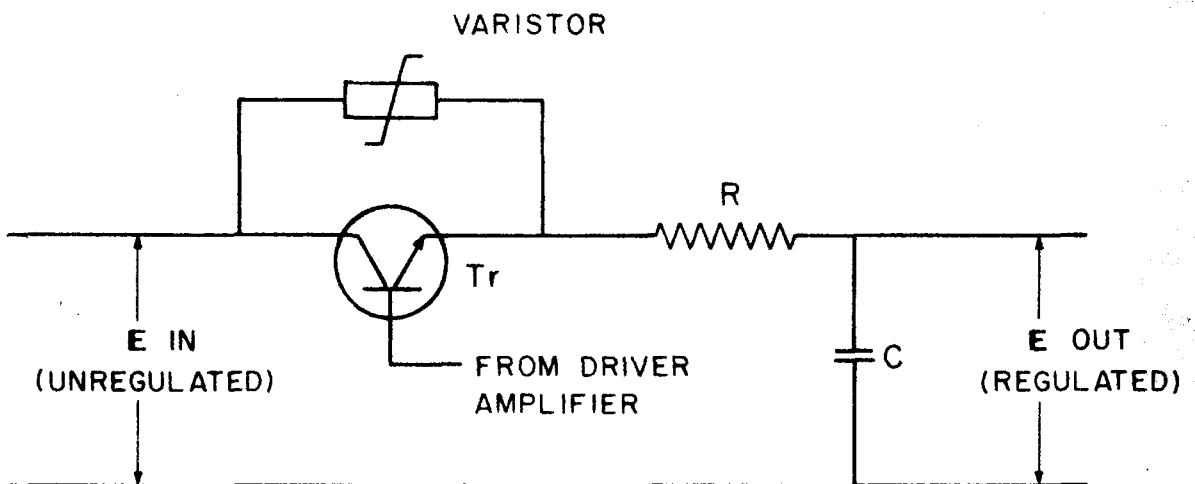


FIG. 1-5 : VARISTOR PROTECTS TRANSISTOR IN SERIES PASS VOLTAGE REGULATOR .

Another source of component failure which is sometimes overlooked can occur in the conventional transistor series pass voltage regulator circuit. When the circuit is turned on, the capacitor appears to be a short circuit, and the transistor is exposed to the full unregulated bus voltage. Placing a varistor across the transistor (fig. 5) allows a soft current rise to pass through the regulator without the usual surge.

1.4 DIFFERENT TYPES OF VARISTORS

Various kinds of varistors have been developed and it has been customary to identify varistors on the basis of the active material used, such as (1) silicon carbide varistors (SiC varistors), (2) selenium varistors (Se varistors), (3) silicon varistors (Si or zener diode varistors), (4) metal oxide varistors (MO or ZnO ceramic varistors).

The SiC and Se varistors were developed during the middle 50s while the metal oxide varistors were developed in the early 70s. These different varistors have different values of the non-linear exponent ' α ' and different current and energy carrying capabilities. Out of these, the metal oxide varistors have the highest ' α ' and current and energy carrying capacity.

1.4.1 SiC Varistors

Frosch [1] of Bell Laboratories, first described a symmetrical variable resistor made of silicon carbide. This is a symmetrical device, in the sense that its current-voltage curve for one direction of the current flow is the same as that for the opposite direction. In other words silicon carbide varistor does not rectify. Such symmetrical varistors find many applications in different electronic circuits.

At very low currents, the silicon carbide varistor is ohmic. With increasing current the I-V characteristic becomes non-ohmic. At very high currents the behaviour becomes ohmic again.

The process for making silicon carbide varistors is like ceramic process. The raw materials used are silicon carbide, carbon in the form of the graphite, clay and water. The carbon content controls the varistor's I-V curve, resistance decreases as the carbon content is increased. Water, along with clay is used to make the matrix in which the silicon carbide granules are embedded. The clay also contributes to the electrical properties of the varistors in both chemical and physical ways. The chemical constituents of the clay determine its plasticity and hence adherence of the clay to the granules. Also, certain organic compounds in the clay

probably react with the silicon carbide, giving effects similar to those of the carbon. In the mixing stage, the four materials are combined into a homogeneous mixture by making a slurry and gradually evaporating the excess water. This leaves a coating of clay and carbon on the silicon carbide granules. The granular mixture is then pressed into disc of any desired thickness, often as thin as 0.5 mm. These discs are then fired at 1100-1250°C in an atmosphere containing equal parts of highly pure hydrogen and nitrogen. The discs are metallized by spraying copper or tin on to both the surfaces, leads are then soldered to these metallized surfaces. Finally, discs are vacuum impregnated with a silicone fluid.

A large scale utilization of silicon carbide varistors originated with their adoption as spark eliminator in the cross-bar exchange. Since then their popularity has increased along with electronic semiconductor device development. The demand for small size silicon carbide varistors has been increasing especially, for micromotor contact protection and noise absorption, which are used in car stereos and cassette tape recorders.

The silicon carbide varistor's non-linear exponent ' α ' is between 2-5 [1-6]. As the current electronic products

employ a large number of semiconductor devices like transistors, diodes and integrated circuits, it has become very important to utilize corrective devices for abnormal voltages. The silicon carbide varistor's non-linear exponent ' α ' is not large enough and its clamping voltage is too high, which means that it provides an unsatisfactory protection against abnormal voltages.

1.4.2 Selenium Varistors

The reverse characteristic of a selenium rectifier which is non-linear is utilized in selenium varistors. The non-linear exponent ' α ' is not large enough and their operating voltage is fairly low.

1.4.3 Si(Zener) Varistor

Zener [7] published a theory of excitation of electrons directly from the valence band to conduction band under the influence of high electric fields. McAfee et al. [8] measured the Zener current across a p-n junction formed in a silicon single crystal by using arsenic as the donor and gallium as acceptor impurity [9-11]. The slope of the $\log V$ versus $\log I$ plot for the junction was observed to be 24. The Zener diode is a superior non-ohmic resistor, which causes electric current to flow through the p-n junction at a critical voltage [12].

The Zener diode excels in regard to the non-linearity exponent but its surge-current absorption capacity is low.

These protecting devices have not therefore been capable of meeting abnormal voltage conditions experienced by rapidly developing electronic devices.

1.4.4 Metal Oxide Varistors

In 1968, M. Matsuoka discovered that the sintered ZnO-Bi₂O₃ metal oxide type ceramic varistor possessed excellent non-ohmic characteristics. From that time zinc oxide based ceramic varistors have gained prominence and research on this new metal oxide varistor is proceeding in a serious way.

These varistors offer the advantages of nanosecond switching speeds. They are of small size and are able to handle current surges of the order of hundreds of amperes. This new metal oxide varistor has a steep non-linear voltage-current characteristic that makes it useful in voltage regulation application. As its non-linearity exponent ' α ' is very much higher than that of the other varistors, it can pass widely varying currents over a narrow voltage range.

At low applied voltages, the metal oxide type varistor looks like an open circuit, because its unique two phase material assumes the properties of an insulator. When the

applied voltage exceeds the clamping voltage, the device effectively becomes a short circuit, protecting the component that it shunts. The metal oxide type varistor requires very little stand-by power, making it useful for guarding other semiconductor devices. Steady state power dissipation of the metal oxide type varistor is typically a fraction of a milliwatt, as compared to the hundreds of watts dissipated by some other varistor devices. In the case of a varistor, the higher the non-linear exponent ' α ', the lower will be the standby loss. For the silicon carbide varistor which has a typical α of 3, the necessary steady state dissipation will be 660 watts. On the other hand, a metal oxide type varistor with a non-linear exponent ' α ' of 30 will dissipate only 0.1 milliwatt.

In summary, the excellent characteristics of ZnO varistors, not found in the previously produced varistors, are :

- (1) non-linearity exponent ' α ' from 20 to 50.
- (2) 2500 A/cm² surge capacity.
- (3) voltage-temperature coefficient from 0.05 to 0.001 %/°C.
- (4) fast surge response time. A 0.5 μ sec. surge can be absorbed.
- (5) wide range of varistor voltages, from 20 volts to 50 K volts.

- (6) maximum energy handling capability: 0.2 to 44000 Joules.

Zinc oxide varistors are manufactured in a variety of sizes and constructed according to the requirements. Normally, disc type varistors are used for application below 1000 volts, and rod type varistors for applications over 5 KV, washer type varistors attached to heat sink are used for applications at higher energy levels.

Applications for zinc oxide ceramic varistors are :

- (1) TV and high voltage equipment stabilization.
- (2) stabilizing circuit voltages in home and industrial electronic products.
- (3) absorbing surges when heavy electric equipment is turned on and off.
- (4) protecting high voltage transformers and high voltage rectifiers.
- (5) protecting household electronic equipments, communication equipments and control devices.
- (6) protecting various kinds of semiconductor devices.
- (7) surge absorption for relays and switches.
- (8) protection from lightening surges.

Thus zinc oxide ceramic varistors can be utilized practically in every electrical device that requires the absorption of abnormal voltages for voltage stabilization.

To minimize the damaging of electronic and electrical equipments by mains-borne transients or internally generated spikes, now, the designer (instead of over specifying semiconductors or incorporating costly protection circuits) can use inexpensive and effective ZnO varistors. By using ZnO varistors, equipment designers are able to increase the reliability of their circuits and at the same time, reduce component costs by specifying semiconductors with more moderate ratings.

It is believed that the ZnO varistors will become the future norm for varistors.

1.5 REVIEW OF LITERATURE ON ZnO VARISTORS

Much of the information available on zinc oxide has been summarized in reviews by the New Jersey Zinc Company [13] and Heiland et al. [14]. The crystal structure of ZnO is hexagonal, analogous to the Wurtzite form of ZnS, it is an n-type semiconductor. The resistivity, which is typically $1 \Omega\text{-cm}$ at 25°C can be decreased by quenching from high

temperature. Doping with Na^+ ions introduces electron traps into the material, increasing the resistivity to the point where space charge limited current can be observed [15]. Non-linear conduction has also been reported for surface barriers formed on ZnO by Au and Pd contacts [16]. In general, monovalent ions (e.g. Li^+) tend to increase the resistivity of doped sintered polycrystalline ZnO by creating electron traps and trivalent ions (e.g. Al^{3+} and Cr^{3+}) tend to decrease it by supplying extra conduction electrons [17].

The effects of ambient atmosphere on the sintering of ZnO can also be interpreted in terms of interstitial Zn diffusion as the rate controlling step [18,19]. The addition of a trivalent dopant increases the concentration of conduction electrons and simultaneously reduces the equilibrium concentration of Zn interstitials, so that the increase in electrical conductivity is accompanied by a decrease in the Zn diffusion coefficient. Thus, the effect of mono and trivalent dopants can be seen in sintering kinetics [20] as well as surface catalytic activity [21]. However, it has been reported [22] that small additions of K_2O to ZnO inhibit grain growth; just the opposite of what is expected for a monovalent dopant.

Matsuoka et al. [23] first found the voltage non-linearity in zinc oxide ceramics doped with alkali earth metal

oxide. The usual semiconducting properties of zinc oxide have been studied by Hahn [24] and Harrison [25]. The cold-pressed bodies of zinc oxide powder with 0.5 mole % of alkali earth metal oxide additives (e.g. CaO, SrO, BaO, BeO, MgO) have been sintered in air at various temperatures from 950 to 1450°C for one hour. The voltage-current non-linearity coefficient ' α ' has been measured in accordance with the method described by Masuyama et al. [26].

The sintered ZnO pellets without or with BeO or MgO additives have $\alpha = 1$. Those with CaO, SrO or BaO additives however produce $\alpha > 1$. When the ionic radius of the dopant e.g. Be²⁺ and Mg²⁺ is smaller than that of Zn²⁺ then the product shows a linear voltage-current characteristic. On the other hand, additives having the ionic radius larger than that of Zn²⁺ produce non-linear voltage-current characteristics.

Electron photomicrograph shows that the sintered body with linear voltage-current characteristic has apparently no second phase segregated. Whereas the sintered body with $\alpha > 1$ has a second phase segregated at the grain boundaries. In view of general rule [27] that the solubility depends on the ionic radius, the added CaO, SrO or BaO should not dissolve in the ZnO lattice but should form a segregated phase.

It is believed that this segregated phase may be responsible for the observed non-linear characteristics.

Matsuoka et al. [23,29] have investigated the non-ohmic metal oxide type varistors made of zinc oxide ceramics with five additives of Bi_2O_3 , CoO , MnO , Sb_2O_3 , Cr_2O_3 and have found them to have non-ohmic property comparable to those of a Zener diode. The electron photo-micrograph and X-ray micro-analysis show that the five additives are combined together and are segregated at the grain boundaries during the sintering process. The electric resistivity and dielectric constant of segregation layers are estimated to be 10^{13} ohm-cm and 170 respectively. Based on the microstructure and voltage-current characteristics, a theory [30] on space-charge limited current of insulator having deep traps is discussed to explain the non-ohmic properties of zinc oxide ceramics.

The effect of single addition and combined addition of various oxides on non-linear resistance and average grain size has been studied. The sintering temperature has been also varied to find out the temperature at which the highest α -value is obtainable.

The single addition of Bi_2O_3 or Sb_2O_3 produces a low α -value of about 3-4 but a double addition such as $\text{Bi}_2\text{O}_3 + \text{CoO}$ or $\text{Bi}_2\text{O}_3 + \text{MnO}$ increases the α -value upto 18 at the highest.

An addition of three oxides of $\text{Bi}_2\text{O}_3 + \text{CoO} + \text{MnO}$ or four oxides of $\text{Bi}_2\text{O}_3 + \text{CoO} + \text{MnO} + \text{Cr}_2\text{O}_3$ further increases the α -value and an addition of five oxides of $\text{Bi}_2\text{O}_3 + \text{CoO} + \text{MnO} + \text{Cr}_2\text{O}_3 + \text{Sb}_2\text{O}_3$ produces the α -value of 50.

The chemical analysis and X-ray microanalysis has indicated that a single addition of 0.5 mole % of CoO , MnO or Cr_2O_3 dissolves in the ZnO grains and does not produce non-ohmic properties when sintered above 1250°C . A single addition of 0.5 mole % of Bi_2O_3 forms a segregation layer at the grain boundaries and produces non-ohmic properties when sintered at a temperature of 950° to 1250°C . Above 1250°C , the sintered body does not include Bi_2O_3 due to its evaporation and is in an ohmic state. ZnO ceramics with a single addition of 0.5 mole % of Sb_2O_3 becomes non-ohmic when sintered at a temperature of 950° to 1150°C but it changes to ohmic state above 1150°C due to the evaporation of Sb_2O_3 . The ZnO ceramics with a double addition of $\text{Bi}_2\text{O}_3 + \text{CoO}$ or $\text{Bi}_2\text{O}_3 + \text{MnO}$ show α -value of 13 or 18, higher than that for a single addition of Bi_2O_3 when sintered at a temperature of 1250°C or 1350°C . On the other hand, the ZnO ceramics with a single addition of Bi_2O_3 , CoO or MnO hardly show the non-ohmic properties when sintered at 1250°C or 1350°C . This fact suggests that a double addition of $\text{Bi}_2\text{O}_3 + \text{CoO}$ or $\text{Bi}_2\text{O}_3 + \text{MnO}$ forms a compound which prevents the evaporation

of Bi_2O_3 at 1250°C or 1350°C . Such an explanation has been supported by Levin et al. [31] who indicate the existence of a compound, $\text{Bi}_2\text{O}_3 \cdot 2\text{Mn}_2\text{O}_3$. The high α -value of five additions of $\text{Bi}_2\text{O}_3 + \text{CoO} + \text{MnO} + \text{Cr}_2\text{O}_3 + \text{Sb}_2\text{O}_3$ cannot be explained reasonably only by considering a mere integration of effects of individual oxides.

The effect of sintering temperature on the non-ohmic properties of ZnO ceramics with five additives, which showed the highest α -value, has been studied. The α -value increases as the sintering temperature rises upto a maximum value of 50 at 1350°C . When sintered above 1350°C , it decreases steeply with the increasing temperature and becomes unity at above 1450°C , the pellets having a low room temperature electrical resistivity of about 10 ohm-cm.

The effect of the concentration of five dopants on the α value has also been studied. An additive content less than 0.1 mole % does not produce the non-ohmic property, but causes a slight increase in the resistance. Above 0.1 mole %, the α -value increases steeply with the increase in the additive content reaching a maximum of about 50 at 3.0 mole %. After the maximum, it decreases with the increasing additive content. Thirty mole % of the additive gave α -value of about 4 only. A pure mixture of the five oxides did not produce the non-ohmic property.

Norris [32] has measured the non-linear voltage-current characteristics, the small signal ac capacitance and resistance of sintered ZnO containing 0.5 mole % Bi_2O_3 . The dielectric properties of similar sintered ceramics have been measured by Delaney et al. [33]. Levin et al. [34] have reported the most comprehensive data on phase equilibria in the ZnO- Bi_2O_3 binary system. In general, very little work has been reported on the electrical properties of Bi_2O_3 , although evaporated thin films were studied by Halford et al. [35].

Wong [36] has studied the intergranular phase in samples of sintered ZnO + 0.5 mole % Bi_2O_3 , after etching with dilute HClO_4 solution. The techniques used have been, electron diffraction, electron microscopy, microprobe analysis and X-ray diffraction. The studies have strongly indicated that the intergranular material is a polycrystalline phase of tetragonal β - Bi_2O_3 rather than the amorphous ZnO- Bi_2O_3 phase reported earlier [29,32]. A polycrystalline matrix of ZnO grains separated by thin layers of β - Bi_2O_3 , forms a series and parallel network of ZnO- Bi_2O_3 barriers. The intergranular barriers may be as thin as $< 500 \text{ \AA}$. From the known intrinsic electrical properties of ZnO [24,37] and Bi_2O_3 [38,39] the non-ohmic behaviour of this binary ceramic appears to arise from an interfacial property characteristic of ZnO, an n-type semiconductor ($\sim 1 \text{ ohm-cm}$ at room temperature) in contact with a thin layer of high resistivity ($> 10^8 \text{ ohm-cm}$) Bi_2O_3 as the intergranular phase.

Long [40] has studied the microstructure of a complex multi-component varistor ceramic based on ZnO with small additions of antimony, bismuth, cobalt, manganese and tin oxides, using a variety of structural techniques such as scanning electron and optical microscopes, Debye-Scherrer powder diffraction etc.

Three crystalline phases have been found to exist in a complex multicomponent varistor.

- (i) a polycrystalline bulk matrix of ZnO doped with Co^{2+}
- (ii) a II-V $\text{Zn}(\text{Zn}_{4/3}\text{Sb}_{2/3})\text{O}_4$ spinel doped with Co^{2+} and Mn^{2+}
- and (iii) an anion deficient pyrochlore $\text{Bi}_2\text{Zn}_{4/3}\text{Sb}_{2/3}\text{O}_6$ also doped with Co^{2+} and Mn^{2+} .

The spinel phase has been found frequently at grain boundaries and occasionally within the grains. The possibility that this material is the intergranular phase has been dismissed by the author on the grounds of its high interfacial energies with ZnO and its strong tendency to form a well-faceted octahedral crystals in the ceramic. It has been shown to play no role in the non-linearity characteristics of the varistor ceramic, but merely to act as a grain growth moderator for ZnO by anchoring the boundaries during

sintering. The pyrochlore is shown to segregate at the nodal regions between two or more ZnO grains and to form a three dimensional threadlike network that is indicative of a liquid phase at high temperature.

The concentration ratio of the spinel to pyrochlore is found to increase monotonically with sintering temperature so a pyrochlore to spinel transformation has been formulated by assuming a total replacement of the Bi_2O_3 content in the pyrochlore by an equivalent amount of ZnO that is readily available from the bulk matrix.

The overall structure has been described as a three-dimensional series-parallel network of ZnO-pyrochlore thin film barriers. The nature of this thin film is studied in detail by Wong [41].

Inada [42] has investigated the crystal phases in ZnO varistors containing Bi_2O_3 , Sb_2O_3 , Co_2O_3 , MnO_2 and Cr_2O_3 as a function of the amount of additives and the sintering temperature by X-ray diffraction analysis with a graphite crystal monochromator using CuK_α radiation.

These varistors consist of :

- (1) ZnO phase, dissolving a small amount of Co and Mn components,

- (2) spinel type phase of $Zn_7Sb_2O_{12}$, dissolving a large amount of Co, Mn and Cr components,
- (3) Bi-rich phases B, C, D or B', among which the B-phase is a δ - Bi_2O_3 type phase ($a = 5.59 \text{ \AA}$) having the composition, $12Bi_2O_3 \cdot Cr_2O_3$. The C phase is tetragonal phase ($a = 7.76 \text{ \AA}$, $c = 5.75 \text{ \AA}$) having the composition of $14Bi_2O_3 \cdot Cr_2O_7$ and dissolving Zn and Sb components. The D-phase is a β - Bi_2O_3 type phase ($a = 10.93 \text{ \AA}$, $c = 5.62 \text{ \AA}$) dissolving a large amount of Zn component (about 20 mole %) and a small amount of Sb component. The B'-phase is also a δ - Bi_2O_3 type phase ($a = 5.48 \text{ \AA}$) formed in the system Bi_2O_3 - ZnO - Sb_2O_3 , and a solid solution between B and B' is formed.

The non-linear exponent ' α ' increases with the changes of Bi-rich phases, B \rightarrow C \rightarrow D or D + B', by the rise in the sintering temperature.

Inada [43] has investigated the states of crystal phases in the non-ohmic zinc-oxide varistors with five additives, $0.5 Bi_2O_3 + 1.0 Sb_2O_3 + 0.5 Co_2O_3 + 0.5 MnO_2 + 0.5 Cr_2O_3$ (mole %) by various analytical techniques like scanning electron microscopy, X-ray microanalysis, electron microscopy, optical microscopy. The microstructure is shown to consist of ZnO phase dissolving Co and Mn; spinel phase of $Zn_7Sb_2O_{12}$ dissolving Co, Mn and Cr; and mixed

phases of β - and δ - Bi_2O_3 . Almost all grains of diameter of 10 to 20 microns correspond to the ZnO phase. Each of them is a single crystal, having a twinning structure. These structures are randomly oriented in the ceramics.

The spinel phase exists as grains of a few microns. These grains are discontinuously dotted in comparatively wide grain boundaries, where three or more ZnO grains meet.

Lda [44,45] has proposed a new energy-band model in the order to explain the non-ohmic property of a metal oxide varistor. A energy band model composed of a thin insulator with traps sandwiched between a forward-biased Schottky barrier and a reverse-biased Schottky barrier is proposed. The non-ohmic property of ZnO ceramics is mainly governed by the field emission for the reverse-biased Schottky barrier in the voltage region above the threshold voltage and by thermionic emission in the voltage region below the threshold voltage.

The physics of metal oxide varistors produced by the General Electric Company, U.S.A. under the trade name GE-MovTM has also been studied by Lionel et al. [46-49].

Beside this, there are many theoretical models [50-67] which have been proposed to explain the non-linear behaviour of ZnO varistors based on various mechanisms such as, charge

limited current process, Fowler-Nordheim tunneling process, tunneling across the Schottky barrier, transient conduction etc.

B. ELECTRON SPECTROSCOPY

In the past ten years, a large variety of surface characterization techniques have been developed and are described in many recent books and review articles [68-91]. Some of these surface characterizing techniques are relatively new and/or undeveloped and although they may give useful information concerning a surface, the interpretation of the data may be complex or the technique may be restricted to special class of materials.

Out of these, electron spectroscopy for chemical analysis (ESCA) or X-ray photoelectron spectroscopy (XPS), ultraviolet photoelectron spectroscopy (UPS), Auger electron spectroscopy (AES), secondary ions mass spectrometry (SIMS) are the more widely used surface techniques.

Electron spectroscopy (ESCA or XPS) involves the determination of the energy distribution of electrons emitted from X-ray irradiated substance. It is a non-destructive surface analysis technique, which produces directly the

electronic levels from the innermost to the outermost shells. Any element except hydrogen and helium can be studied even if it occurs together with several other elements. The utility of XPS has been two-fold. First, since the electronic energy levels of the atoms are sensitive to their environment, the technique is the best available for determination of chemical states of atoms and molecules. Secondly, from the photoelectron spectra, one can obtain the relative ratios of different elements or even of atoms of the same element in different environments.

The technique analyses only the first few angstroms of the solid surfaces. This is both good and bad. On the bad side, great care must be taken in sample preparation in order to keep the surface very clean. On the good side, this makes a sensitive technique for many important areas of research in various fields [92].

1.1 HISTORY

The two most important phenomena on which the technique of electron spectroscopy is based i.e. photoionization and the Auger process, were already understood earlier in the century. Einstein [93] in his classic paper, explained the photoelectric effect in 1905, while Pierre Auger [94] discovered the effect named after him in 1923. Between 1910

and 1930, Robinson [95] and de Broglie [96] used magnetic fields and photographic recording to determine the kinetic energies of photoelectrons ejected by X-ray absorption. The resolution attainable at that time was insufficient for observation of actual peaks in photoelectron spectra and therefore, the accuracy and precision of the measurement were far from adequate for the real surface analysis. Pioneering efforts in this field were carried out in 1951 by Steinhard and Serfass [97].

Present-day high resolution photoelectron spectroscopy, however, grew out of two parallel developments that took place principally in Uppsala, Sweden and the Imperial College, London. In Uppsala, the Swedish group headed by Prof. Kai Siegbahn [98] was interested in determining the binding energy for the atomic shells by X-ray photoelectron spectroscopy, whose values were known only approximately from the X-ray data. It was soon, discovered, that the chemical shift effects occurred, and a classic paper was published in 1958 [99] showing that the chemical difference between copper and its oxide was clearly distinguishable by X-ray photoelectron spectroscopy (XPS). Because of these observed and useful chemical effects, the Swedish group coined the name "Electron Spectroscopy for Chemical Analysis (in short, ESCA) to this X-ray photoelectron spectroscopy (XPS) technique.

Meanwhile, Turner and Al-Joboury in the Imperial College, London [100] were looking for a method of directly studying the binding energies of the molecular orbitals. Instead of X-rays as the photon source, which is the requirement for the study of core electrons, they chose the HeI resonance line as obtained in a helium gas discharge lamp. This radiation had enough energy (21.22 eV) to eject electrons from the outer orbitals (the ones which are usually the most important in determining the nature of the chemical band) with a natural line width of only a few millivolts. Since the days of these pioneering experiments the instrument design has been improved considerably with better sensitivity and resolution. In order to improve the resolution a very narrow X-ray beam has been designed for the X-ray monochromator [101, 102]. The sensitivity has been increased by a factor of 100 to 1000 times by modulating the intensity of the primary beam. The application of position sensitive detector [103], Vidicon [104], resistive strip [105] and various electrostatic electron energy analysers [106] have improved the resolution and sensitivity of the electron spectrometer.

With the rapid developments, both in technique and applications one can expect ESCA to rank among the top chemical research tools.

1.2 BASIC PRINCIPLES

The basic principle of X-ray photoelectron spectroscopy (XPS or ESCA) is extremely simple and is illustrated in fig. (1.6). The sample is irradiated with X-rays having fixed and definite energy $E_{h\nu}$ (characteristic X-rays of an anode material of the X-ray tube). The X-ray photons are absorbed by the sample atoms, with each absorption event resulting in the prompt emission of an electron.

If the sample is metallic and in good contact with the spectrometer, we may reasonably assume that the Fermi levels of the sample and the spectrometer material are the same. By convention, the binding energy of an electron is the energy required to raise the electron to the Fermi level.

The ejected electrons carry kinetic energy which is equal to the difference between the X-ray photon energy ($E_{h\nu}$) and the binding energy. Then the energy conservation for the photoemission process is given by the relation

$$E_{KE} = E_{h\nu} - E_{BE} - \phi_{Sp} \quad \dots\dots (1.8)$$

where E_{BE} is the binding energy of the electron in a particular level of the compound. E_{KE} is the kinetic energy of the ejected electron and ϕ_{Sp} is the work function of the spectrometer material. This work function ϕ_{Sp} does not

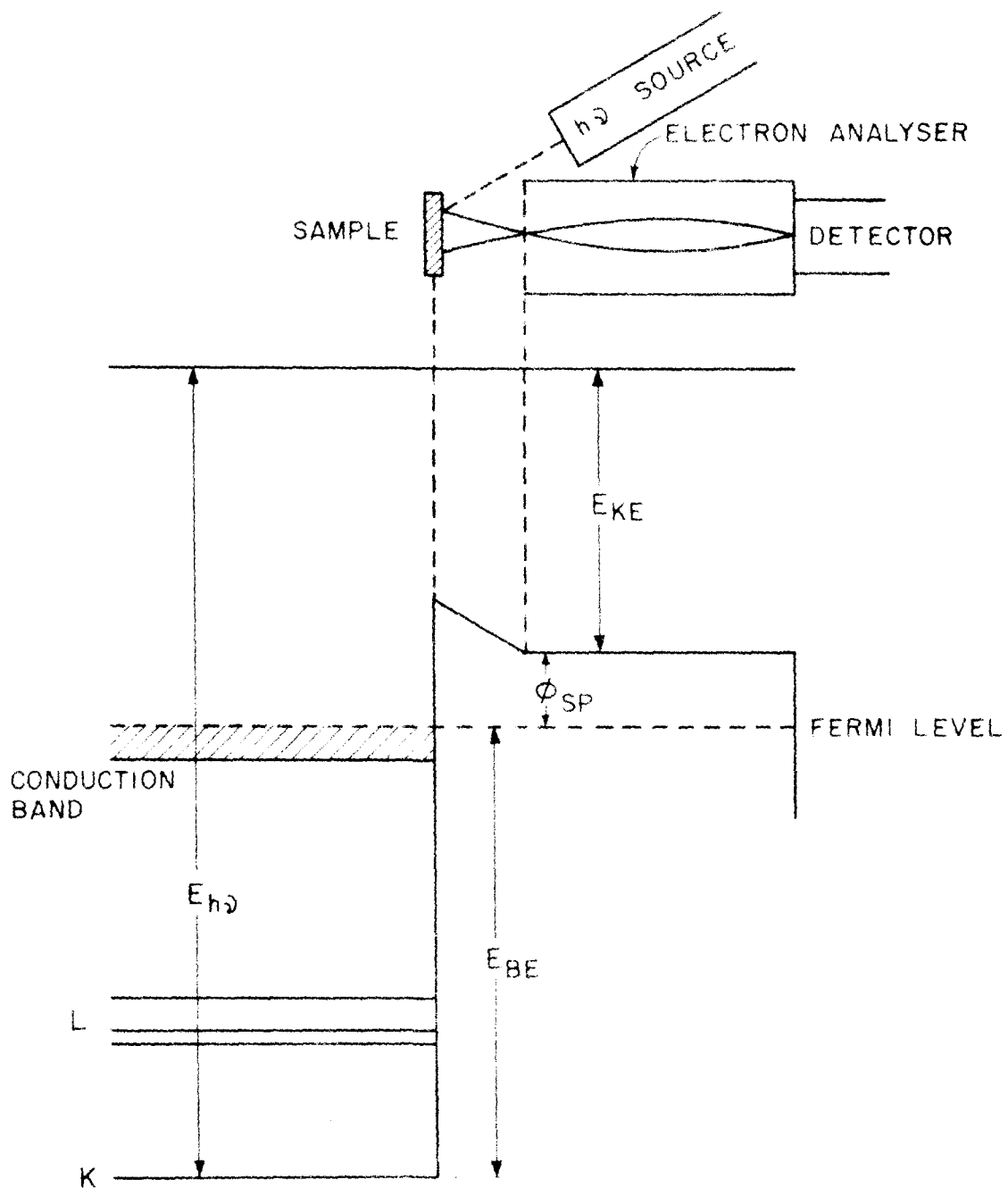


FIG. 1.6 : PRINCIPLES OF AN ELECTRON SPECTROMETER FOR A METALLIC SAMPLE WHICH IS IN GOOD CONTACT WITH THE SPECTROMETER (REF. 68)

depend on the sample material and as long as it does not vary with time, one and the same work function correction can be applied to all the measurements. If photon energy (usually 1253.6 eV and 1486.6 eV respectively for Mg and Al X-ray sources) is known and analyser work function ϕ_{sp} is predetermined, a plot of spectrum can be made of the number of the electrons $N(E)$ vs electron kinetic energies (E_{KE}). The binding energies (E_{BE}) are calculated using equation (1.8) and as binding energies of electrons of an atom are characteristic of the atom, a plot of binding energies against number of electrons is a sure way of identifying elements.

The qualitative information is provided by peak positions and quantitative information by their peak heights (area).

1.3 CHEMICAL SHIFT

The main value of X-ray photoelectron spectroscopy lies in the fact that the measured core electron binding energies are a function of chemical environment of the atoms. It was discovered that the binding energies of the orbital electron were dependent on the chemical environment [107,108]. When a bond is formed between two atoms, outer electronic shells coalesce into molecular shells called molecular

orbitals at different binding energies. These changes in binding energy called chemical shifts are carried uniformly from outer shells to innermost shells. So the potentials of the shells within an atom are shifted uniformly by the same amount, when a bond is formed. So these changes in binding energies which are known as chemical shifts enable one to distinguish atoms of the same type but occupying different chemical states within a molecule.

It was realized that the core binding energy of an atom should be related to the effective charge of the atom [68,109]. From the simple electrostatic considerations, one would expect that the energy for removing an electron from an atom would increase as the charge on the atom became more positive. Plots of the core binding energy for a given type of atom against estimated atomic charge show approximately linear correlations [68,110].

A great amount of effort has been spent for systematic investigations of binding energies for elements in related compounds in order to derive chemical shift data and has been compiled into tables [83,111,112].

The bulk of the published ESCA research in the last fifteen years has been directed toward understanding the systematic shift in peak positions resulting from changes in the chemical structure and oxidation state of chemical compounds.

1.4 ESCAPE DEPTH

As the X-ray normally used in XPS are the AlK_{α} or MgK_{α} X-rays (1486.6 eV and 1253.6 eV respectively), the photoelectrons have energies less than these amounts, and at these energies the mean free paths of the electrons are very short. Such electrons, travelling through a material, have a relatively high probability of experiencing inelastic collisions with locally bound electrons, as a result of which they suffer energy loss. These electrons coming out after collision, have a reduced kinetic energy, and such electrons contribute to the background. Electrons that come out without collision, obviously will be from the surface, electrons liberated from atoms deeper in the material will either lose their energy entirely in the material or will emerge out of the materials with a $E_{KE} < (h\nu - E_{BE})$.

Electron escape depth varies as a function of (i) electron kinetic energy and (ii) the type of material being examined [113,114].

For ESCA, the escape depth is about

- (i) 5-20 Å for metals
- (ii) 20-30 Å for inorganic compounds
- (iii) 50-100 Å for organic compounds.

1.5 SATELLITE LINES

The recorded photoelectron spectrum may contain satellite lines due to various phenomena such as multiplet splitting, electron shake up, configuration interaction and characteristic energy losses. It is most important to know the nature of these extra (satellite) photoelectron peaks both because we cannot interpret photoelectron spectra without this understanding and because the phenomena are in themselves of fundamental interest. In addition, these phenomena can be of extreme importance in learning about the nature of the chemical bonding.

1.5.1 Multiplet Splitting

When there are one or more electrons in the valence shell with unpaired spins, the act of photoionization in another shell of the same atom can lead to more than one final state, depending on the way in which the unfilled shells couple. Multiplet splitting is found generally in 3s (and 4s) peaks when unpaired electrons are present in 3d (and 4f) orbitals. The relative intensities of the 's' peaks, which appear as a doublet, will be the same for all shells and can be predicted from the number of unpaired spins in the valence shell. The degree of energy splitting decreases as the difference between the principal quantum number of the shell under consideration and that of the unfilled shell increases.

Vinikka et al. [115] correlated splitting of the 3s core levels in the ESCA spectra of transition metal compounds with increasing covalency of the metal-ligand bond. Similarly multiplet splitting in ESCA spectra has been studied for mixed nickel-iron and chromium oxide by Santibanez et al. [116] and the splitting of 4s and 5s levels of the rare earths by McFeely et al. [117-118].

1.5.2 Shake-up

Shake-up peaks are found on the low kinetic energy side of the core level peaks and arise from the two electron shake-up processes in which the valence-shell excitations take place in parallel with core electron ejection. Shake-up satellites have been observed for a number of transition metal compounds [119-123].

1.5.3 Configuration interaction

If the ion formed as a result of the photoionization process can be described by a wave function that includes excited configurations, then it is possible that the final state may end up as one of these excited states. Satellite structure from configuration interaction will usually occur only when photoionization takes place in the valence cell. These configuration interaction satellites have been observed for alkali metal halides by Wertheim et al. [124], for argon by Spears et al. [125] for neon by Wuilleumier et al. [126].

1.5.4 Characteristic energy losses

As an electron moves through matter it may suffer an inelastic collision. It will then appear in the spectrum with lower kinetic energy. The energy of the characteristic energy losses is dependent on the material. Its intensity depends on both the nature of the material and the kinetic energy of the electron passing through the material. Pollak et al. [127] have made a study of plasmon losses in metals using XPS.

1.6 LINE BROADENING

The most serious limitation to photoelectron spectroscopy of solids is the line broadening. This broadening results from three main sources:

- (i) Width of the photon source
- (ii) Width of the subshell from which the electron is photoejected and
- (iii) broadening due to charging.

(i) The width of UV source is negligible (1 meV) compared to AlK_{α} and MgK_{α} - X-ray source. The widths are due to the life time of the K-shell vacancy and due to spin-orbit splitting between the $2p_{1/2}$ - $2p_{3/2}$ levels. The net full-width at half maximum (FWHM) is about 0.9 eV for $AlK_{\alpha_{1,2}}$ and 0.8 eV

for $MgK_{\alpha_{1,2}}$. This source broadening can be overcome by use of a monochromator.

(ii) Line broadening occurs as a result of the finite lifetime of the vacancy created in the atom of the material under study. The lifetime decreases with an increase in binding energy. The broadening in the $2p_{3/2}$ level in silicon has been measured and found 0.5 eV by Siegbahn et al. [128].

(iii) For non-conducting solids one of the serious sources of line broadening is due to the uneven charging of the surface as a result of photoionization. This line broadening seriously affects the resolution of the electron spectrometer.

1.7 SAMPLE CHARGING

During the X-ray irradiation, non-conducting samples can acquire an excess positive charge at the surface due to the ejection photoelectrons, the conduction of the sample being inadequate to permit electrical equilibrium. In other words, the Fermi level of the sample may be lower than that of the spectrometer because of the electric charging. This positively charged sample surface retards the photoejected electrons. This decrease in the kinetic energy of ejected electrons results in higher apparent binding energies than

the true values and therefore limits the amount of chemical information obtainable from the data.

The error in the binding energy due to this effect can amount to many volts and varies with the X-ray flux and sample analyser chamber design. In most instruments, there are sufficient number of background electrons in the chamber to either neutralize the surface charge or stabilize it at a small value. However, there is a marked reduction in the number of background electrons when a monochromatized X-ray source is used and the charging effect can then be large.

Various techniques have been used to reduce or to eliminate this charging effect. In early work [63,110,129-131] the carbon 1s peak due to an organic film on the material or from the scotch tape used for mounting the sample was taken as a reference. Some other workers [132-134] have ground the sample with graphite (a fair electrical conductor) powder in order to provide a carbon 1s reference line in a standard material electrostatically equilibrated with the sample. Probably the most reliable method for providing a reference material with its Fermi level, the same as that of the sample, is to vacuum sputter a thin layer of metallic gold on the sample [135-142]. The gold adheres to the surface of the sample in small clumps or islands which are close enough

together to ensure that all regions of the sample are in electrostatic equilibrium with the gold and the gold $4f_{7/2}$ peak is used as a reference.

If in a series of compounds under study, there exists a common chemical group containing an atom which may reasonably be expected to have the same binding energy in all the compounds, one of the core level peaks for that atom may be used as an internal reference. Such internal references have been taken using the carbon 1s peak of ligands such as organophosphines [129] ethylenediamine [134] and benzoylacetonamine [143].

In some cases surfaces can be neutralized by using an auxiliary low energy electron source as a flood gun [144].

PURPOSE OF THE PRESENT STUDY

From the previously reported work, it is observed that the unusual non-ohmic property of the metal oxide varistor is attributable to the second phase segregated at the surface of the zinc oxide grains.

Several successful studies have been performed to detect the grain boundary segregation utilizing electron spectroscopy. ESCA was used in studies of grain boundary segregation of MgO doped Al_2O_3 [145]. Coad et al. [146]

recently observed segregation of manganese and antimony to grain boundaries of 0.12 % Sb and 2 % Mn steel. A careful examination of the Mn peak position suggested that the manganese was present as manganese sulfide or antimonide. Similarly Cu-Bi alloy, containing Cu-doped with 0.009 % of Bi was suitably heat treated and studied by ESCA. The ESCA results showed Bi segregation but no difference in the binding energies of segregated bismuth and elemental bismuth was found. Bishop et al. [147] have found out that the boron segregation to grain boundaries was partially responsible for high temperature fracture in steels containing boron.

Electron spectroscopy thus appeared to be a good technique to study the nature of the surface layers and their effect on the electronic properties of the varistor systems. One expects to identify the chemical nature, oxidation state, surface migration, grain boundary segregation etc. by means of a systematic electron spectroscopic study. X-ray photoelectron spectroscopy (XPS) is potentially capable of throwing light on such problems because the electrons ejected from only top surface layers reach the analyser. Further, XPS is also capable of showing any changes in the oxidation states of the ions involved. To the best of our knowledge, electron spectroscopic studies on ZnO varistor system have not been reported.

Although ZnO containing five additives gives a better non-linearity, it was considered desirable from the point of view of understanding, to start with a simpler system like ZnO containing a single additive and then to go over to the study of the more complicated five additives systems. We have therefore prepared samples belonging to four different varistor systems and investigated them by electron spectroscopy. Complementary studies by other techniques like scanning electron microscopy (SEM), electron probe micro analysis (EPMA) and X-ray diffraction (XRD) have also been conducted and these studies have revealed some interesting features of ZnO varistor systems. The details about the experimental techniques and results are discussed in the successive chapters.

CHAPTER - II : EXPERIMENTS AND TECHNIQUES

The metal oxide varistor samples studied in the present investigations consist mostly of zinc oxide along with additives such as bismuth oxide, antimony oxide, cobalt oxide, manganese oxide and chromium oxide. They have been prepared by the conventional ceramic fabrication procedure. Batches of pellets have been sintered at different temperatures from 600 to 1400°C for one hour. Sintered pellets have then been examined by different techniques, like electron spectroscopy (ESCA), scanning electron microscopy (SEM), electron probe microanalysis (EPMA) and X-ray diffraction (XRD). Electrical characteristic and density have also been measured.

The preparation and measurement procedures are given in detail in this chapter.

2.1 PREPARATION OF SAMPLES

2.1.1 ZnO + Bi₂O₃ varistor system

Reagent grade zinc oxide and bismuth oxide in the ratio 99.5 and 0.5 (mole %) were mixed by wet ball-milling for 20 hours using deionized water. The mixture was dried and 1.5 g. portions were pressed in a die of 1.53 cm. in diameter at a pressure of 5000 lbs./in². Batches of three pellets were sintered and maintained at different temperatures

Th. 6030

from 600 to 1400°C for one hour and then furnace cooled to room temperature.

2.1.2 ZnO+Sb₂O₃ varistor system

The ZnO-Sb₂O₃ varistor samples were prepared in the same way as above by using 1.0 mole % of Sb₂O₃ additive and sintered at different temperatures from 500° to 1200°C.

2.1.3 ZnO + Bi₂O₃ + CoO varistor system

These varistor samples were also prepared in the same way as above by using 2 mole % (Bi₂O₃ + CoO) additives and pellets sintered at different temperatures from 600° to 1400°C.

2.1.4 ZnO varistor systems containing five additives

These multicomponent varistor samples were prepared in a similar way as described previously by using 3 mole % of five oxides (Bi₂O₃ + Sb₂O₃ + CoO + MnO + Cr₂O₃) additives and also sintered at different temperatures from 600° to 1400°C.

Out of the three pellets from each batch, one pellet was used for the I-V characteristic measurements, the second pellet was used for the X-ray diffraction characterization and the third pellet was used for ESCA, SEM and EPMA analysis.

2.2 MEASUREMENT OF THE CURRENT-VOLTAGE CHARACTERISTICS

For the I-V characteristics measurements, silver was deposited by vacuum evaporation on to the two faces of the sintered pellets. The pellets were held under pressure between the two copper plates in the sample holder fabricated in our Laboratory as shown in fig. 2.1. The current-voltage relationship was measured on the sintered pellets using a Keithly Electrometer (Model 610C) and a stabilized d.c. voltage source. The voltmeter incorporated in a stabilized d.c. voltage source was used for the measurement of the applied voltage and an electrometer was used for the measurement of the current flowing through the varistor sample. The I-V characteristics were measured in the current range upto 100 mA so that the result was not affected by the Joule heating.

The voltage-current characteristics are expressed by the following empirical equation similar to that for the silicon carbide varistors [1] :

$$I = \left(\frac{V}{C} \right)^\alpha \quad \dots (2.1)$$

The voltage non-linearity exponent ' α ' is calculated by the following equation:

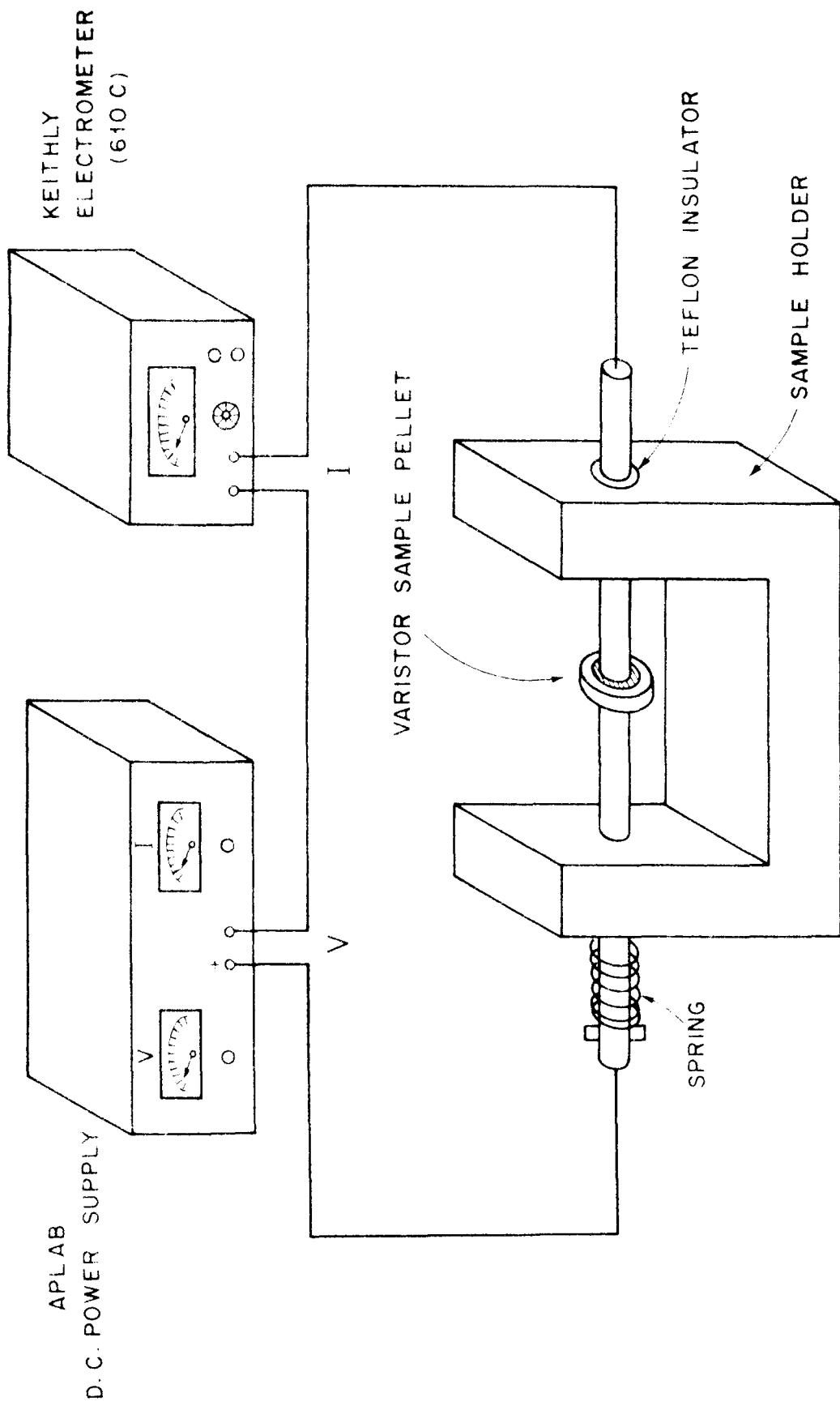


FIG. 2.1 : EXPERIMENTAL SET-UP FOR I-V CHARACTERISTIC MEASUREMENT.

$$\alpha = \frac{dI/I}{dV/V} = \frac{d(\log I)}{d(\log V)} \approx \frac{\log_{10} I_2 - \log_{10} I_1}{\log_{10} V_2 - \log_{10} V_1} \dots\dots (2.2)$$

where V_1 and V_2 are the voltages at currents of I_1 and I_2 respectively.

The current-voltage characteristics of the pellets sintered at different temperatures were measured at room temperature and are plotted on a log-log scale and the non-linear exponent ' α ' values are calculated. The I-V plots and the computed α -values for all the pellets are given and explained in the next chapter.

2.3 ELECTRON SPECTROMETER

All samples of metal oxide varistors prepared in the present work are characterized on a commercial electron spectrometer marketed by M/s Vacuum Generators Scientific Ltd., U.K., ESCA-3, MK-II model and the same is described in detail here.

An electron spectrometer may conveniently be considered to consist of three main parts: (i) the excitation source (X-rays, ultraviolet photons, electrons or ions) to irradiate the sample, (ii) the energy analyser to disperse the ejected electrons according to their energy and (iii) the detector

for a quantitative estimation of the electron intensity and to provide a suitable output signal proportional to intensity as a function of electron binding energy.

Fig. 2.2 shows a block diagram of an electron spectrometer divided into its essential components.

ESCA-3, MK-II is a high resolution electron spectrometer shown in fig. 2.3 and it has been designed so that a variety of radiation sources can be accommodated simultaneously. The electron spectrometer at our National Chemical Laboratory, Pune, has been fitted with the following radiation sources:

1. A twin anode (aluminium and magnesium) X-ray source for X-ray photoelectron spectroscopy (XPS)
2. An ultraviolet helium lamp for ultraviolet photoelectron spectroscopy (UPS)
3. A small spot electron gun for electron initiated Auger electron spectroscopy (AES). (The same electron gun is used for scanning Auger microprobe facility (SAM)).
4. An argon ion gun to etch out the specimen for the depth profiling (DP).
5. Low ion density argon ion gun for secondary ion mass spectrometry (SIMS).

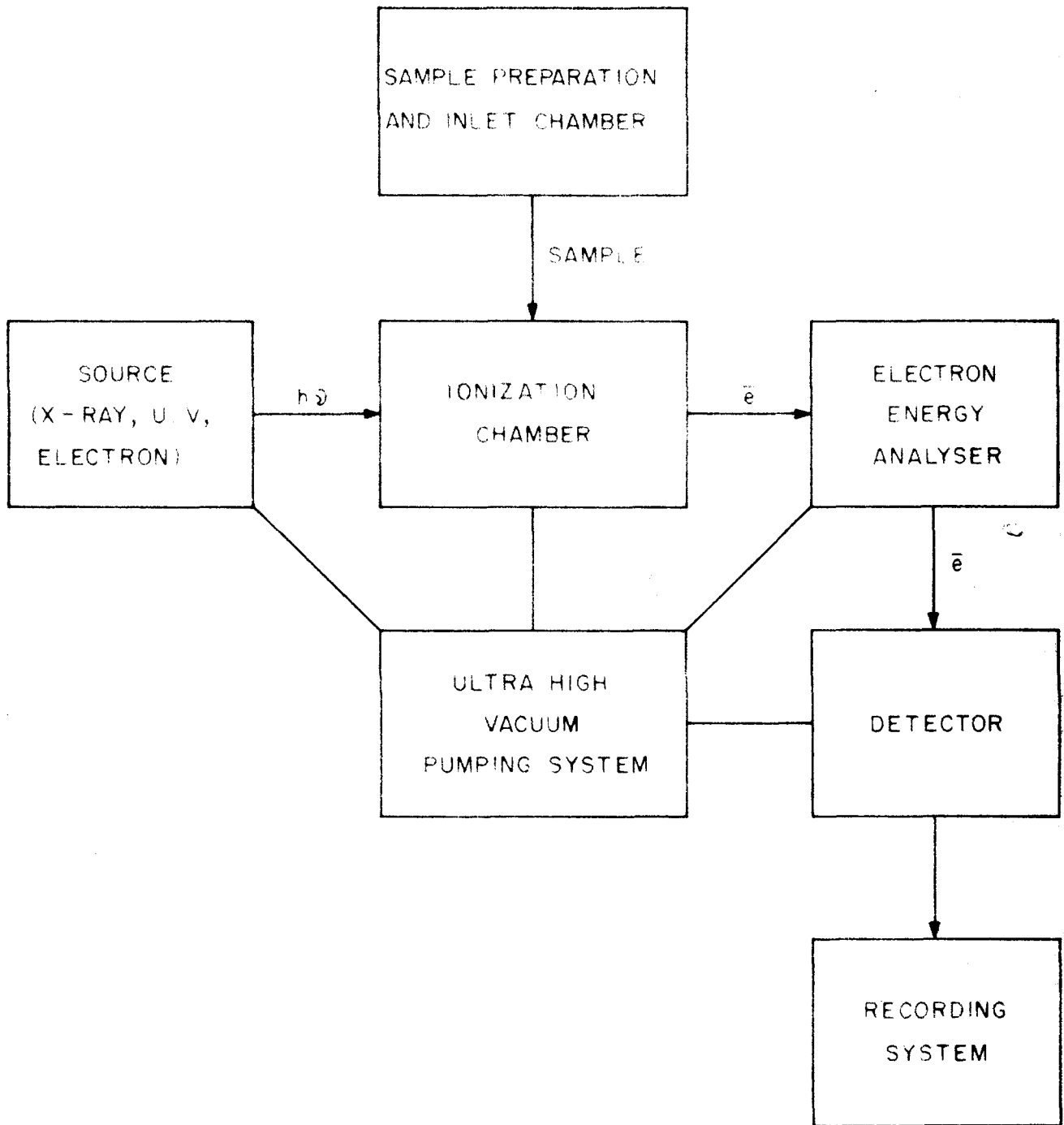
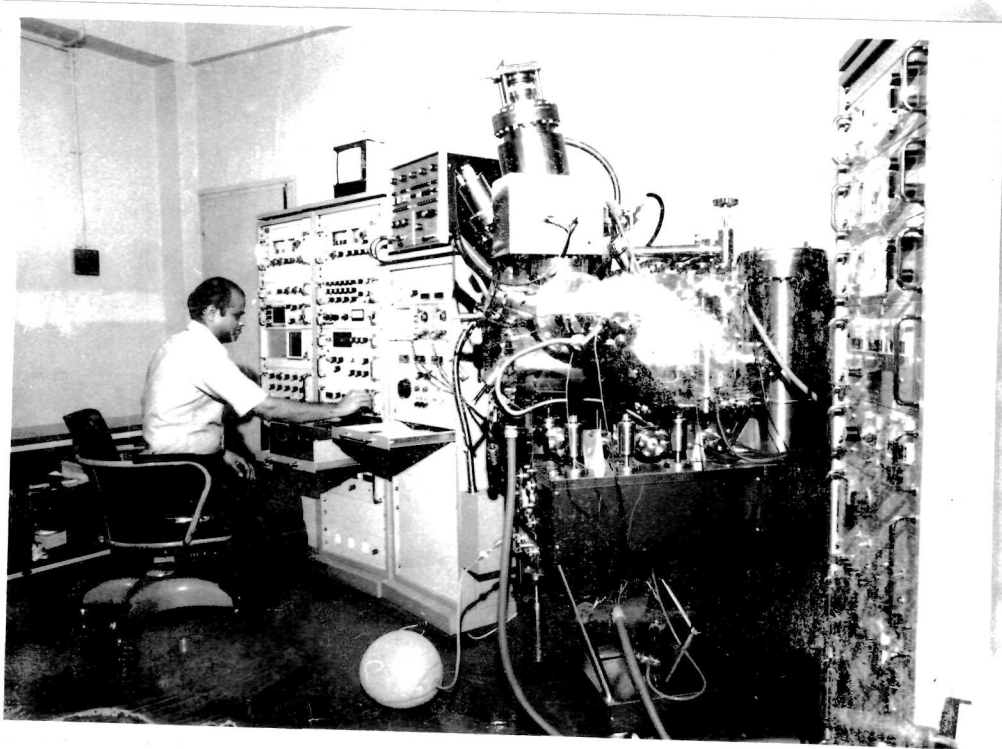


FIG.2.2 : BLOCK DIAGRAM OF AN ELECTRON SPECTROMETER .



**Fig. 2.3 : Electron spectrometer
VG ESCA - 3, MARK-II.**

2.3.1 X-ray source

The simplest type of X-ray source used in XPS is the one which utilizes characteristic emission lines from a target (anode) bombarded by high energy electrons. The energies of these characteristic lines are dependent only on the energy levels within the atoms in the target since they result from electron transitions within these atoms.

In addition to these characteristic lines, a continuous spectrum is also produced and this is dependent upon the primary electron energy. This continuous spectrum is normally known by the German word Bremsstrahlung and its maximum intensity occurs approximately at two thirds of the primary electron energy. The energy spectrum of X-rays emitted from a standard X-ray source used for XPS therefore consists of a broad continuous distribution with characteristic lines superimposed upon it. A narrow monochromatic X-ray source is desirable because the width of the incident X-ray line contributes to the width of the resultant photoelectron peak, which in turn affects the resolution of the electron spectrometer, that is, the ability of the system to distinguish between closely spaced peaks. Hence, when considering the choice of a suitable X-ray source, line width is a major consideration. The other consideration is the energy since this determines the depth into the atomic core from which electrons can be released.

In our electron spectrometer, characteristic radiation emitted from aluminium and magnesium anodes are used. The K_{α} doublet of aluminium has an energy of 1486.6 eV with a composite line width of approximately 0.9 eV FWHM (full width at half maximum height) and K_{α} doublet of magnesium has an energy of 1253.6 eV with a composite line width of approximately 0.8 eV FWHM. The K_{α} lines of the heavier elements are more energetic sources of excitation, but they have broader line widths, for example, the copper K_{α} with energy 8048 eV has a line width of about 2.6 eV FWHM, and the molybdenum K_{α} with energy 17441 eV has a width of about 6 eV FWHM. Moreover, at higher energies, the $\alpha_{1,2}$ doublets in the X-ray spectrum separate, and this gives rise to confusing artifacts in the photoelectron spectrum. Thus, the radiation from the heavier elements is normally undesirable. Feldeg et al. [148] have discussed various X-ray sources of characteristic energies as a function of their line widths and intensities.

The twin anode X-ray source assembly has magnesium on one side and aluminium on the other. The filament is heated by means of a current which produces a high density electron cloud around the filament due to the thermionic emission. Electrons are accelerated towards the anode by the potential upto 15 KV applied between the anode and the filament. An electrostatic shield is interposed to eliminate a line-of-sight

from the filament to the target and thus minimize deposition of filament material onto a target. Water is circulated to cool the anode to dissipate that portion of the energy which appears as heat. The generated X-rays pass through a window and impinge on the sample surface. This window prevents the entry of scattered electrons from the X-ray source into the sample chamber. A thin aluminium window is used to purify the X-ray spectrum by absorbing Bremsstrahlung radiation above approximately 1600 eV.

Even then the characteristic X-ray lines are accompanied by X-ray satellites and Bremsstrahlung. X-ray satellites give satellite peaks and the presence of Bremsstrahlung increases the background level of XPS spectrum. In order to remove the unwanted X-radiation, a crystal monochromator [102] is used, which improves resolution upto 0.2 eV.

Twin anode is useful to differentiate between XPS peaks and Auger peaks. Kinetic energy peaks in XPS will shift by 233 eV and Auger peaks will not move.

For the XPS study, the varistor samples are irradiated by AlK_{α} with 15 KV, 20 mA anode voltage and emission current respectively and MgK_{α} with anode voltage 12 KV and emission current 20 mA and electrons from different orbits are ejected. These ejected electrons are analysed energy-wise by a spherical sector analyser.

2.3.2 Electron energy analyser

The function of the energy analyser is to disperse the ejected photoelectrons from a sample as a function of their energy.

For the electron spectrometer, it is desirable that both the spectral resolution as well as the sensitivity of photoelectron detection be as high as possible. Unfortunately however, both cannot be simultaneously increased, and compromises need to be made. The energy resolution is limited by the width of the photoelectron lines and is determined by several factors, the inherent width of the ionizing radiation, the intrinsic width of the level which is responsible for photoelectron emission, and the finite resolving power of the electron energy analyser used.

The resolution of an electron energy analyser is usually measured as the full width at half maximum height of the electron line divided by the electron energy.

$$\text{Resolution} = \frac{\Delta E (\text{FWHM})}{E_0} \quad \dots \quad (2.3)$$

where $\Delta E (\text{FWHM})$ = full width at half maximum of photoelectron line

and E_0 = electron kinetic energy in eV.

The inverse of the resolution is the resolving power.

A resolution requirement for XPS is around 0.2 eV at 1000 eV electron energy i.e. resolving power $1000/0.2$ equal to 5000. This resolution is sufficient for normal electron spectroscopic applications. For high sensitivity applications it is necessary to be able to degrade the resolution in order to achieve the necessary sensitivity increase. A reasonable upper limit is about 2.5 eV at 1000 eV or a resolving power of 400 [149].

There are two basic types of analyzers using the principle of (1) retarding potential and (2) dispersion respectively. Dispersion instruments are generally used for high resolution work and the same is used in ESCA-3, Mark-II Electron Spectrometer. The types of energy analyser that are being used in different electron spectrometers are described elsewhere [150-155].

An electron energy analyser may be of any type but it must be placed in a suitable vacuum environment, with pressure less than/about 10^{-3} torr to minimize the electron scattering through collision with the residual gas molecules. Similarly, since electrons are influenced by stray magnetic fields (including the earth's magnetism), it is necessary to cancel these fields within the enclosed volume of the analyser. The cancellation of external magnetic field is done by using Helmholtz coils and Mu-metal shielding.

2.3.3 Spherical sector analyser

The spherical sector analyser used for electron energy analysis in ESCA-3, MK-II electron spectrometer is shown in fig. 2.4. It consists of two hemispheres (actually 150°), inner and outer, of 100 mm mean radius of curvature, mounted so as to provide a constant separation between them. A positive voltage is applied to the inner hemisphere and negative voltage to the outer one.

Electrons emitted by the sample enter the analyser through the entrance slit and come under the influence of the electrostatic field (V) applied between the hemispheres, so that they now follow a curved path of constant radius.

High energy electrons moving at a relatively high speed are not deflected very much by the electrostatic field between the hemispheres, so they strike the outer hemisphere. Conversely low energy electrons moving at a relatively low speed are easily deflected and they strike the inner hemisphere. High energy electrons can then be detected by retarding them before they reach the analyzer until their energy is equal to the pass energy of the analyzer. Low energy electrons are detected in a similar way by accelerating them. A positive voltage is applied to the sample plate to retard the electrons and a negative voltage to accelerate

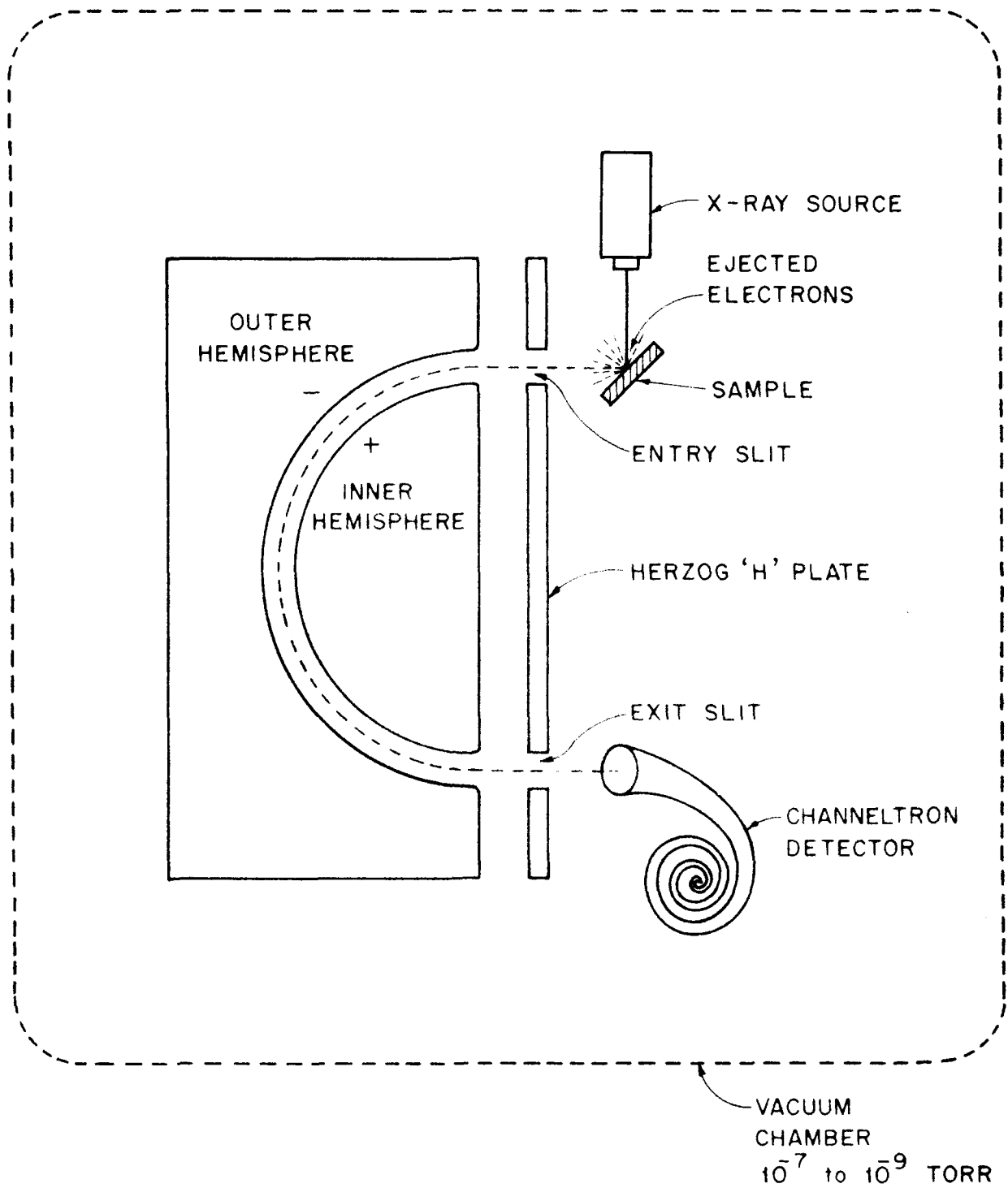


FIG. 2.4 : HEMISPHERICAL ANALYSER.

them. The plate in front of analyzer hemispheres which contains the entry and exit slits is called the "Herzog" or "H" plate to which the retarding potential is applied.

The inner surfaces of hemispheres are specially treated to minimize the emission of secondary electrons. The slit at the entrance to the analyzer improves the resolution by ensuring that electrons enter the analyzer close to the neutral axis between the hemispheres. The resolution is further improved by the exit slit which allows only those electrons which are close to the neutral axis to reach the detector. ESCA-3, Mark-II electron spectrometer is provided with externally adjustable 4, 2, 1 and 0.5 mm entrance and exit slits.

The analyser thus, works as a narrow pass filter, letting through only electrons with an energy " HV ", where V is the potential difference between the inner and outer hemispheres and H is a constant determined by the physical dimensions of the analyzer which is equal to 2.64 for our instrument.

The electrons from the sample are retarded to a pass energy " nV " by the scanned retarding potential " R " applied between the specimen and the electrical centre point of the hemispheres.

If E_{KE} = Kinetic energy of ejected electron
(conventionally referred to the
Fermi level)

$$\text{then, } E_{KE} = R + hV + w \quad \dots\dots (2.4)$$

where 'w' is a constant arising from the work function of the spectrometer material and is equal to 4.2 for our instrument.

Binding energies are obtained by subtracting the kinetic energy from the photon quantum energy ($h\nu$).

The spectrometer control unit incorporates a switch for setting the pass energies of the analyser at 2, 5, 10, 20, 50, 100 or 200 eV by varying the value of 'V' (voltage applied between two hemispheres) correspondingly to about 0.7, 1.9, 3.8, 7.6, 19, 38, 76 volts. It can provide energy scans of 1, 3, 10, 30, 100, 300 and 1000 volts in 30, 100, 300, 1000 and 3000 seconds.

The ability to select the energy with which electrons are transmitted around the analyser and the ability to change entry and exit slit widths, provides a great flexibility in choosing the optimum sensitivity or resolution to suit a particular application.

2.3.4 Detector

The electron current emerging from the exit slit of the analyser is very small, of the order of 10^{-16} to 10^{-13}

amperes. To detect this very weak current, a channel electron multiplier is used.

A channel electron multiplier is a small curved glass tube as shown in fig. (2.4). The inside wall of this glass tube is coated with a high resistivity material. If a potential is applied between the ends of the tube, the resistive surface becomes a continuous dynode, electrically analogous to the separate dynodes of a conventional photomultiplier together with the resistive chain used to establish the separate dynode potentials.

An electron entering the low potential end of the channel electron multiplier generates secondary electrons on collision with the wall of the tube. These secondary electrons are accelerated along the tube until they strike the wall again, where they generate further secondary electrons. This process produces a large number of electrons at the positive end of the tube. A channel electron multiplier tube thus responds to an input of one electron by producing an output pulse of charge containing upto 10^8 electrons and its duration (full width at half maximum) is about 10 nanoseconds.

The output electron beam charges a capacitor in the anode circuit of the multiplier which produces a voltage pulse.

These pulses are fed to an amplifier and a discriminator. These pulses are then converted into NIM standard pulse of 5 volt amplitude and 500 nanosecond durations and fed to the ratemeter which reads out the counts (pulses per second).

The X-axis of the X-Y recorder is connected via dividing resistors to scan the amplitude supply. The Y-axis is fed from the recorder output of the rate meter. A spectrum of total number of ejected electrons versus kinetic energy is thus plotted on the X-Y recorder.

Binding energies are obtained by subtracting the kinetic energies from the energy of the X-ray source ($h\nu$).

2.3.5 Vacuum system

The heart of the electron spectrometer is its ultra high vacuum (UHV) console. Ultra high vacuum (better than 10^{-8} torr) is required for two reasons: (i) the ejected electron should pass from the sample through the analyser without making any collisions with residual gas molecules and (ii) the partial pressure of reactive residual gases must be reduced to such a level that they will not unduly contaminate the sample surface and interfere with the study of that surface.

ESCA-3, Mark-II vacuum console is designed to accept a variety of radiation sources simultaneously thereby allowing sequential analyses by a range of complementary surface techniques. The UHV system is divided in two parts, one is the sample preparation chamber and the other is the sample analyser chamber.

The analyser chamber is fabricated from mu-metal with fourteen copper gasket-sealed-flanged ports fitted with the electron analyser assembly, the twin anode X-ray source, the UV source, the electron source, the ion source, the channeltron electron multiplier detector, the secondary electron detector, the glass view port, the sample manipulator and the X-ray monochromator source.

The 150 mm diameter x 340 mm long stainless steel specimen preparation chamber has 16 flanged ports sealed with copper gaskets and fitted with gate valve, sample transfer mechanism, argon ion cleaning gun, gas admission system, SIMS quadrupole detector, ion source, charge neutralising gun, view port and evaporation source.

Both the chambers are independently pumped by oil diffusion pumps fitted with water cooled chevron baffle and liquid nitrogen cold traps and backed rotory pumps. In addition titanium sublimation pumps (TSP) are fitted to both the chambers to reduce the pressure down to 5×10^{-11} torr.

The preparation chamber is isolated from the analyser (or spectrometer) chamber at all times except when the specimen is being moved between them. The spectrometer and its channeltron multiplier is therefore protected against contamination from specimen preparation procedures. The sample preparation chamber also acts as a vacuum lock facility permitting relatively quick specimen change overs.

The vacuum monitoring and protection system incorporate Pirani and ion gauges. The roughing line pressures are measured by Pirani gauges which incorporate facilities for protecting the diffusion pumps against failures in the rough vacuum system. Ultra high vacuum pressures are measured by ion gauges fitted separately to both chambers.

2.3.6 Sample handling

The electron spectrometer can handle samples which may be either solid with a regularly defined surface or a powder, and may be a conductor, semiconductor or non-conductor. Powders may be pelletized, compressed into suitable holder or dusted onto a carrier such as double-sided adhesive tape.

The mounted sample holder is attached to the sample probe which is moved in the preparation chamber and to the analyser chamber by means of a transfer mechanism consisting of edge welded stainless steel bellows giving a movement of approximately 13 inches. A heating and cooling facility enables the temperature of the sample to be varied between 600°C to the liquid nitrogen temperature. The sample probe is mounted on a precision rotary motion drive with 360° movement to allow the specimen to be accurately positioned for the appropriate analysis.

2.3.7 ESCA analysis of varistor samples

X-ray photo-electron spectra of zinc oxide varistor samples were recorded on this instrument.

Before analysing the varistor samples, the spectrometer was calibrated with the help of standard metallic samples. The spectroscopically pure foils of gold, silver, copper and platinum (obtained from M/s Johnson and Matthey Chemical Company, U.K.) were mounted on the standard sample holder assembled on to the sample transfer mechanism and finally located in the sample preparation chamber. The sample preparation chamber was then evacuated upto 10^{-2} torr by rotary pump and then upto 10^{-7} torr by the oil diffusion pump. The whole vacuum system was then baked at

150°C for 12 hours so that any contamination on the internal surface was removed and the system was cleaned. After removing the bakeout shrouds, the system was cooled to room temperature. The ion gauge heads, X-ray anode and filament were outgassed for 30 minutes.

The liquid nitrogen traps of both the oil diffusion pumps were filled by sufficient liquid nitrogen. The titanium sublimation pump was fired for 1.5 minutes and vacuum better than 10^{-10} torr was achieved.

The samples were cleaned by argon ion etching followed by heating at 200°C in the sample preparation chamber to remove all the surface contaminations. After opening the sample preparation and analyser chamber isolation gate valve, samples were transferred to the analyser chamber. One of the four samples was positioned exactly under the X-ray source and in front of the entry slit of the analyser with the help of the X,Y,Z sample manipulator.

The ratemeter, channeltron multiplier power supply, X-ray source power supply, X-Y recorder, digital voltmeter and spectrometer control units were switched on for half an hour to stabilize before the spectra were taken.

The spectrometer control unit comprising programmed power supply, the ramp generator, hemisphere voltage, HV + W circuit and pedestal supply were calibrated by

adjusting the calibrating potentiometers. The XPS spectra were then recorded. The other three samples were also analysed in the same way. The binding energies are given in table (2.1). The best available standard binding energy values [156] are also given in the same table for comparison.

The binding energy values are in good agreement within experimental errors.

After switching off the X-ray source, the analyser and the detector power supply, the samples were brought back to the preparation chamber and the isolation gate valve was closed. Then dry nitrogen was let in the sample preparation chamber upto atmospheric pressure. The sample probe was then removed from the sample transfer mechanism by unbolting the flange.

The sintered ZnO varistor samples were mounted (three at a time) on the sample holder and were examined in the same way as discussed above.

Table 2.1 : Binding energies suitable for use as standards for calibration of X-ray photoelectron spectrometer

Metal	Level	BE (eV) [Ref. 156]	BE (eV) [Our experi- mental values]
Silver	3d _{5/2}	368.2 ± 0.2	368.3
Gold	4f _{7/2}	83.8 ± 0.2	83.96
Platinum	4f _{7/2}	71.0 ± 0.2	71.0
Copper	2p _{3/2}	932.8 ± 0.2	932.4

For comparative study the spectrometer parameters were kept constant while analysing all varistor samples. All the spectra were taken at 50 eV pass energy of the analyser, with 4 mm entry and exit slit, at 10^4 counts per second and 0.1 second time constant. Each spectrum was recorded for 300 seconds with 1000 and 100 volts scan. The total effective voltage to the channeltron multiplier was kept at 3.5 KV to avoid its damage.

As ZnO varistor samples are highly resistive the carbon 1s (285.0 eV) peak was used as an internal standard for correcting of any charging effects in the sample.

The surface of the pellet as got after sintering was first examined by XPS. The pellet was then brought out of the spectrometer and fractured in air to expose the inside material which was also examined by XPS in a similar way. Lastly, the pellet was finely powdered by grinding in a mortar, and pressed in the form of a thin layer in the gold mesh of the sample holder and examined by XPs.

The recorded XPS spectra and their analysis are given in the next chapter.

2.4 SCANNING ELECTRON MICROSCOPY (SEM)

Scanning electron microscopy has become a valuable tool in a broad variety of scientific and technical

investigations. The main reason for this is that this instrument enables the user to visualize directly the surfaces of rough specimens over a wide range of magnifications with a good depth of field. It is quite different from both the conventional light microscope and transmission electron microscope. The light microscope has a very limited depth of field at high magnifications which makes it difficult to study rough surfaces. The conventional transmission electron microscope (TEM) has a great depth of field and resolution associated with its electron optics, but cannot work directly with solid surfaces and its scope in these applications has been limited by the problems of making replicas of surfaces and interpreting the resulting images. Although the resolution achieved in scanning electron microscopy (SEM) is generally lower than that in the transmission electron microscopy, the great depth of focus and the relative ease of sample preparation make the former an ideal instrument for the examination of the surface features, morphology and microstructure of various materials. During the last forty years, various people [157-175] took tremendous effort in development of today's advanced high resolution scanning electron microscopes. Today a majority of SEM facilities are equipped with X-ray analytical capabilities. Thus, topographic, crystallographic and compositional information can often be obtained rapidly and efficiently.

2.4.1 Basic function of SEM

The basic function of the scanning electron microscope (SEM) is to produce on a cathode ray tube (or T.V. tube) an image of three dimensional appearance, derived from the action of an electron beam. When a finely focussed electron beam impinges on the specimen surface, different types of signals are produced as shown in fig. 2.5 like secondary electrons, backscattered electrons, Auger electrons, characteristic X-ray photons, transmitted and inelastically scattered electrons, elastically scattered electrons, absorbed electrons, cathodo luminescence etc. These signals are used to measure various characteristics of the sample like surface topography, elemental composition, crystallography, magnetic and electrical properties etc. The secondary electron signal is strongly dependent on the topography of the specimen, therefore it is used for the image formation in the SEM.

In the scanning electron microscope a very small diameter electron beam scans across the part of the specimen to be imaged like a television type raster pattern.

The way in which electrons are scattered by variations in the specimen surface are detected and this backscattered information is used to vary the brightness of a T.V. type display tube which is being scanned in synchronism with the electron beam.

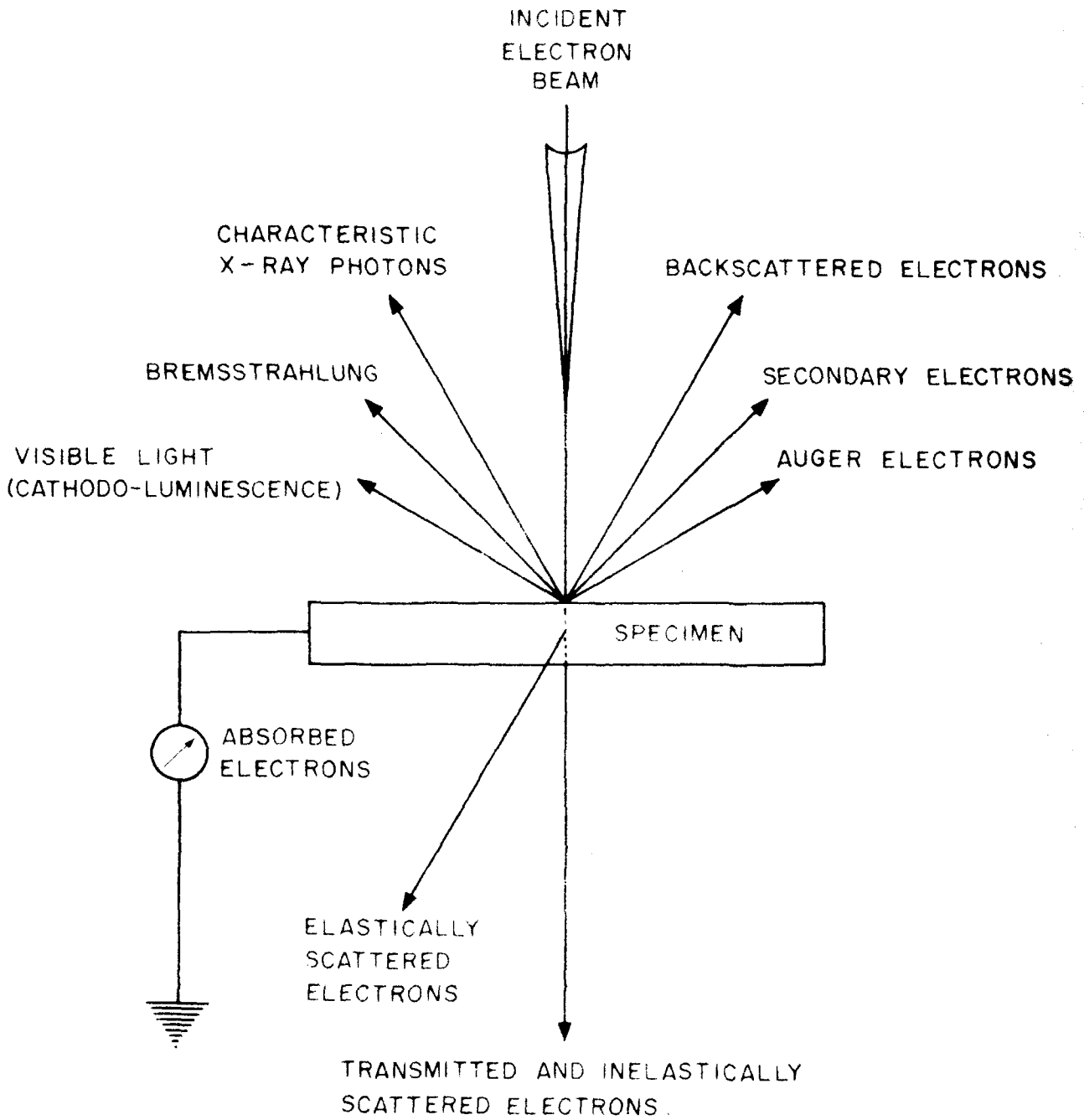


FIG. 2-5 : VARIOUS SIGNALS GENERATED IN THE SCANNING ELECTRON MICROSCOPE .

2.4.2 Cambridge stereoscan 150-SEM

Cambridge stereoscan-150 scanning electron microscope (SEM) is a three lens system with specimen detail resolution achievable to better than 70 \AA under satisfactory conditions. The depth of focus is at least 300 times greater than that of a light microscope. It has a magnification range between X20 and X100,000 which represents a scanned area on the specimen from 6 mm x 5 mm to $1.2 \mu\text{m} \times 1 \mu\text{m}$ at 10 mm working distance. Additional variable magnification of upto X3 can be obtained using a zoom facility. The true magnification at all working distances is indicated by a μ -mark on the display.

The block diagram of the scanning electron microscope is shown in fig. 2.6, which is conveniently divided into four sub-systems.

- (1) Electron optics - Responsible for generating and manipulating the primary electron beam.
- (2) Scanning system - Responsible for producing the electrical signals which make up the raster scan, including scan coils, magnification control and display scanning.
- (3) Video system - Responsible for collecting information about interactions of electron beam and specimen, processing this information, and presenting it to the display in a suitable form.

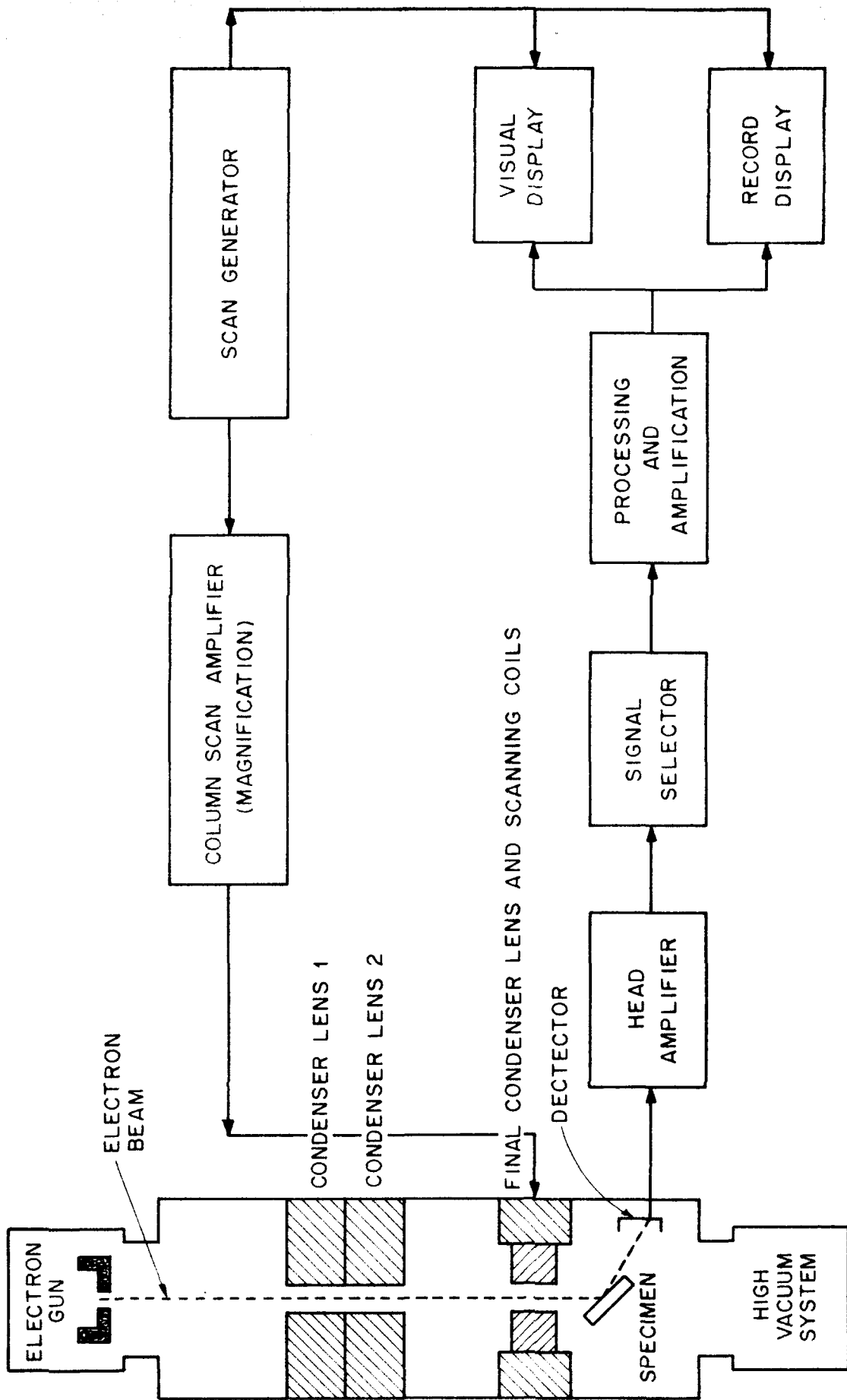


FIG. 2.6 : BLOCK DIAGRAM OF SCANNING ELECTRON MICROSCOPE (SEM).

- (4) Vacuum system - Responsible for maintaining a sufficiently good vacuum in the electron optics, to ensure efficient generation and propagation of the electron beam.

The signals from the photomultiplier pass through a head amplifier and then to the display C.R.T. (cathode ray tube), where the amplified signals modulate the brightness of the C.R.T. The tube is scanned in synchronism with the scanning of the specimen by the electron probe. The resultant image has a marked three dimensional appearance because the contrast is produced by the variation in the number of electrons emitted or reflected from the different parts of the specimen, which is a function of the inclination of the surface to the incident electron beam.

A 35 mm camera is mounted on the recording C.R.T., which can provide high quality photograph of the image presented on the normal visual display.

2.4.3 SEM analysis of varistor samples

To understand the varistor mechanism and its micro-structure, grain growth, grain boundary segregation, migration etc., ZnO varistor samples prepared for this work, were studied by the scanning electron microscope; Cambridge Stereoscan-150 model, manufactured by M/s Cambridge

Scientific Instruments Ltd., U.K. as shown in fig. 2.7.

The ZnO varistor sintered pellets are fractured and the inside portion is exposed, and mounted on the standard specimen mounting stub. The samples are coated by a good conducting thin layer (upto 200-300 Å thickness) of silver by vacuum deposition technique to prevent charging of the specimen. The specimen stub containing 7-9 small pieces of the sample sintered at various temperatures are mounted on a specimen stage. The sample chamber and column are then evacuated by the oil diffusion pump backed by the rotary pump upto 10^{-5} torr.

For comparative study, the electron beam parameters were kept constant while analysing all the varistor samples. The photographs of the samples with 20 KV EHT, 2.7 amp. filament current, 390 µA beam current at various magnifications from X2K to X10K were recorded by a 35 mm camera attached on the recording C.R.T. The photographs taken for the ZnO varistor are given and discussed in the next chapter.

2.5 ELECTRON PROBE MICROANALYSIS (EPMA) USING ENERGY DISPERSIVE X-RAY SPECTROMETER

Electron probe microanalysis is a powerful analytical technique capable of performing elemental analysis of microvolumes, typically on the order of a few cubic microns in

bulk samples and considerably less in thin sections. The sample is analysed non-destructively and quantitative analysis can be obtained with a good accuracy. Another important feature of the EPMA is the capability for obtaining X-ray signal scanning pictures, which gives the elemental distribution in the area of interest. The various people [176-185] took lots of effort to develop techniques of electron probe microanalysis (EPMA) using a solid state detector capable of performing simultaneous analysis of all elements heavier than sodium.

A block diagram of the essential components of the energy dispersive X-ray spectroscope (EDS) is shown in fig. 2.8.

2.5.1 X-ray generation

When an electron beam of sufficient energy strikes the atom, an inner shell electron may be ejected. In order to return the atom to its lowest energy state, an outer shell electron (of greater energy) will fill the vacancy in the lower energy shell. In so doing, an X-ray will be released with an energy equal to the difference between the energy of the electron in its initial and final energy states.

Assume, that an electron of high energy strikes the atom and ejects a K-shell electron. To fill the gap created

by the ejected electron, an L-shell electron may drop to the K-shell, lowering the energy of the atom and emitting K_{α} X-radiation in the process. If an electron from the M-shell fills the K-shell vacancy, K_{β} X-radiation would be emitted. Similarly, if an electron from the next outer shell (N) filled the vacancy, L_{α} radiation would be emitted.

The most probable transition to occur when a K-shell vacancy is created is the L-K transition since these are adjacent energy shells. Therefore K_{α} radiation will always be made intense than the K_{β} radiation. The K_{β} radiation will be of higher energy than K_{α} radiation since the energy difference between the M and K shells (K_{β} radiation) is greater than the energy difference between the L and K shells (K_{α} radiation).

The salient feature of the characteristic X-ray production is that the energy of the characteristics radiation in a given series of lines varies monotonically with atomic number. This is expressed by Moseley's law :

$$\sqrt{E} = C_1 (Z - C_2) \quad \dots\dots (2.3)$$

where E = energy of the emission line for a given X-ray series

Z = atomic number of the emitter

C_1 and C_2 are constants.

From this equation it is clearly shown that if the energy of a given K, L and M line is measured, then the atomic number of the element producing that line can be determined.

2.5.2 Si(Li) detector

The heart of an energy dispersive spectrometer is a Si(Li) diode whose active area is typically 12.5 mm^2 and thickness is 3 mm. If a diode is reversed-biased (by typically 1000 volts) a depletion region is established. All of the normally present electrons and holes in the depletion region are removed by the externally applied electrical field. The absorption of an X-ray quantum release a photoelectron from a Si atom in the detector. This photoelectron then produces a wake of ionization at the rate of one electron-hole pair per 3.8 eV of initial photoelectron energy. This charge is collected by a bias voltage of several hundred volts and converted to a voltage pulse in the field effect transistor (FET) input first stage of the preamplifier.

The FET is located directly behind the silicon lithium drifted Si(Li) detector and provides the first stage of signal amplification. The actual charge induced in the detector is extremely small, therefore, to minimize noise, the FET must be located as close to the detector as possible and must be operated at low temperature. In addition, low temperature is

required at all times to limit lithium diffusion in the silicon crystal as lithium is very mobile at room temperature. To achieve the required low temperature, the detector and FET are connected through an efficient heat conductor actually a copper rod called the "cold finger" to a liquid nitrogen dewar. A very thin 0.3 mm beryllium window is used to enclose the end cap to ensure its vacuum integrity while providing high X-ray transmission.

The X-ray signal from the sample passes through this beryllium window into an evacuated chamber containing a cooled, reverse-biased p-i-n lithium drifted silicon crystal. Absorption of the X-rays in the intrinsic region results in the formation of electron-hole pairs, which are collected by a charge sensitive preamplifier. The signal is further amplified and shaped by a main amplifier and passed to a multichannel analyser (MCA) where the pulses are sorted by voltage which remains proportional to their incident energy. The energy distribution is then displayed on a cathode ray tube or an X-Y recorder or is transmitted to a computer for further processing.

2.5.3 Varistor sample analysis by EPMA

To get the elemental composition and their distribution in the microstructure of the zinc oxide varistor,

samples prepared for these studies were analysed by electron probe micro analysis (EPMA) technique using the Link Systems Model 290-2K X-ray Energy Dispersive Spectrometer attached to a Cambridge Stereoscan-150 Scanning Electron Microscope (SEM) shown in fig. 2.7.

The same samples were used for EPMA analysis, which were prepared for scanning electron microscopic studies.

The Link Systems 290 Energy Dispersive (ED) system consists of lithium drifted silicon Si(Li) detector having resolution of 150 eV FWHM at 5.9 KeV, using MnK_{α} peak 0.3 mm Be window with a take off angle of 75° .

All the data acquisition, display and permanent storage is done via a 16 bit Data General's NOVA-2 computer with 16 K words of memory.

Anologue to digital converter (ADC) keyboard, video display unit, teletype printer are connected to the computer's central processing unit via the input/output bus.

The histogram of the energy versus counts can be displayed on the TV monitor (video display unit) which is interfaced by the digital to video convertor. There is also a provision of alphanumeric character storage and readout logic. This can store 64 x 6 bit characters on the top and

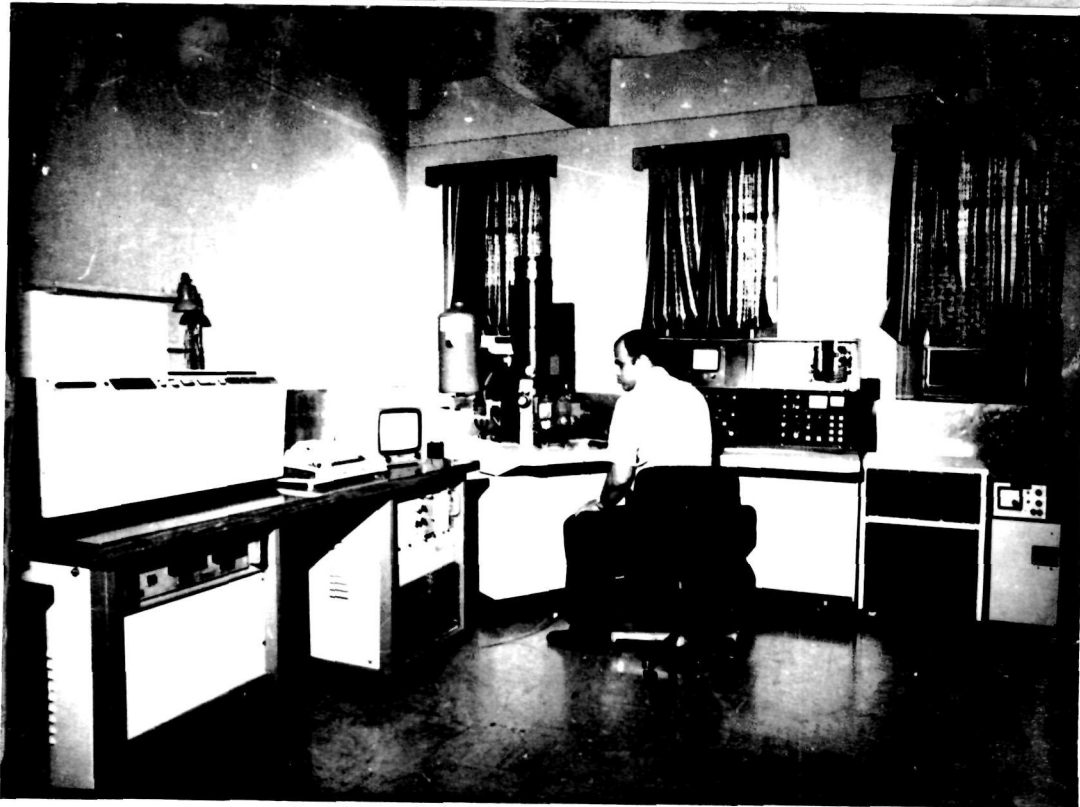


**Fig. 2.7 : Scanning Electron Microscope
Cambridge Stereoscan - 150 and
Energy dispersive X-ray spectrometer
Link systems 290-2K.**

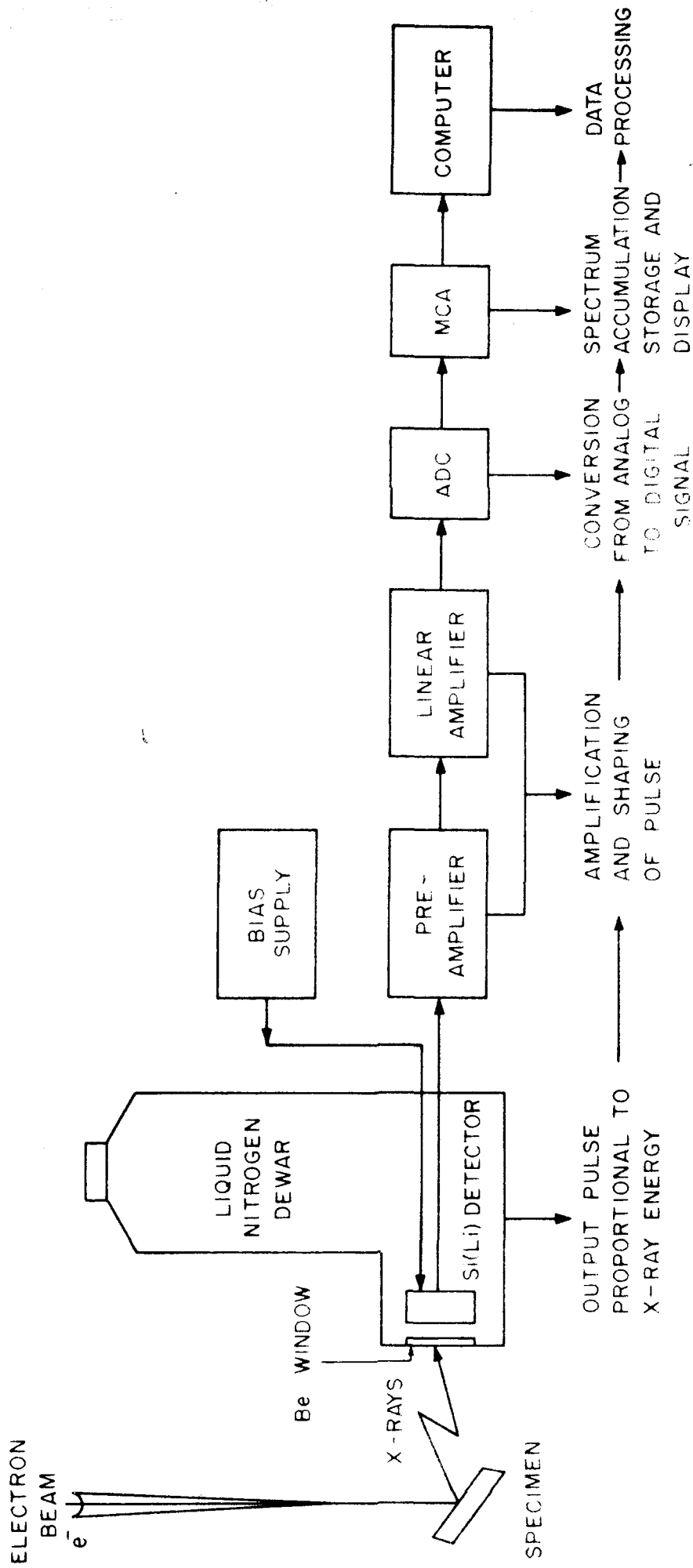


FIG. 2-8 : BLOCK DIAGRAM OF AN ENERGY DISPERSIVE X-RAY ANALYSIS SYSTEM.

bottom of the video display unit. This provides the display of various spectral information like count rate in the spectrum, count rate in the window, integral of a peak, atomic symbol for the K, L, M lines, counts and energy at the cursor position.

The microstructure elemental analysis, X-ray distribution image of various elements and point analysis of varistor samples were carried out in this study and details are given in the next Chapter.

2.6 X-RAY DIFFRACTION (XRD) ANALYSIS OF VARISTOR SAMPLES

The ZnO varistor pellets were directly mounted on the sample holder of a Philips X-ray diffractometer model PW 1730 for the structure identification. The diffracted X-ray intensities were recorded as a function of 2θ by using copper target ($\text{CuK}\alpha$, $\lambda = 1.5404 \text{ \AA}$). The values of the interplaner spacing 'd' were calculated using the Bragg's relation :

$$n\lambda = 2d \sin\theta \quad \dots\dots (2.4)$$

where λ is the wavelength of the X-ray used, d is the distance between the two neighbouring atomic planes and θ is the Bragg's angle.

The XRD results for different varistor samples are tabulated and discussed in the next Chapter.

CHAPTER - III : RESULTS AND DISCUSSION

To understand the cause of the unusual non-linear property of metal oxide varistors, four systems were prepared for this study:

<u>System</u>	<u>Abbreviated as</u>
1. ZnO + Bi ₂ O ₃	ZB
2. ZnO + Sb ₂ O ₃	ZS
3. ZnO + Bi ₂ O ₃ + CoO	ZBC
4. ZnO + Bi ₂ O ₃ + Sb ₂ O ₃ + CoO + MnO + Cr ₂ O ₃	ZBSCMCr

The current-voltage characteristics of these pellets sintered at different temperatures have been measured at room temperature and values for the non-linear exponent (α) are calculated. The varistor samples of these four systems are characterised by the XPS, SEM, EPMA and XRD techniques. All the experimental results and their detailed analysis are presented for each system separately. They are tabulated and discussed in this Chapter.

3.1 ZnO + Bi₂O₃, (ZB) SYSTEM

3.1.1 I-V characteristics

The I-V characteristics of these pellets sintered at different temperatures are measured at room temperature using the experimental set-up described in Chapter-II. The results

are plotted in fig. 3.1. The non-linear behaviour is seen clearly from the I-V plots, which shows a systematic change as a function of the sintering temperature. These I-V curves of the 2B pellets are expressed in a standard form used in the earlier studies on silicon carbide ceramics [1],

$$I = \left(\frac{V}{C} \right)^\alpha \quad \dots (3.1)$$

The non-linear exponent ' α ' in the above equation is calculated using the equation (2.2) as described earlier. The computed ' α ' values for these pellets sintered at different temperatures are given in table 3.1. The ohmic resistance of the pellets sintered at temperatures less than 800°C was too high leading to a high I^2R heating at currents greater than 10^{-6} amp. It is seen that the ' α ' value increases slowly upto 900°C, attains a maximum in the temperature range 1200-1300°C and then slowly falls off. The maximum α -value of 6.5 is obtained with pellets sintered at 1300°C, which decreases to 4.3 for those sintered at 1400°C. These results agree with the reported α values [29,32,186,187].

The non-linear constant 'C' is calculated from the I-V plots for different sintering temperatures and the values are given in table 3.1. It is seen that constant 'C' decreases as sintering temperature increases.

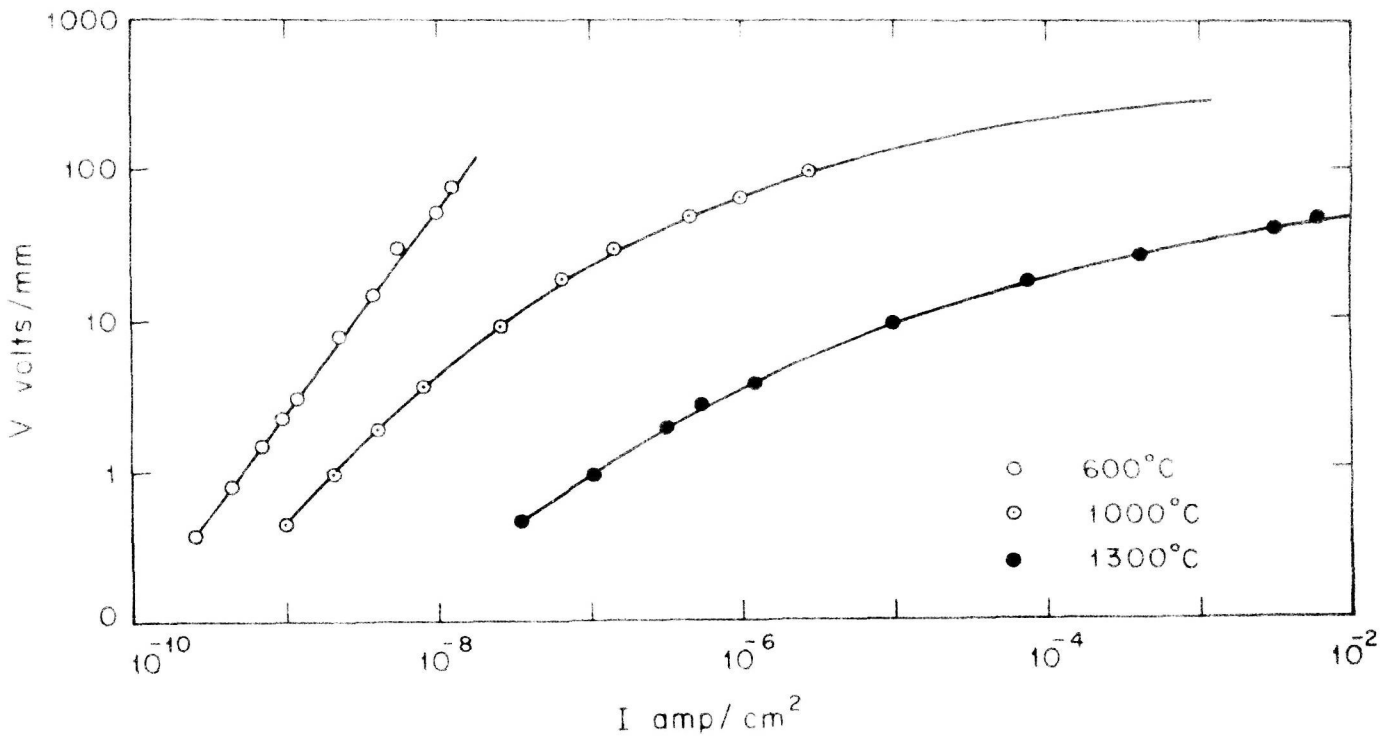
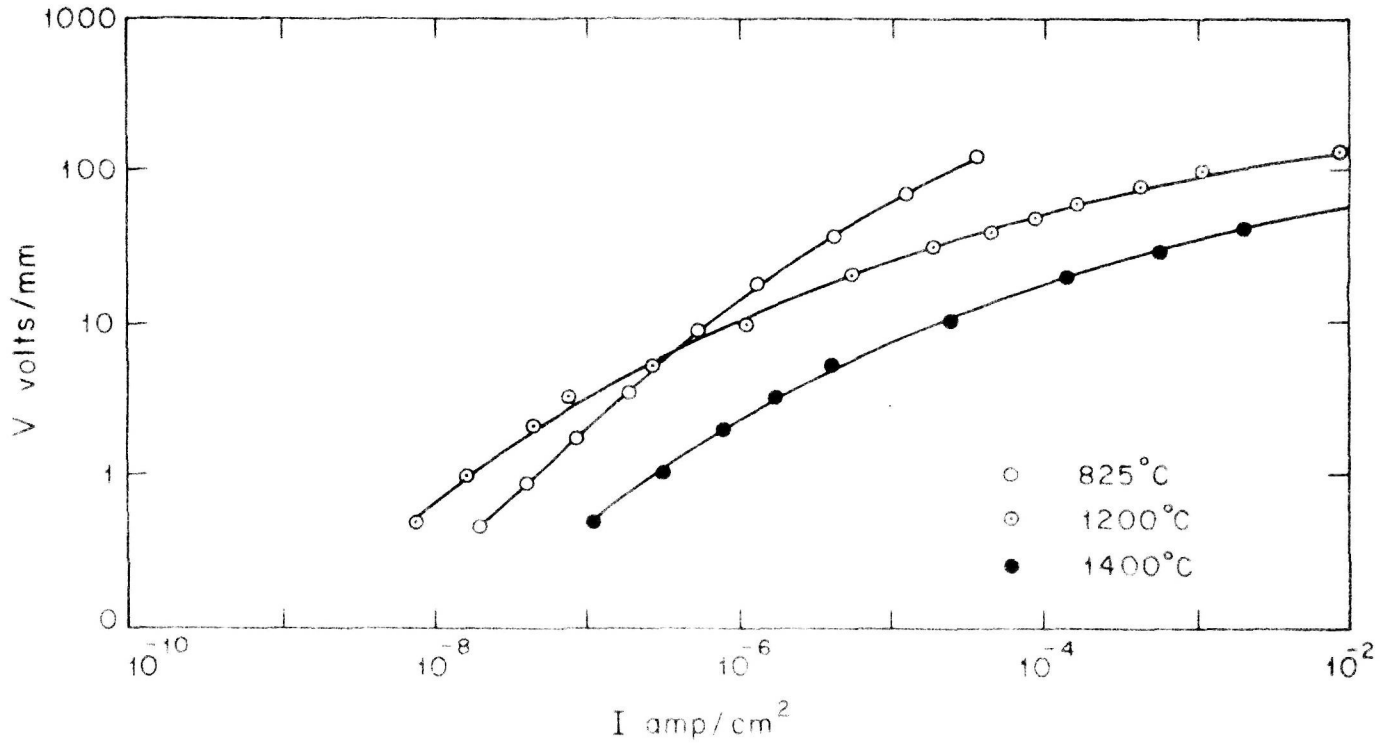


FIG. 3-1 : I-V CHARACTERISTICS OF (ZB) PELLETS SINTERED AT VARIOUS TEMPERATURES.

Table 3.1 : Values of α , C and density for the ZB pellets sintered at various temperatures

Sintering temperature $^{\circ}\text{C}$	Non-linear exponent ' α '	Non-linear constant 'C' (V/mm at 1 mA)	Pellet density (gm/cm ³)
600	1.0	3.2×10^8 *	3.3
825	1.8	632	3.3
1000	3.4	339	3.5
1200	5.7	100	5.3
1300	6.5	34	5.3
1400	4.3	33	5.2

* extrapolated value

The density of pellets sintered at different temperatures is calculated by measuring the dimensions and weight of the pellets and is given in table 3.1. It is observed that the density slowly increases upto 1100°C, attains maximum in the temperature range 1200-1300°C and then falls off slowly, similar to the observed variation of α . This behaviour brings out the importance of sintering and densification of pellet to get the maximum α value.

3.1.2 Electron spectroscopic study

As indicated earlier, X-ray photoelectron spectroscopy is an ideal and proven technique to study the electronic structure, chemical nature, oxidation state, migration, segregation at grain boundary etc. of the mixed oxide system sintered at various temperatures. Fig. 3.2 shows the typical spectra (i.e. intensity versus binding energy) obtained from the surface of a pellet of 99.5 mole % ZnO and 0.5 mole % Bi₂O₃ and from the surface of another pellet (from the same batch) sintered at 1200°C. The peaks have been identified using known systematics of XPS data and assigned to Zn-3d and Bi-4f_{7/2} and Bi-4f_{5/2} states. It can be seen clearly that the intensities of Bi-4f_{7/2} and Bi-4f_{5/2} peaks are considerably enhanced after sintering the pellet at 1200°C. This is possible due to the migration of Bi₂O₃ on ZnO grain surfaces. Therefore, the intensity of Bi peaks increases and

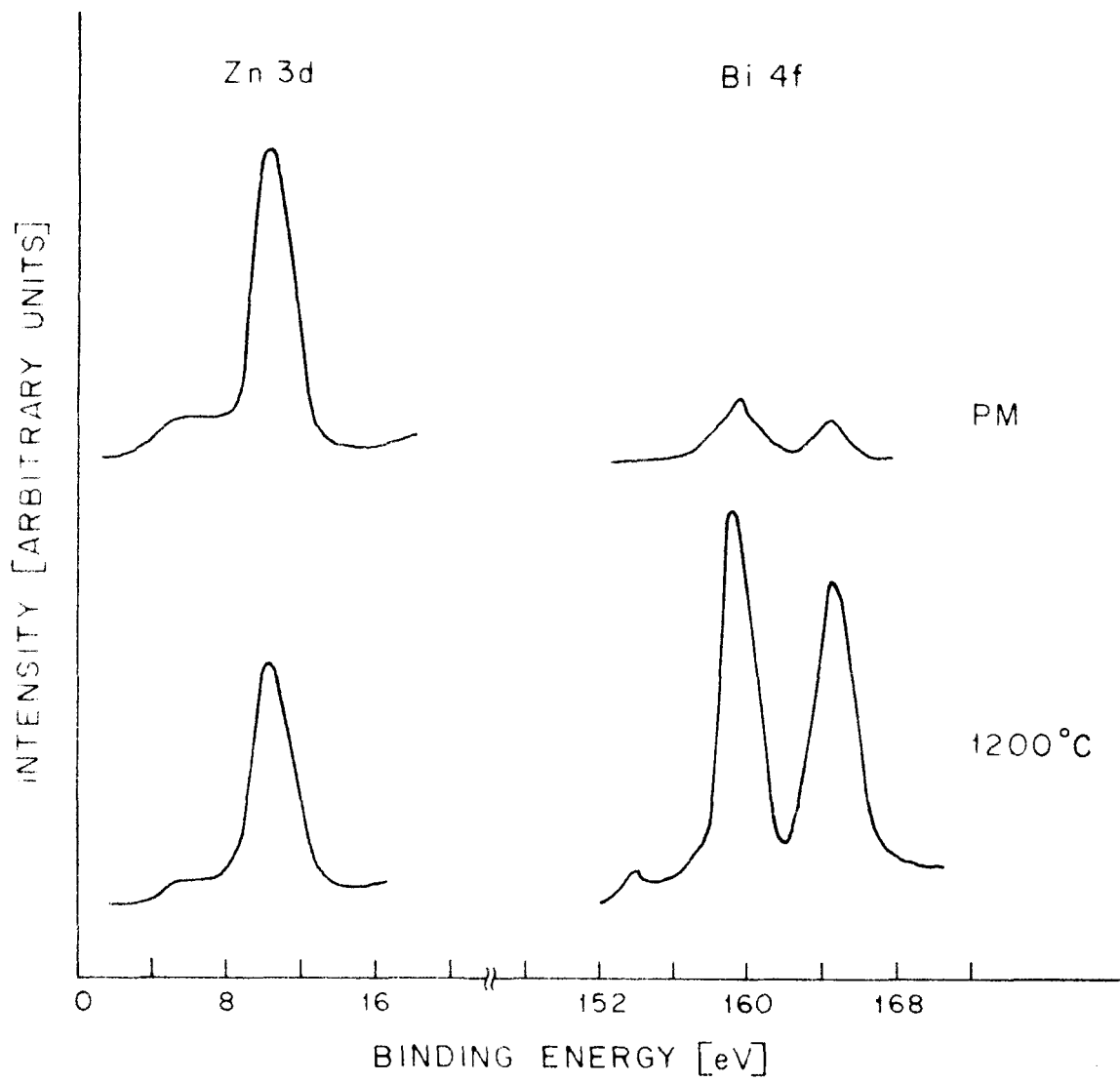


FIG. 3-2 : Zn 3d AND Bi 4f ELECTRON SPECTRA OF A (ZB) PELLETT BEFORE AND AFTER SINTERING .

intensity of Zn peak decreases due to sintering. No binding energy shift was observed in Zn-3d and Bi-4f XPS peaks (table 3.2) before or after sintering the ZB pellets, therefore it is concluded that there is no chemical change taking place in ZnO and Bi_2O_3 after sintering. To differentiate between a bulk migration or a grain boundary migration, the same sample was analysed after (a) fracturing the pellet and exposing the inner surface and (b) by grinding the pellet in a mortar and loading the powder sample on to the gold wire mesh of the sample holder. Exactly similar results were obtained from the fractured surface as well as from the powder samples and these results are shown in table 3.2. Migration of Bi_2O_3 , therefore, is not a bulk process but it is taking place at the boundaries of ZnO grains. Similarly, on grinding or fracturing, the cleavage takes place along the old grain boundaries, so that the ZnO grains still remain coated with Bi_2O_3 . This confirms the formation of intergranular layer enriched in Bi_2O_3 due to sintering of ZnO- Bi_2O_3 pellet at 1200°C .

In order to understand the migration of Bi_2O_3 in detail (i.e. the chemical nature of the intergranular layer), the X-ray photoelectron (XPS) spectra were recorded after crushing the ZB pellets, sintered at various temperatures and the results are shown in fig. 3.3. The peaks have been

Table 3.2 : XPS results of a 2B pellet before and after sintering at 1200°C

Sample	Binding energy of XPS peaks (eV)		Intensity of XPS peaks (10 ⁴ c.p.s.)		Intensity ratio
	Zn-3d	Bi-4f	Zn-3d	Bi-4f	Zn-3d Bi-4f
PM*	10.2	159.6	4.20	0.80	5.25
Pellet surface (as sintered)	10.2	159.7	3.20	4.80	0.66
Fractured pellet	10.2	159.6	1.20	4.20	0.29
Powder after grinding the sintered pellet	10.2	159.6	1.35	4.70	0.29

* PM - physical mixture before sintering

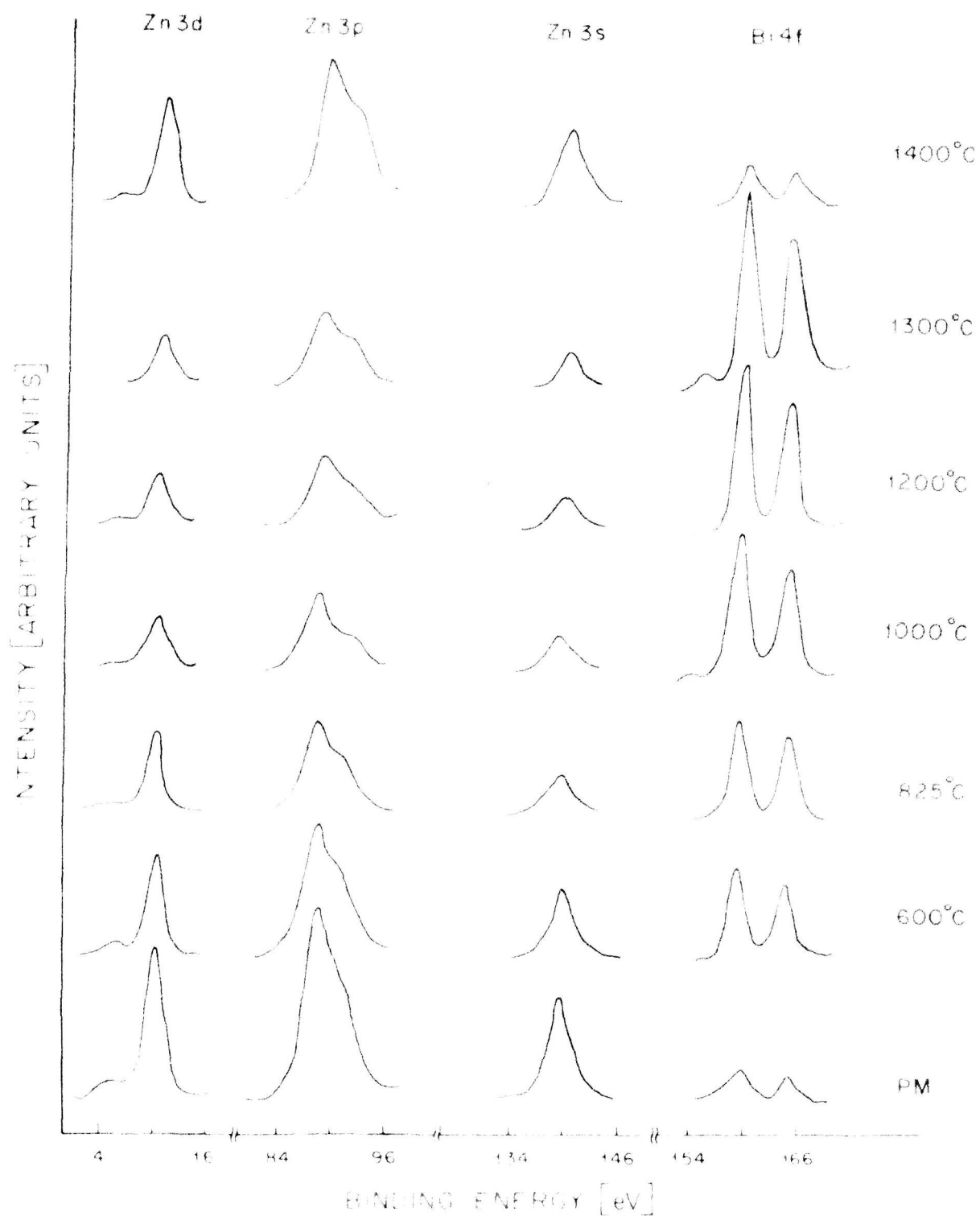


FIG. 3-3 . XPE-SPECTRA FOR (ZB) PELLETS SINTERED AT VARIOUS TEMPERATURES .

identified and assigned to Zn-3d, Zn-3p, Zn-3s, Bi-4f_{7/2} and Bi-4f_{5/2}. We have also recorded the Zn Auger peaks excited by AlK_α X-rays because the shift in the kinetic energy of Auger peaks is more than the binding energy shifts of XPS peaks for zinc metal and its oxides. For example, the binding energy of Zn-3d XPS peak shifts from 9.4 for Zn to 10.2 eV for ZnO, whereas the kinetic energy of Zn-L_{II}M_VM_V Auger peak shifts from 1015.6 to 1012.0 eV [188]. That is, the XPS binding energy shifts by 0.8 eV whereas the Auger kinetic energy shifts by 3.6 eV which helps in the identification of chemical nature easily. These X-ray excited Auger electron (XAES) peaks are distinguished from the XPS peaks by recording the spectra using the twin anode X-ray source (AlK_α hν = 1486.6 eV and MgK_α hν = 1253.6 eV) and the results are shown in fig. 3.4. It is clearly seen that the Auger peaks have been shifted by 233.0 eV on the binding energy scale whereas the XPS peaks have remained stationary.

From the XPS spectra of ZB varistor pellets sintered at various temperatures (fig. 3.3), it is clearly seen that the Bi XPS peaks increase whereas the Zn XPS and the Zn Auger peaks decrease in intensity as the sintering temperature increases. Contrary to the earlier observation, (M. Matsuoka's conclusion from the SEM results [29]) Bi₂O₃

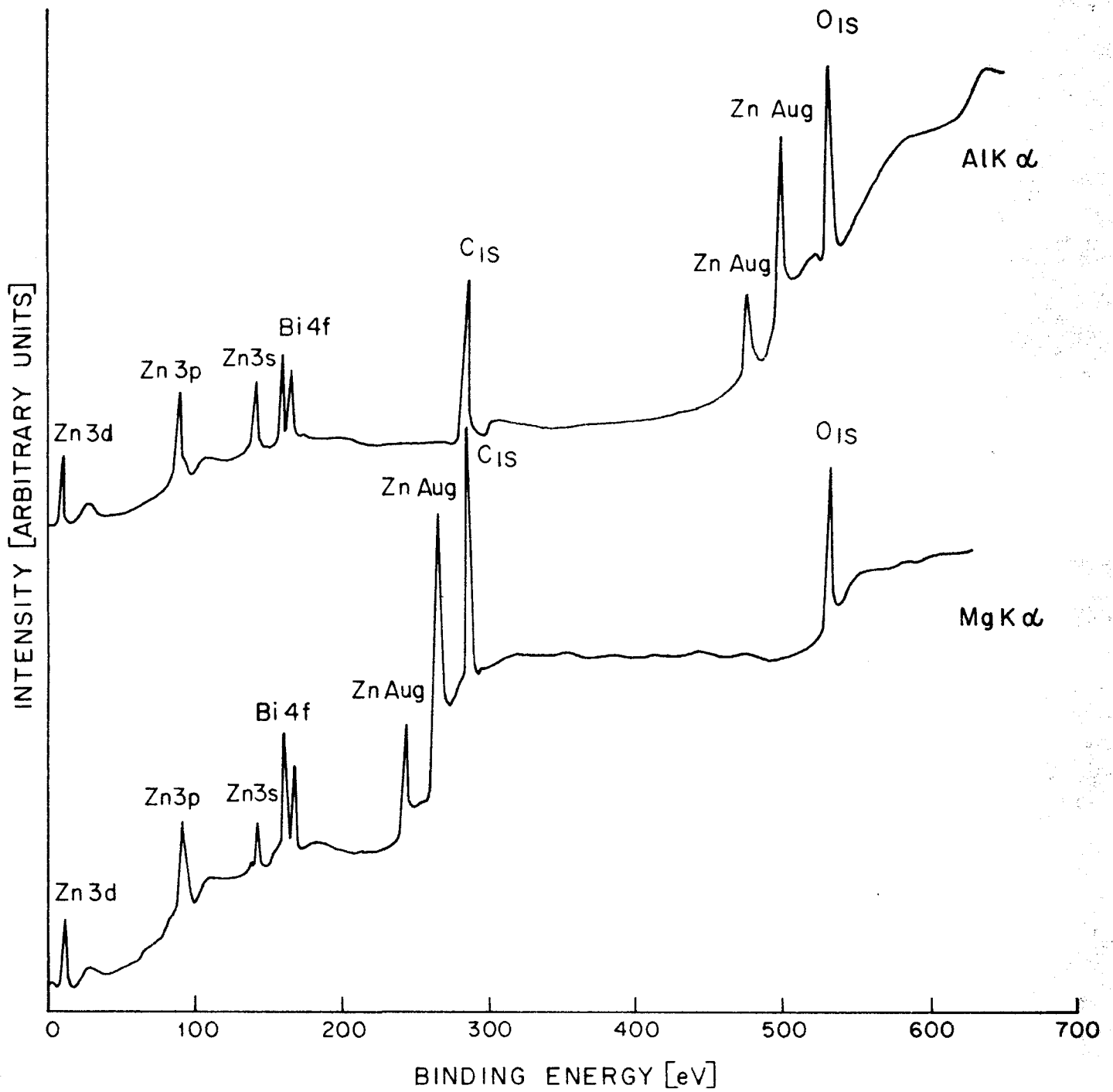


FIG. 3-4 : XPE - SPECTRA OF (ZB) PELLETT USING MgK α AND AlK α X-RAY SOURCES.

migration to the intergranular layer separating ZnO grains starts even at 600°C and progressively becomes pronounced at higher sintering temperatures, as seen clearly from the increase in the intensities of the characteristic Bi peaks in comparison with that of the Zn peak intensities given in table 3.3. To get a clear idea about the variation of Zn and Bi XPS peak intensities, Zn/Bi peak intensity ratios are given in table 3.4 and the variation of these intensity ratios as a function of sintering temperatures are plotted in fig. 3.5. Bi peak intensity is maximum and Zn peak intensity is minimum in other words, Zn/Bi intensity ratio is minimum for pellets sintered at 1300°C, which show that the migration of Bi₂O₃ to the intergranular layer separating ZnO grains is maximum at 1300°C. Similarly the α -value and density are also maximum at 1300°C (see table 3.1). It is thus clearly shown that at this sintering temperature, densification and maximum migration of Bi₂O₃ at grain boundary are more or less complete to give the maximum value of α .

When a pellet of the ZB varistor system is sintered at 1400°C, the Bi peaks suddenly decrease in intensity (simultaneously Zn peak intensity increases). It is reasonable to explain the sudden increase in the intensity ratio on the basis of a loss in Bi₂O₃ due to its sublimation from the surface. In fact there is a continuous loss of

Table 3.3 : XPS peak intensities from the ZB pellets
sintered at various temperatures (10^4 cps)

Sintering temperature $^{\circ}\text{C}$	Zn-3d	Zn-3p	Zn-3s	Zn-Auger Li, Mn, V	Zn-Auger Bi, Fe, Mn, V	Bi-4f $_{7/2}$	Bi-4f $_{5/2}$
PM	4.20	5.40	2.80	6.30	13.50	0.80	0.60
600	2.70	3.70	1.90	4.30	10.00	2.60	2.00
825	2.20	2.50	1.20	3.10	7.80	2.80	2.40
1000	1.40	2.10	1.00	2.10	5.40	4.00	3.00
1200	1.35	2.00	0.90	1.70	4.60	4.70	3.70
1300	1.30	1.95	0.90	1.50	4.00	5.30	4.20
1400	2.80	4.00	2.00	4.60	10.60	1.20	0.90

Table 3.4 : XPS peak intensity ratios for the Zn pellets sintered at various temperatures

sinter- ing tempe- rature °C	<u>Zn-3d</u>	<u>Zn-3p</u>	<u>Zn-3s</u>	<u>Zn-Auger</u>	<u>Zn-Auger</u>
	Bi-4f _{7/2}	Bi-4f _{7/2}	Bi-4f _{7/2}	L _{II} M _V M _V	L _{III} M _V M _V
				Bi-4f _{7/2}	Bi-4f _{7/2}
PM	5.25	6.75	3.50	7.88	16.88
600	1.04	1.42	0.73	1.65	3.85
825	0.79	0.89	0.43	1.10	2.79
1000	0.35	0.53	0.25	0.53	1.35
1200	0.29	0.43	0.20	0.36	0.98
1300	0.25	0.36	0.17	0.28	0.75
1400	2.33	3.33	1.66	3.83	8.83

PM - physical mixture before sintering.

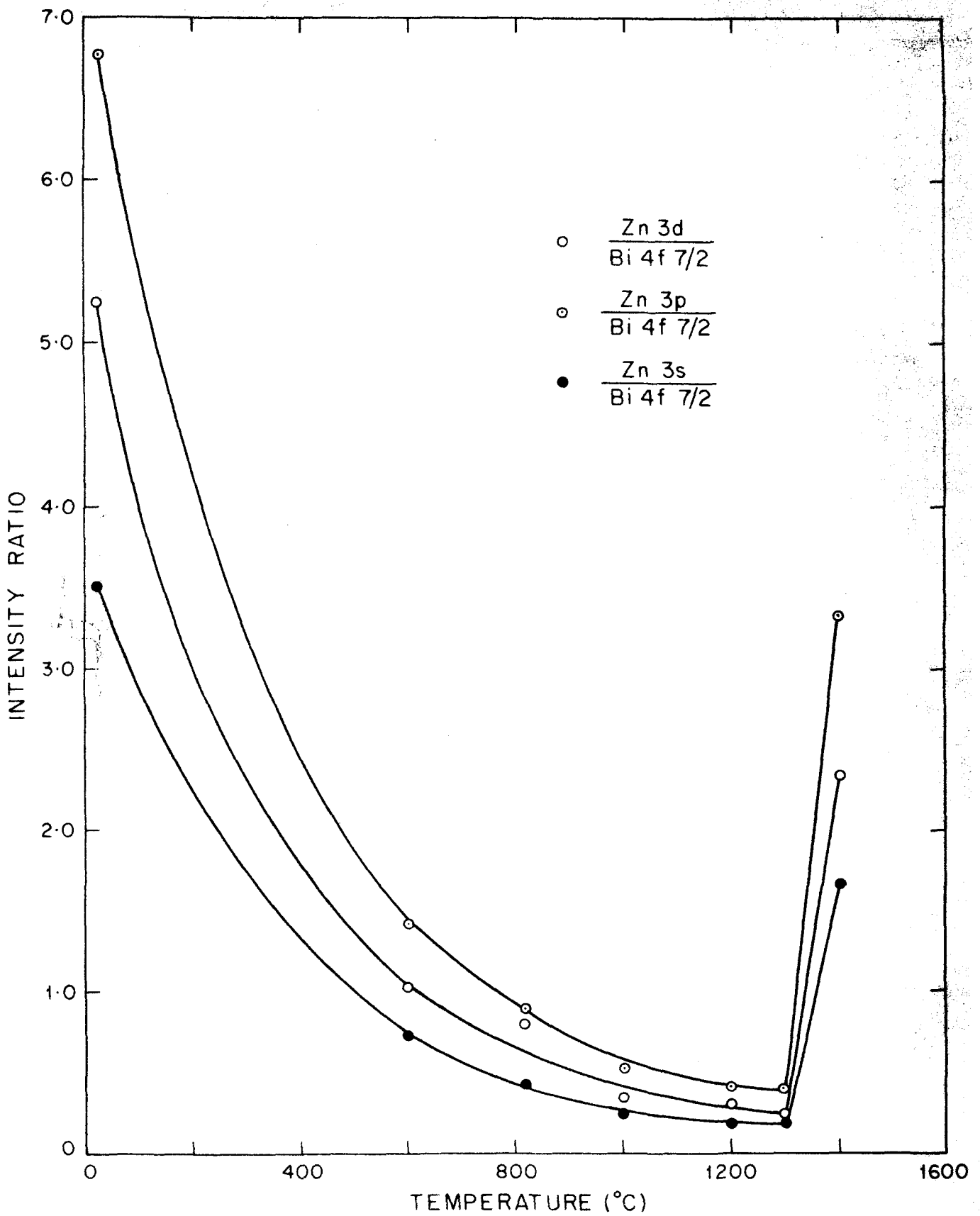


FIG. 3.5 : Zn/Bi XPS PEAK INTENSITY RATIO AS A FUNCTION OF SINTERING TEMPERATURE OF (ZB) PELLETS.

Bi_2O_3 from the surface layers during the sintering process at higher temperatures, as is seen clearly by comparing the intensity ratios of the surface of the sintered pellet and the powder sample (table 3.2). Indirectly due to the loss of Bi_2O_3 from the surface layers the fresh ZnO surface layers are exposed to the X-ray excitation, culminating in the rise in intensity of the Zn peaks.

There is no XPS binding energy shift of Zn and Bi lines or no kinetic energy change in Zn Auger lines (table 3.5) thereby confirming that no new phase has been formed after sintering.

From the above studies, the migration of Bi_2O_3 on ZnO grains which plays an important role to achieve the unusual non-linear varistor property is experimentally supported.

3.1.3 Scanning electron microscopy (SEM) and electron probe micro analysis (EPMA)

To understand the varistor mechanism and micro-structure, and to check the XPS conclusions, ZB varistor samples prepared for this work are also characterized by scanning electron microscopy. The EPMA coupled to SEM was used to know the elemental distribution in the micro-structure of the varistor pellet. Fig. 3.6 shows the scanning electron micrograph (X1000 magnification) of a ZB

Table 3.5 : XPS binding energy and XAE kinetic energy of the Zn pellets sintered at various temperatures

Sintering temperature °C	XPS binding energy (eV)			XAE kinetic energy (eV)				
	Zn-3d	Zn-3p	Zn-3s	Bi-4f _{7/2}	Bi-4f _{5/2}			
PM	10.2	88.8	139.6	159.8	165.0	Zn-Auger L _{II} M _{IV} V	Zn-Auger L _{II} M _{IV} V	988.6
600	10.3	83.9	139.7	159.6	164.3			983.8
825	10.3	88.8	139.6	159.8	165.0			988.8
1000	10.2	90.0	139.6	159.8	165.0			988.7
1200	10.3	88.8	139.6	159.7	164.9			988.8
1300	10.2	83.9	139.7	159.8	165.0			983.8
1400	10.2	88.8	139.6	159.8	165.0			983.9

PM - Physical mixture before sintering
 XPS - X-ray photoelectron
 XAE - X-ray excited Auger electron

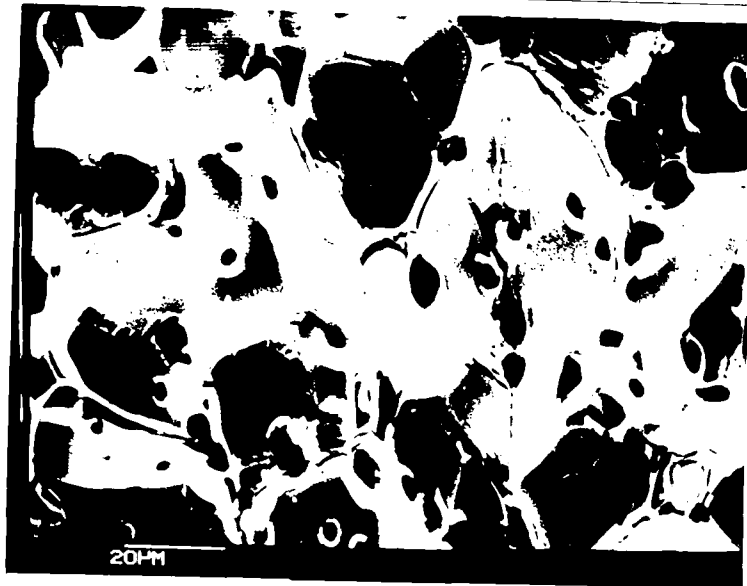
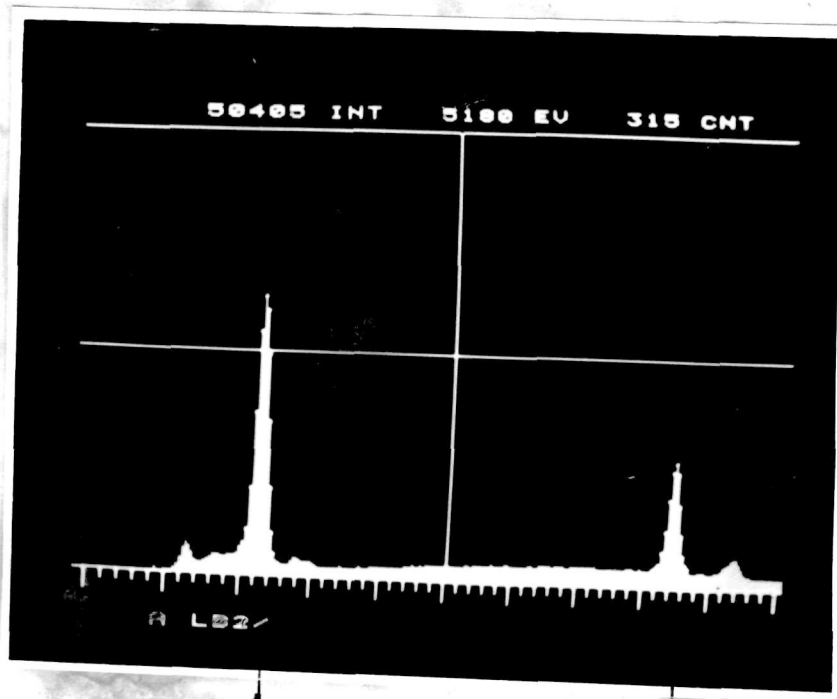


Fig. 3.6 : Scanning electron micrograph of a ZrB pellet
sintered at 1300°C.

pellet sintered at 1300°C. It can be clearly seen from the micrograph that the big grains of about 20-30 microns are separated by a thin layer, the so-called intergranular layer in the literature. The elemental microanalysis of these big grains and the intergranular layer was carried out by the EPMA technique.

The characteristic X-rays generated in the sample by an electron beam, are detected by the silicon-lithium solid state energy dispersive detector which measures the X-ray energy directly and produces a spectrum of counts versus energy as shown in fig. 3.7. The characteristic X-ray spectrum for the total area (shown in micrograph of fig. 3.6) is recorded and shown in fig. 3.7(a). The spectrum clearly shows that the intensity of ZnK_α peak (at energy 8.630 KeV) is more whereas the intensity of BiM_α peak (at energy 2.418 KeV) is less as is expected from the composition. The spectrum shows some more peaks belonging to AlK_α (1.486 KeV) coming from aluminium sample stub and AgL_α (at energy 2.984 KeV) coming from the silver deposited on the sample surface for avoiding the charging of the sample. The integral values (i.e. total number of counts under the peaks after fixing the energy window, 2.28 KeV to 2.70 KeV for BiM_α and 8.34 KeV to 8.96 KeV for ZnK_α) for bismuth and zinc and integral ratios Zn/Bi for the ZB pellet sintered at 1300°C are given in table 3.6.



(c)

Bi M α

Zn K α

Fig. 3.7 : Energy dispersive analysis of X-rays (EDAX) spectra of a ZB pellet sintered at 1300°C, electron probe on—(a) total surface area covered in micrograph fig. 3.6, (b) big grain (c) intergranular layer.

Table 3.6 : EPMA RESULTS OF A ZB PELLETT SINTERED AT 1300°C AT VARIOUS PLACES

Place of analysis	ZnK _α integral	BiM _α integral	Integral ratio Zn/Bi
Total surface area covered in fig. 3.6	2,20,976	35,642	6.20
Probe on a big grain	2,09,708	5,765	36.38
Probe on an intergranular layer	73,342	1,49,573	0.49

When an electron probe is placed on the big grain of the micrograph (fig. 3.6) and the characteristic X-ray spectrum obtained is shown in fig. 3.7(b). It is clearly seen from this spectrum, there is a tremendous decrease in intensity of the BiM_α peak. It is, therefore, concluded that the big grain belongs to ZnO. However, when electron probe is placed at the intergranular layer, the spectrum obtained (fig. 6(c)) shows an increase in the BiM_α peak intensity and a decrease in the ZnK_α peak intensity (table 3.6). Hence it is concluded that intergranular layer belongs to Bi_2O_3 -rich phase. The melting point of Bi_2O_3 is 825°C [31] and that of ZnO is 1970°C [31] and they are separated by over 1150°C . The sintering of ZnO- Bi_2O_3 pellets in the temperature range 1000 - 1400°C is therefore a liquid-phase sintering. At these temperatures Bi_2O_3 melts and goes into liquid phase which flows between the ZnO grains and when the sample is cooled to room temperature it solidifies and remains in solid state between the ZnO grains. We can therefore see in the scanning electron micrograph (fig. 3.6) big grains of ZnO separated by a thin layer of Bi_2O_3 .

Zinc oxide is an n-type semiconductor material having a good electrical conductivity (the resistivity is typically 1 ohm-cm at 25°C) [32,37], whereas Bi_2O_3 is a highly resistive material (the resistivity $> 10^8$ ohm-cm at 25°C) [38,39]. The voltage applied to this ZB varistor pellet

is therefore concentrated at the highly resistive Bi_2O_3 intergranular layer which is responsible for the non-ohmic property of these varistors.

In order to understand the growth kinetics of Bi_2O_3 rich intergranular layer as a function of the sintering temperature, the scanning electron micrographs were recorded for samples of ZB pellets sintered at various temperatures. The micrographs are shown in fig. 3.8 and their EPMA results are given in table 3.7. From the micrographs, it is clearly seen that as the sintering temperature increases, the ZnO grain growth increases slowly upto 1000°C and then rapidly after 1200°C . Similarly the features of intergranular layer are clearly visible from 1200°C and become prominent at 1300°C . The thickness of the intergranular layer is maximum at 1300°C , where α value is also maximum. The thickness of the intergranular layer therefore plays an important role to get the maximum non-linear property of these varistors.

A SEM micrograph (fig. 8(e)) of a similar pellet from the same batch sintered at 1400°C clearly shows a reduction of intergranular ^{layers} presumably due to the vapourization of Bi_2O_3 at higher temperatures. The α -value also decreases possibly due to reduction in the thickness of the intergranular layer.

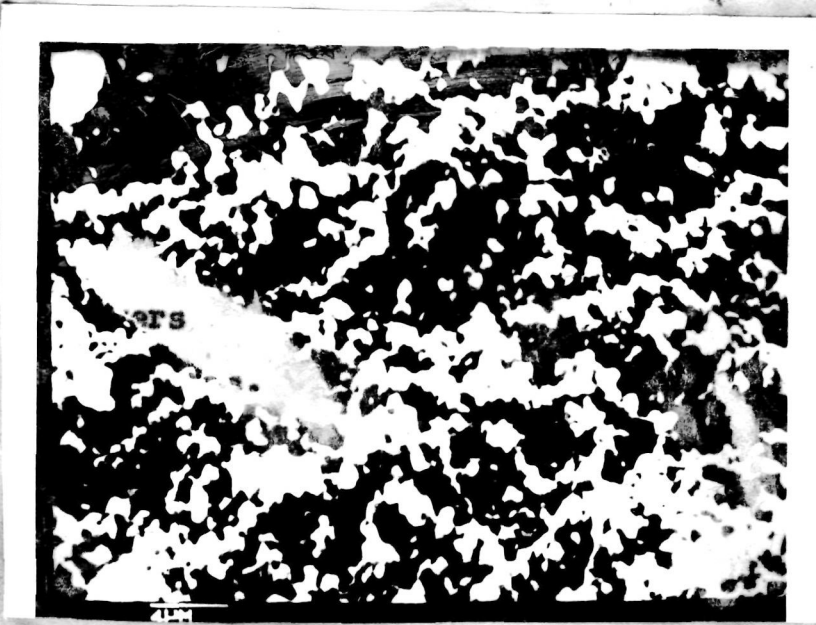
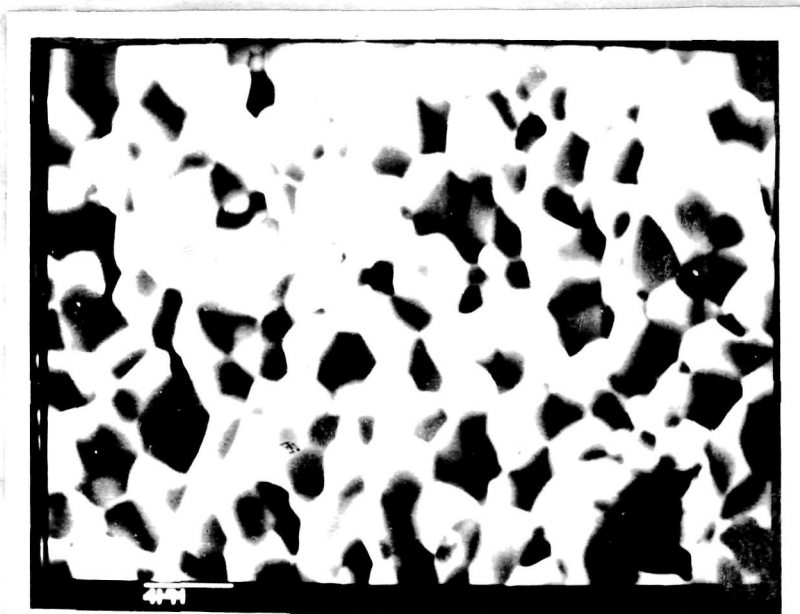


Fig. 3.8

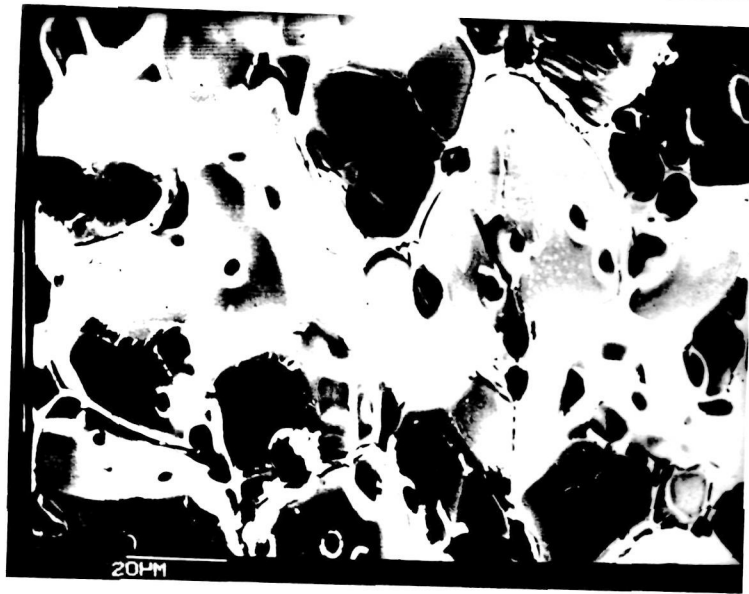
(a)



(b)



(c)



(d)



(e)

Fig. 3.8 : Scanning electron micrographs for the
ZB pellets sintered at (a) 825°C (b) 1000°C
(c) 1200°C (d) 1300°C (e) 1400°C

Table 3.7 : XPM results and grain size of the
ZB pellets sintered at various
temperatures

Sintering temperature °C	Integral		Integral ratio Zn/Bi	Grain size (micron)
	ZnK _α	BiM _α		
PM	88,483	3,744	23.63	< 1
600	1,14,192	4,886	23.37	< 1
825	1,37,262	5,990	22.92	1-2
1000	1,40,660	6,579	21.37	3-5
1200	1,57,469	23,381	6.74	15-20
1300	1,45,478	23,388	6.22	15-20
1400	1,33,040	724	183.76	15-20

PM - physical mixture before sintering.

Table 3.7 shows changes in the integral ratios of Zn/Bi at various sintering temperatures of ZB varistor pellets. It is clearly seen from the Zn/Bi integral ratio that the migration of Bi_2O_3 slowly takes place upto 1000°C and suddenly increases in the temperature range $1200-1300^\circ\text{C}$. The ratio becomes minimum at 1300°C indicating the formation of Bi_2O_3 rich intergranular layer separating ZnO grains. The Zn/Bi integral ratio increases tremendously for pellets sintered at 1400°C confirming the volatilization loss of Bi_2O_3 from the ZnO surface.

It can be clearly seen that the grain size and thickness of intergranular layer rich in Bi_2O_3 play an important role to achieve the maximum value of α .

3.1.4 X-ray diffraction (XRD) study

In order to look for any phase changes taking place in the (ZB) varistor pellets sintered at different temperatures, the ZB pellets were characterized by the X-ray diffraction technique. The 'd' values and intensities are given in table 3.8. There are no additional lines observed in the XRD spectrum of the sintered pellets. To get a better idea about the Bi_2O_3 phase, samples containing 1 % and 5 % Bi_2O_3 were prepared and sintered at different temperatures. It can be seen that the samples containing 0.5 % Bi_2O_3 show, after sintering at 1300°C , line due to cubic Bi_2O_3 whereas the ones

Table 3.8 : XRD results of the 2B pellets sintered at various temperatures

PM	600°C		825°C		1000°C		1200°C		1300°C		1400°C		
	d Å	I/I ₁	d Å	I/I ₁	d Å	I/I ₁	d Å	I/I ₁	d Å	I/I ₁	d Å	I/I ₁	
2.81	63.6	2.81	59.1	2.80	67.7	2.80	70.7	2.82	70.0	2.79	70.5	2.78	62.5
2.60	44.6	2.60	44.3	2.59	27.6	2.59	27.6	2.61	26.0	2.58	25.6	2.58	30.0
2.47	100	2.47	100	2.47	100	2.47	100	2.48	100	2.46	100	2.45	100
1.91	22.3	1.91	21.6	1.91	17.3	1.90	18.1	1.91	17.0	1.90	20.3	1.90	22.5
1.62	34.2	1.62	31.3	1.62	34.6	1.62	34.5	1.63	33.0	1.62	33.3	1.62	48.8
1.48	27.2	1.48	27.3	1.47	21.3	1.47	20.7	1.48	20.5	1.47	23.4	1.47	25.0

containing more Bi_2O_3 give rise to α -(monoclinic) Bi_2O_3 . Thus when Bi_2O_3 is crystallised from the molten phase on cooling the sample from the temperature greater than 1000°C , the bismuth oxide can crystallise to either the cubic (γ) phase or the monoclinic (α) phase. In the absence of any other stabilizing oxide, the tendency is towards the more stable monoclinic phase and only a small portion (0.5 % of the total weight) crystallises in the cubic phase. This is presumably the layer surrounding the grains of ZnO . The extra Bi_2O_3 which crystallises in the monoclinic phase segregates to small discontinuous crystallites and is therefore not effective in improving the non-ohmic characteristics of the systems. The only way of getting high non-linearity, therefore, resides in stabilizing the cubic phase in competition to the other more stable monoclinic (α) phase when Bi_2O_3 is crystallizing from the molten state. The cubic phase apparently has the property of maintaining the thin intergranular layer like in the liquid Bi_2O_3 , which property the (α) monoclinic form may not have.

This stabilization is not obtained merely by the dissolution of ZnO in Bi_2O_3 in a small proportion as is claimed in the literature. If that was so, there was no reason why the entire 5 % Bi_2O_3 added in (ZB) systems did not crystallise in the cubic phase. It looks that cubic oxides such as MnO or CoO which crystallise in the face centred cubic sodium chloride structure tends to stabilize γ - Bi_2O_3 . This conclusion is borne out by the findings for the (ZBC) systems discussed latter.

3.2 ZnO + Sb₂O₃ (ZS) VARISTOR SYSTEM

3.2.1 I-V characteristics

The current voltage characteristics of ZS pellets sintered at different temperature from 500°C to 1200°C are measured at room temperature and the results are plotted in fig. 3.9 (log V vs log I). From these I-V plots, it is seen that the non-linearity increases with sintering temperature and it is maximum at 660°C, then starts decreasing with further increase in the sintering temperature. The I-V characteristics become almost linear for samples sintered at 900°C. At still higher sintering temperatures the I-V curve starts becoming non-linear and the non-linearity reaches a maximum at 1100°C and again decreases at 1200°C. This is more clearly seen from the computed non-linear exponent α -values using equation (2.2), which are given in table 3.9.

The non-linear constant 'C' calculated from the I-V plots at different sintering temperatures are also given in table 3.9. It is seen to decrease in value upto 600°C, then to remain constant in the temperature range of 660°C-900°C and then again to drop at 1000°C and continue to decrease upto 1200°C. The non-linear constant 'C' for the ZB pellet sintered at 1200°C is 10 times more than the ZS pellet sintered at the same temperature, and this is because the resistivity of Bi₂O₃ is much more than that of the Sb₂O₃.

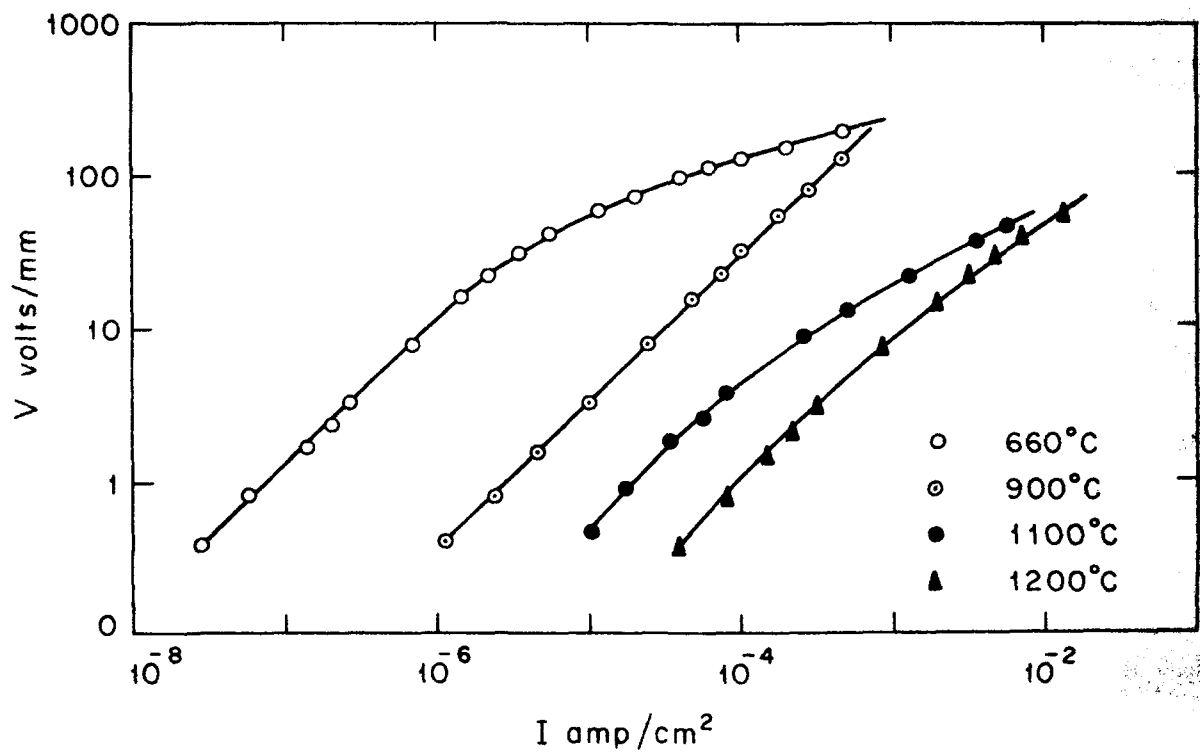
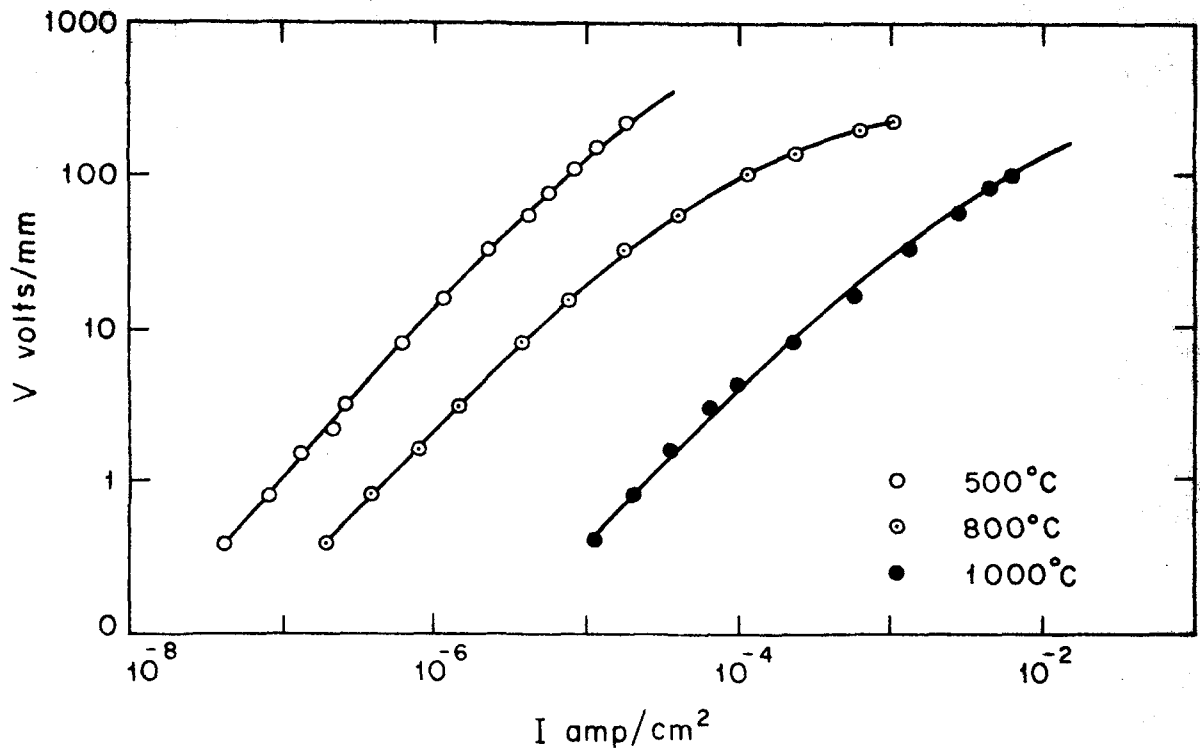


FIG. 3-9 : I-V CHARACTERISTICS OF (ZS) PELLETS SINTERED AT VARIOUS TEMPERATURES.

Table 3.9 : Values of α , C and density of
ZS pellets sintered at various
temperatures

Sintering temperature $^{\circ}\text{C}$	Non-linear exponent ' α '	Non-linear constant 'C' (V/mm at 1 mA)	Pellet density (g/cm ³)
500	1.1	4.2×10^3 *	3.08
660	4.0	240	3.08
800	2.5	240	3.10
900	1.3	240	3.10
1000	2.0	28	3.16
1100	4.0	18	3.24
1200	2.2	9	4.40

* extrapolated value

The density measured for the ZS pellets sintered at various temperatures are also given in Table 3.9. It does not change upto 1000°C, it increases slowly from 1000-1100°C and then rapidly from 1100-1200°C. The density of ZB pellets sintered at 1200°C is much higher (92.8 % of the theoretical density of ZnO) than the density of ZS pellets sintered at the same temperature (77.0 % of the theoretical density of ZnO), which shows that Bi₂O₃ helps more in sintering and densification than Sb₂O₃.

3.2.2 Electron spectroscopic study

As in the case of the ZB systems, the X-ray photoelectron spectra are recorded in a similar way after crushing the ZS pellets sintered at various temperatures which are shown in fig. 3.10. The peak intensities measured from these spectra are given in table 3.10. Similarly Zn/Sb intensity ratios are given in table 3.11 and the variation of these ratios as a function of the sintering temperatures for ZS pellets are shown in fig. 3.11. It is clearly seen from these results that the intensity of Sb XPS peaks increases and that of all Zn XPS and Zn XAES peaks decreases as the sintering temperature increases upto 650°C and the intensity ratio Zn/Sb is minimum at 660°C. Contrary to the earlier observations [29], Sb₂O₃ migration on the ZnO grains starts even at 500°C. The concentration of Sb₂O₃ in the enriched layer at the surface reaches a maximum

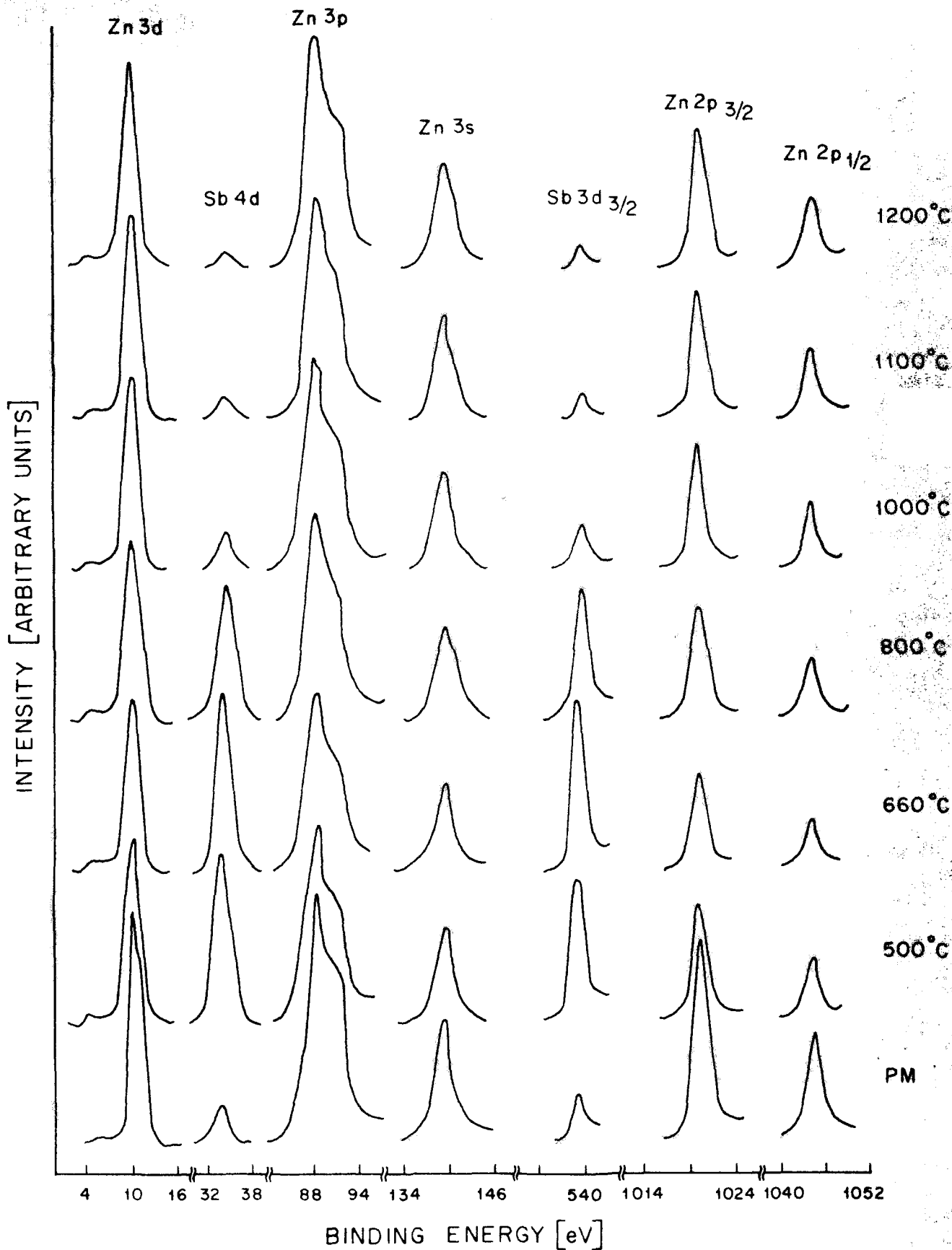


FIG. 3-10 : XPE - SPECTRA FOR (ZS) PELLETS SINTERED AT VARIOUS TEMPERATURES.

Table 3.10 : XPS peak intensities from the 23 pellets sintered at various temperatures (10^4 cps)

Sintering temperature $^{\circ}\text{C}$	Zn-3d	Zn-3p	Zn-3s	Zn-2p _{3/2}	Zn-2p _{1/2}	Zn-Auger L _{II} M _{IV} M _V	Zn-Auger L _{III} M _{IV} M _V	Sb-4d	Sb-3d _{3/2}
PM	7.7	8.3	3.9	66.0	33.0	10.5	22.8	1.2	4.2
500	6.0	6.6	3.0	38.0	19.0	8.1	18.3	5.5	13.8
650	5.6	5.9	2.8	30.0	15.0	7.5	16.2	5.9	16.8
800	5.9	6.5	3.0	36.0	18.0	8.1	19.2	4.4	12.6
1000	6.3	6.8	3.2	40.0	20.0	8.4	19.5	1.2	4.2
1100	6.6	7.2	3.4	42.0	21.0	8.7	20.4	0.7	2.4
1200	6.8	7.6	3.5	45.0	22.5	9.0	21.0	0.5	1.8

Table 3.11 : XPS peak intensity ratios for the 23 pellets
sintered at various temperatures

Sintering tempera- ture °C	Zn-3d	Zn-3p	Zn-3s	Zn-2p _{3/2}	Zn-2p _{1/2}	Zn-Auger	Zn-Auger
	Sb-3d _{3/2}	Sb-3d _{3/2}	Sb-3d _{3/2}	Sb-3d _{3/2}	Sb-3d _{3/2}	L _{II} M _V	L _{III} M _V M _V
PM	1.83	1.98	0.93	15.71	7.86	2.50	5.43
500	0.44	0.48	0.22	2.75	1.38	0.59	1.33
660	0.33	0.35	0.17	1.79	0.89	0.45	0.96
800	0.47	0.52	0.24	2.86	1.43	0.64	1.52
1000	1.50	1.62	0.76	9.52	4.76	2.00	4.64
1100	2.75	3.00	1.42	17.50	8.75	3.63	8.50
1200	3.78	4.22	1.89	23.33	12.50	5.00	11.67

PM - Physical mixture before sintering.

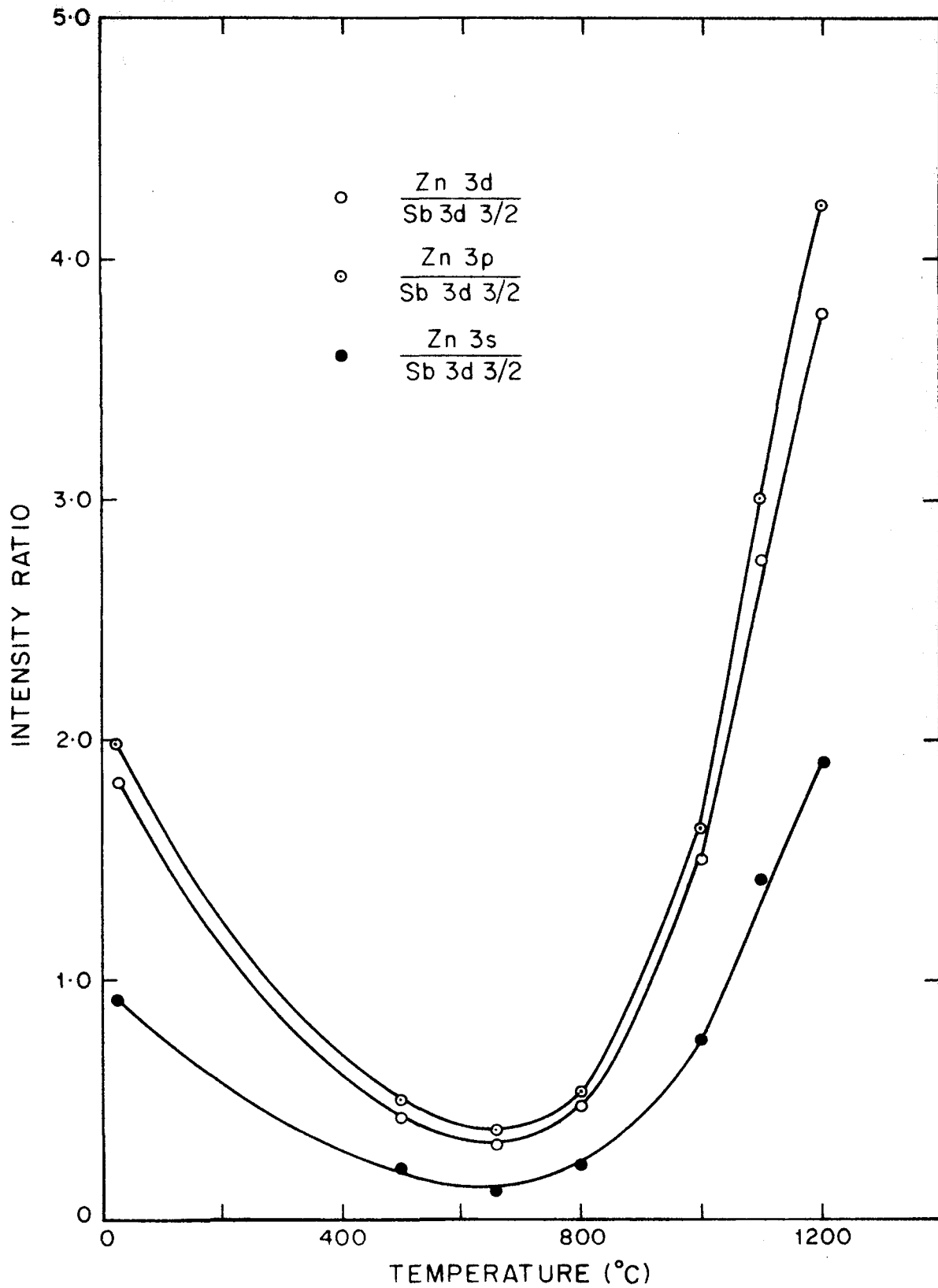


FIG. 3.11 : Zn/Sb XPS PEAK INTENSITY RATIO AS A FUNCTION OF SINTERING TEMPERATURE OF (ZS) PELLETS .

at around 660°C . On the other hand, more and more ZnO grains get coated with Sb_2O_3 enriched intergranular layer thereby decreasing the intensity of Zn peaks. As the sintering temperature increases to about 800°C , the intensity of the Zn peaks starts increasing whereas the intensity of the Sb peaks starts decreasing. This decrease in the intensity of Sb peaks may be either due to the evaporation of Sb_2O_3 from the surface and/or Sb_2O_3 diffusing into the ZnO grains due to reaction of ZnO and Sb_2O_3 and forming another phase. It may be recalled that in the case of ZB system the Bi_2O_3 was found to evaporate above 1400°C which was confirmed from the facts that there was no shift in the binding energy values as seen from the XPS peaks, and that there were no extra lines observed in the XRD. It was thus concluded that no phase change was taking place in ZB system and thus the fall in the XPS peak intensity of Bi_2O_3 at the sintering temperature above 1400°C was due to the evaporation of Bi_2O_3 . However in this ZS varistor system sintered at higher temperature ($> 800^{\circ}\text{C}$) a shift in the binding energy values of the Sb peaks has been observed but no shift in the Zn peaks. The binding energy values for ZS system sintered at various temperatures are measured from the XPS spectra and are given in table 3.12. The Sb- $3d_{3/2}$ binding energy changes from 539.2 eV to 540.0 eV at higher temperatures.

Table 3.12 : XPS binding energy and XAS kinetic energy of the 4S pellets sintered at various temperatures

Sintering temperature °C	XPS binding energy (eV)				XAS kinetic energy (eV)				
	Zn-3d	Zn-3p	Zn-3s	Zn-2p _{3/2}	Sb-4d	Sb-3d _{3/2}	Zn-Auger L _{IIIM_{IV}M_V}	Zn-Auger L _{IIIM_{IV}M_V}	
PM	10.2	88.8	139.6	1021.4	1044.6	34.2	539.2	1012.0	988.8
500	10.3	88.9	139.8	1021.2	1044.4	34.2	539.2	1012.0	988.9
660	10.2	88.8	139.6	1021.4	1044.6	34.1	539.1	1011.9	988.7
800	10.2	88.7	139.6	1021.4	1044.6	34.3	539.3	1012.0	988.9
1000	10.4	88.9	139.6	1021.2	1044.4	35.0	540.0	1012.1	989.9
1100	10.3	90.0	139.8	1021.4	1044.6	35.0	540.0	1012.0	988.8
1200	10.2	88.8	139.6	1021.4	1044.6	35.0	540.0	1012.0	988.8

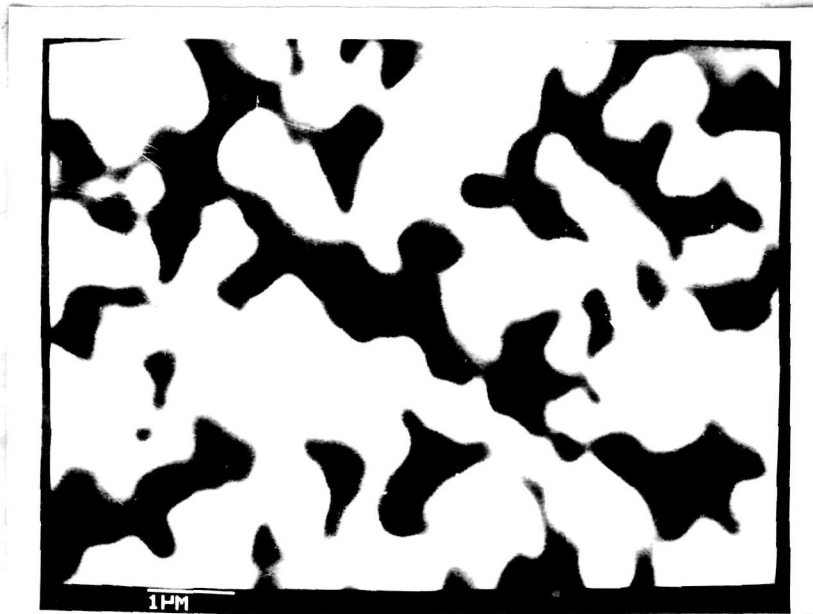
This shift of 0.8 eV confirms that antimony changes from Sb^{3+} to Sb^{5+} because the observed value of 540.0 eV matches the binding energy for Sb^{5+} [83].

3.2.3 Scanning electron microscopy and electron probe microanalysis

Samples of ZS system sintered at various temperatures have been examined by the SEM in a way similar to the earlier ZB samples. It has been observed from the micrograph that the grain size of these pellets sintered upto $1000^{\circ}C$ is very small ($\ll 1$ micron). It was therefore difficult to get details of the microstructure of these pellets.

The scanning electron micrographs at very high magnification (X20,000) for samples sintered at 1100 and $1200^{\circ}C$ are shown in fig. 3.12. From these micrographs it is clearly seen that a definite grain growth of ZnO (hexagonal) starts taking place above $1200^{\circ}C$ at which temperature the density also increased. No definite grain boundary segregation of Sb_2O_3 is observed.

The energy dispersive X-ray analysis of these pellets has been carried out and the values of the X-ray integral for ZnK_{α} and SbL_{α} and their ratios are given in table 3.13. It is seen that the integral ratio (Zn/Sb) decreases as



(a)



(b)

Fig. 3.12 : Scanning electron micrographs of the
ZS pellets sintered at (a) 1100°C (b) 1200°C .

Table 3.13 : EPMA results and grain size of
the ZS pellets sintered at
various temperatures

Sintering temperature °C	Integral		Integral ratio Zn/Sb	Grain size (micron)
	ZnK _α	SbL _α		
PM	1,08,698	3,260	33.34	< 1
500	1,32,932	4,517	29.43	< 1
660	1,53,543	5,455	28.15	< 1
800	1,53,601	4,928	31.17	< 1
900	1,45,506	4,646	31.32	< 1
1000	1,54,641	4,644	33.30	< 1
1100	1,70,190	5,067	33.60	1
1200	1,66,337	4,895	33.98	2

sintering temperature increases upto 660° , and the ratio is minimum i.e. the migration is maximum at 660°C . The ratio of Zn/Sb integral increases slowly as sintering temperature increases. As the electron probe microanalysis technique analyses upto a few micron depth, the Sb diffusing into the ZnO grains is also detected, therefore the ratio does not exceed the value for the physical mixture before sintering. It therefore appears reasonable to conclude that Sb_2O_3 is not evaporating from the surface but it is diffusing into the ZnO grains. At higher temperatures (i.e. 1100°C) the ratio exceeds that for the starting mixture presumably due to the increase in the grain size and some evaporation of Sb_2O_3 from the surface.

The X-ray analysis spectrum of ZS pellet sintered at 1100°C is shown in fig. 3.13. No preferential concentration of Sb at the grain boundary is seen contrary to what was seen for the ZB system.

3.2.4 X-ray diffraction study

To check the formation of any new phase, XRD studies were carried out for the ZS pellets sintered at various temperatures. The 'd' values and intensities were calculated and are presented in table 3.14. These data have been compared with the standard X-ray pattern for different phases

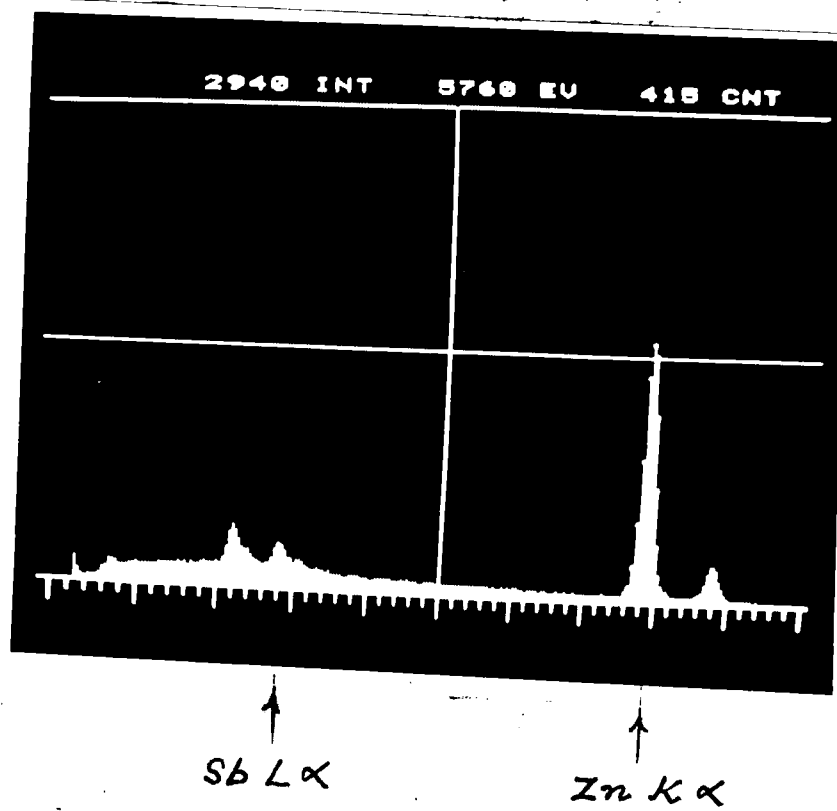


Fig. 3.13 : Energy dispersive analysis of X-rays (EDAX) spectrum of a ZnS pellet sintered at 1100°C .

Table 3.14 : XRD results of the ZS pellets sintered at various temperatures

No.	500°C		660°C		800°C		900°C		1000°C		1100°C		1200°C	
	d Å	I/I ₁	d Å	I/I ₁	d Å	I/I ₁	d Å	I/I ₁	d Å	I/I ₁	d Å	I/I ₁	d Å	I/I ₁
1	-	-	-	-	-	-	3.02	2.8	3.02	3.6	3.01	4.1	3.01	2.2
2	2.79	66.6	2.79	67.4	2.80	65.9	2.78	66.3	2.81	65.4	2.79	68.1	2.79	74.1
3	2.58	31.1	2.58	30.5	2.59	30.6	2.57	32.6	2.59	32.4	2.58	36.1	2.58	30.9
4	2.45	100	2.44	100	2.47	100	2.45	100	2.47	100	2.46	100	2.46	100
5	-	-	-	-	-	-	-	-	2.14	1.1	2.14	1.8	2.14	2.5
6	1.90	17.8	1.90	21.1	1.91	17.6	1.90	18.6	1.91	18.1	1.90	18.1	1.90	17.3
7	-	-	-	-	-	-	-	-	1.65	1.1	1.65	2.4	1.65	2.7
8	1.62	36.6	1.61	37.9	1.62	34.1	1.61	37.2	1.62	34.0	1.62	34.7	1.62	37.0
9	-	-	-	-	-	-	-	-	1.52	2.1	1.52	3.4	1.52	3.5
10	1.47	24.4	1.47	24.2	1.47	20.1	1.47	23.3	1.48	20.7	1.47	24.1	1.47	18.5

and identified phases are recorded in table 3.15. The pellets sintered above 900°C show additional lines in the XRD spectra. These extra lines can be indexed on the basis of a spinel type compound with 'a' value equal to $8.577 \pm 0.004 \text{ \AA}$. The 'd' values for observed phases are given in tables 3.16 and 3.17.

Two spinel type compounds, namely ZnSb_2O_4 and $\text{Zn}_7\text{Sb}_2\text{O}_{12}$ are reported in the literature. The observed 'a' value is closer to that of $\text{Zn}_7\text{Sb}_2\text{O}_{12}$ phase. Direct evidence is also available from the analysis of the XPS chemical shift data. The antimony valency is different in the two spinel compounds namely pentavalent in $\text{Zn}_7\text{Sb}_2\text{O}_{12}$ phase and trivalent in ZnSb_2O_4 . The observed binding energy shift matches that of Sb^{5+} [83, 189, 190]. Since there is a shift observed in the Sb peak position above 900°C it is concluded that there is a reaction between the two constituent oxides to form a new spinel $\text{Zn}_7\text{Sb}_2\text{O}_{12}$ phase containing Sb^{5+} . Since there is a migration and diffusion of Sb^{5+} ions from the intergranular layer surrounding the ZnO grains due to formation of the spinel phase, the corresponding XPS peak intensity of Sb decreases with the increase in the sintering temperature. Inada [191, 192] has also observed the formation of a spinel phase at higher sintering temperatures.

As a consequence of the migration and the subsequent diffusion of Sb^{5+} ions from the intergranular layer, the α value also decreases with the increase in the temperature

Table 3.15 : Crystal phases observed by XRD
in ZS pellets sintered at various
temperatures.

Phase	T °C	PM	500	660	800	900	1000	1100	1200
	ZnO		VS	VS	VS	VS	VS	VS	VS
Spinel		A	A	A	A	W	M	S	M

Table 3.16 : Values of 'd' and 'a' for the
spinel phase in ZS pellets
sintered at various temperatures

hkl	T °C	d values ^o Å							
		PM	500	660	800	900	1000	1100	1200
220		A	A	A	A	3.02	3.02	3.01	3.01
400		A	A	A	A	2.14	2.14	2.14	2.14
511/333		A	A	A	A	1.65	1.65	1.65	1.66
440		A	A	A	A	1.52	1.52	1.52	1.52
a ^o Å		A	A	A	A	8.57	8.57	8.57	8.57

VS - very strong,
S - strong
M - medium
W - weak
A - absent

upto about 1000°C (table 3.9). No correlation could be found in the α value and the ratio of XPS peak intensities of samples sintered at different temperatures. These results are to some extent different from the analogous ZnO-Bi₂O₃ varistors [193]. In case of 4B system, the grain boundary concentration of Bi₂O₃ increases with temperature in the range 1000-1300°C and it decreases at higher temperatures (> 1400°C) due to the loss of the Bi₂O₃ by evaporation. On the other hand, in case of the 2S system, the grain boundary concentration of Sb₂O₃ is highest around 600-700°C and it decreases at higher temperatures > 800°C due to reaction with bulk ZnO leading to the formation of Zn₇Sb₂O₁₂ spinel phase.

Furthermore, in case of the 2B system, there was a direct correlation between the grain boundary concentration of Bi₂O₃ and the α value. Such a correlation is not seen in the 2S system. A possible explanation is as follows:

The value of α is controlled by the grain boundary layer as well as the density of the pellets. In case of 2B system the increase in the density by sintering as well as the increase in grain boundary concentration of Bi₂O₃ take place around 1000-1300°C, whereas in the case of 2S system, the density is increasing in this temperature range but the Sb₂O₃ concentration of the surface is decreasing, leading to two opposing influences on the α value.

3.3 ZnO + Bi₂O₃ + CoO (ZBC) VARISTOR SYSTEM

The non-linear exponent ' α ' obtained in the first two i.e. ZB and ZS systems is small. For the improvement of α -value, a third set of varistor samples has been prepared by the addition of CoO to the ZnO-Bi₂O₃ system. These ZBC varistor pellets sintered at various temperatures are studied in a similar way by XPS, SEM, EPMA and XRD techniques and the results are given below.

3.3.1 I-V characteristics

The current-voltage characteristics of the ZBC varistor pellets sintered at different temperatures are measured at room temperatures and the results are plotted in fig. 3.14. The I-V plots show much more non-linearity than for the first two systems. The ' α ' values calculated from the I-V plots using equation (2.2) are given in table 3.18. It is seen that the α -value increases slowly upto 800°C and then increases rapidly and attains a maximum value at 1300°C and then falls off rapidly. The maximum α value upto 25 is obtained at 1300°C, which rapidly decreases to 5 at 1400°C. These results agree with those got by others [29,42]. The non-linear exponent α has improved from 6.5 to 25 in this system by just adding cobalt oxide to the first system.

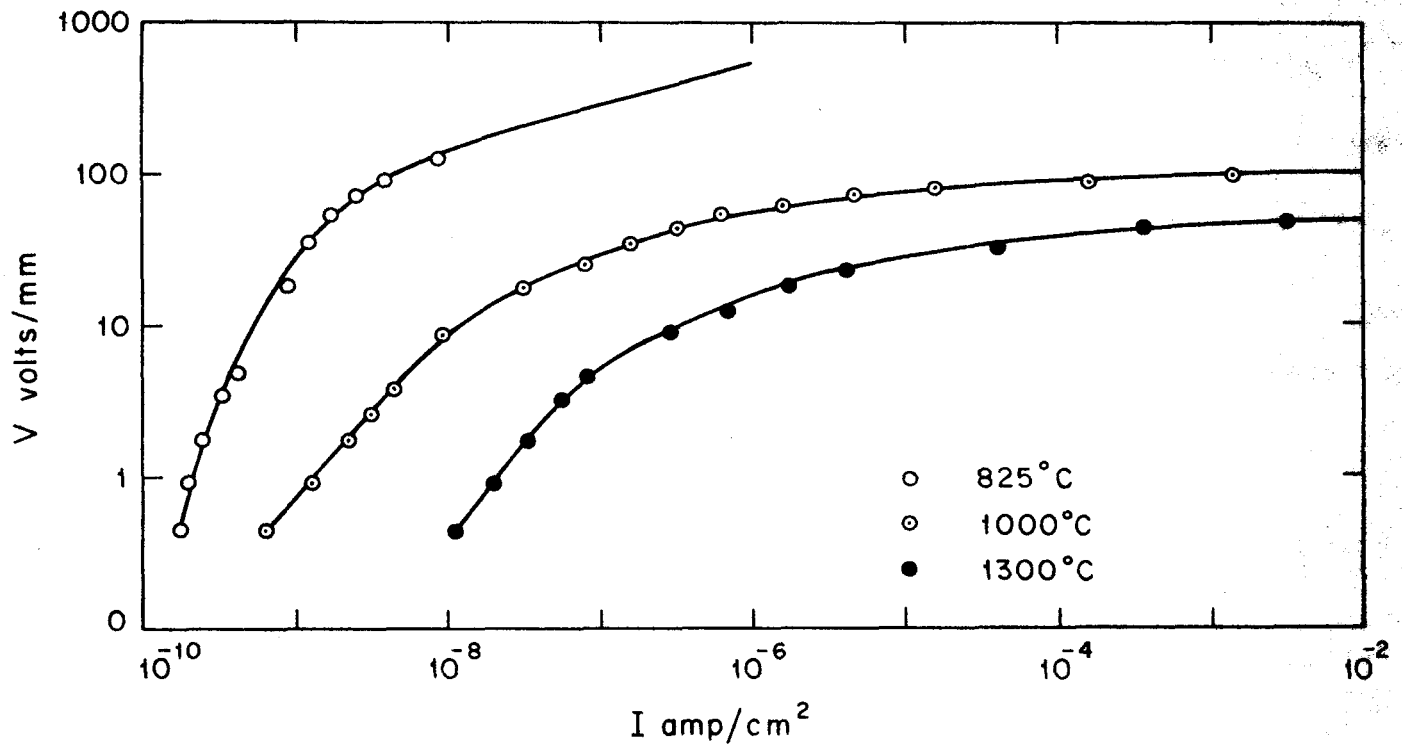
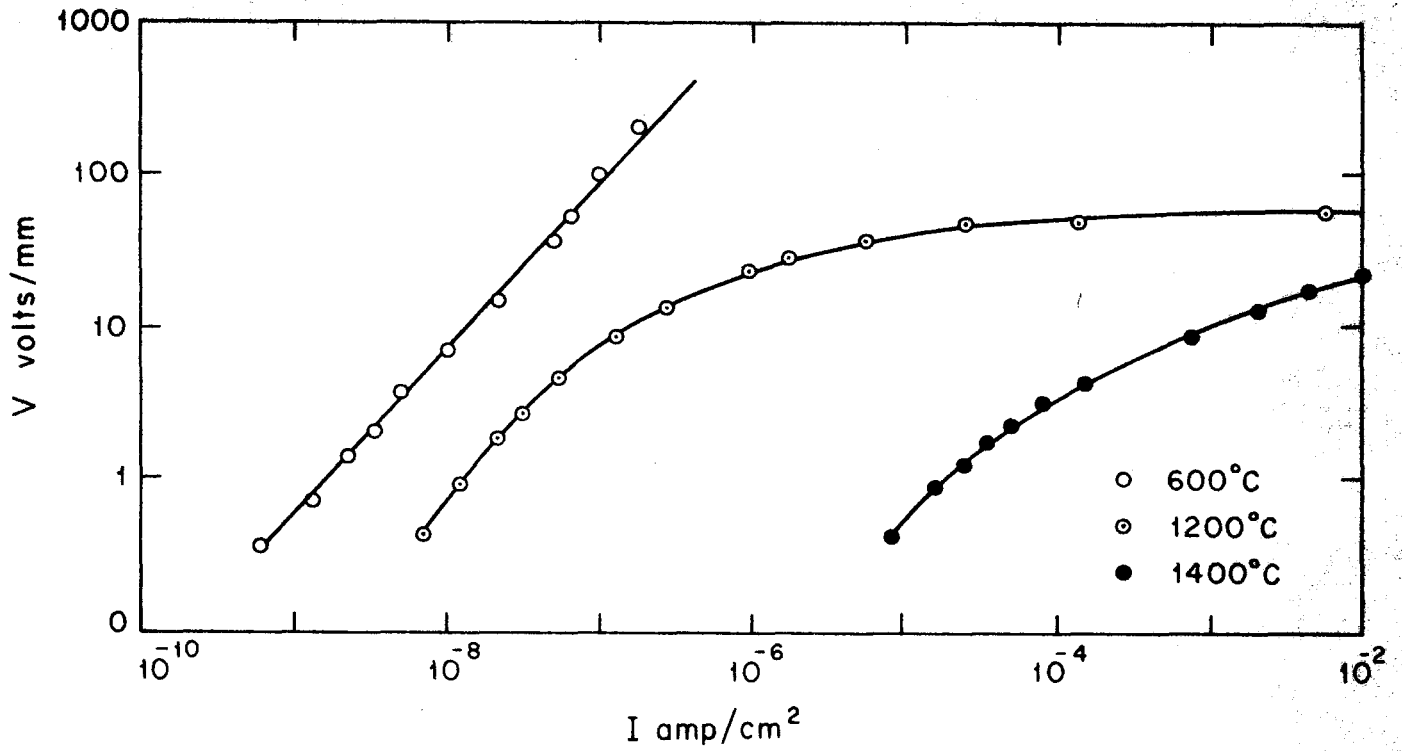


FIG. 3-14 : I-V CHARACTERISTICS OF (ZBC) PELLETS SINTERED AT VARIOUS TEMPERATURES .

Table 3.18 : Values of α , C and density of the ZBC pellets sintered at various temperatures

Sintering temperature $^{\circ}\text{C}$	Non-linear exponent ' α '	Non-linear constant 'C' (V/mm at 1 mA)	Pellet density (g/cm^3)
600	1.0	4×10^6 *	3.08
825	2.5	4×10^3 *	5.16
1000	20.0	96	5.17
1200	22.5	59	5.18
1300	25.0	48	5.19
1400	5.0	10	4.8

* extrapolated value.

The values of constant 'C' calculated from the I-V plots for various sintering temperatures are also given in table 3.18. It is seen that the 'C' value decreases as the sintering temperature increases. At low sintering temperatures upto 800°C the 'C' value is very high and then it decreases rapidly above 1000°C.

The density of these sintered pellets is also measured and given in the same table (3.18). The density remains constant upto 600°C and then it rapidly increases at 825°C and remains constant at that value upto 1300°C and decreases at 1400°C. By comparing these densities with those obtained for the ZB pellets under the similar conditions it is found they are higher, for example at 825°C the ZB pellets attain 57.8 % of the theoretical density whereas those of ZBC system attain 90.3 %. It is therefore concluded that cobalt oxide helps in sintering and the liquid phase sintering starts at a lower temperature.

3.3.2 Electron spectroscopic study

In order to find out whether cobalt oxide added in this system also segregates at the grain boundary like bismuth oxide, the ZBC pellets sintered at various temperatures are studied by the X-ray photoelectron spectroscopy and the spectra are given in fig. 3.16. The intensities for all the XPS peaks were measured and are given in table 3.19. The Zn/Bi intensity ratios are given in table 3.20 and the

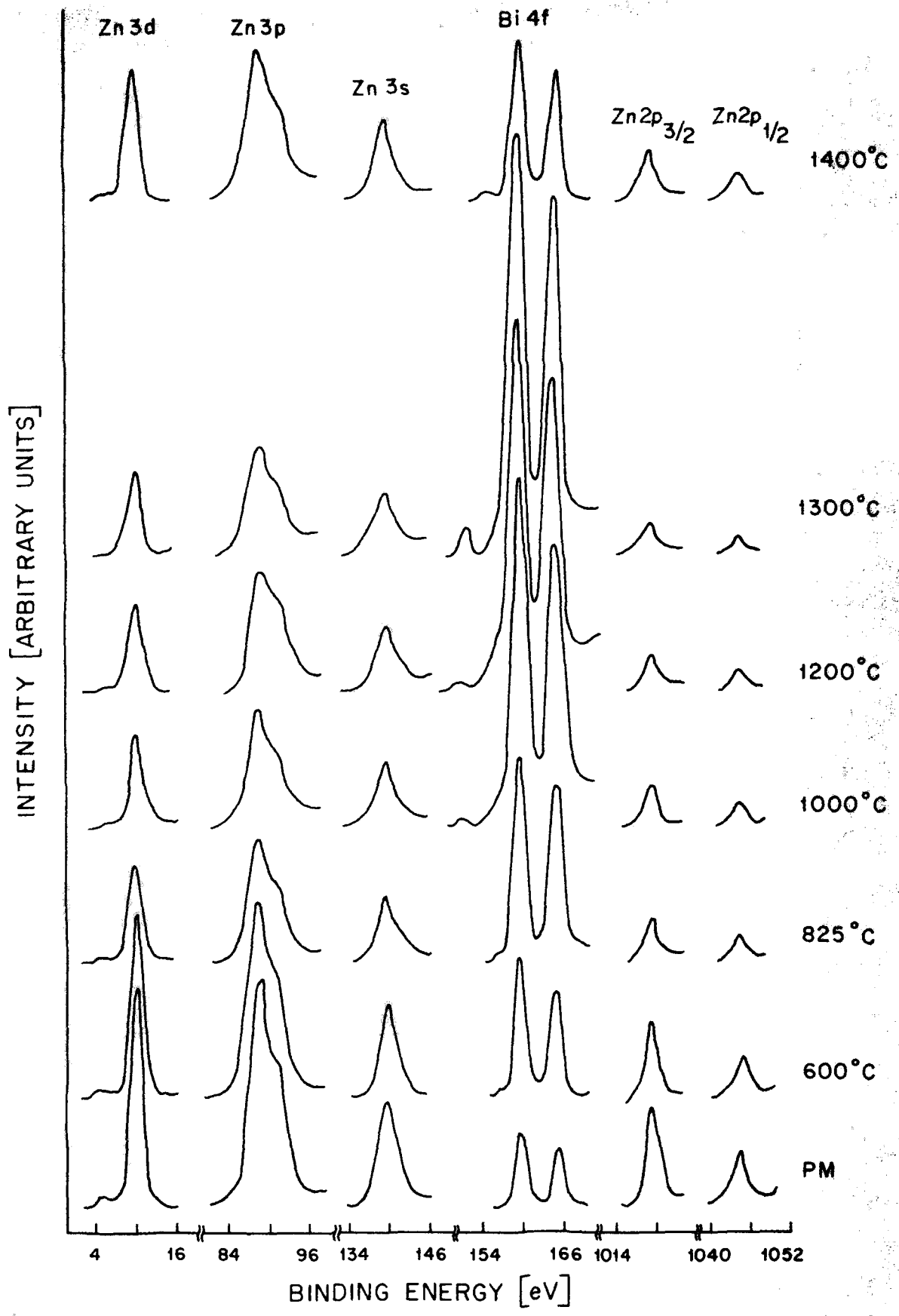


FIG. 3-15 : XPE - SPECTRA FOR (ZBC) PELLETS SINTERED AT VARIOUS TEMPERATURES.

Table 3.19 : XPS peak intensities from the Δ BC pellets
sintered at various temperatures (10^4 cps)

Sinter- ing tempe- rature $^{\circ}$ C	Zn-3d	Zn-3p	Zn-3s	Zn-2p _{3/2}	Zn-2p _{1/2}	Zn-Auger LII M ₂ M ₁ V	Zn-Auger LIII M ₂ M ₁ V	Bi-4f _{7/2}	Bi-4f _{5/2}
PM	8.0	8.4	3.8	36.0	18.0	9.0	20.7	2.6	2.0
600	6.8	7.2	3.3	28.0	14.0	8.2	18.9	5.1	3.9
825	3.6	4.5	2.4	15.0	7.5	5.6	12.8	7.5	6.5
1000	3.3	4.3	2.3	14.0	7.0	4.7	11.6	12.8	10.3
1200	3.2	4.2	2.2 ₅	12.0	6.0	4.6	11.1	13.6	11.4
1300	3.0	4.0	2.2	11.0	5.5	4.4	10.5	15.4	13.4
1400	4.8	5.5	2.8	13.0	9.0	7.5	17.1	5.7	4.6

Table 3.20 : XPS peak intensity ratios for the ZBC pellets sintered at various temperatures

Sintering temperature °C	Zn-3d	Zn-3p	Zn-3s	Zn-2p _{3/2}	Zn-2p _{1/2}	Zn-Auger L _{II} M _V M _V	Zn-Auger L _{III} M _V M _V
	Bi-4f _{7/2}	Bi-4f _{7/2}	Bi-4f _{7/2}	Bi-4f _{7/2}	Bi-4f _{7/2}	Bi-4f _{7/2}	Bi-4f _{7/2}
PM	3.08	3.23	1.46	13.85	6.92	3.46	7.96
600	1.33	1.41	0.65	5.49	2.75	1.61	3.71
825	0.48	0.60	0.32	2.00	1.00	0.75	1.71
1000	0.26	0.34	0.18	1.09	0.55	0.37	0.91
1200	0.24	0.31	0.16	0.88	0.44	0.34	0.82
1300	0.19	0.26	0.14	0.71	0.36	0.29	0.68
1400	0.84	0.96	0.49	3.16	1.58	1.31	3.00

PM - Physical mixture before sintering.

variation of these Zn/Bi intensity ratios as a function of sintering temperatures are shown by plotting Zn/Bi versus sintering temperatures in fig. 3.16.

It is clearly seen from the XPS spectra and intensity table that the intensity of Bi peaks increases as the sintering temperature increases, whereas the Zn peak intensity decreases simultaneously. It is therefore concluded that, similar to ZB system, bismuth starts migrating to the intergranular layer between the zinc oxide grains at 600°C. This migration becomes progressively more pronounced at higher sintering temperatures as is clearly seen from the decrease in the intensity ratios of Zn/Bi peaks (table 3.20 and fig. 3.16). This intensity ratio is minimum at 1300°C similar to the ZB system, the Bi intensity becoming maximum whereas Zn peak intensity becoming minimum which means that the migration of bismuth oxide to zinc oxide grain surface is maximum at 1300°C.

However, unlike Bi_2O_3 , cobalt peak is not detected at all therefore it is easily concluded that cobalt oxide is not migrating on the surface of zinc oxide grains, but it is dissolving, during liquid sintering, into the zinc oxide phase.

When pellets of ZBC varistor system are sintered at 1400°C, the intensity of Bi peaks suddenly decreases (simultaneously Zn peak intensity increases). It is reasonable to

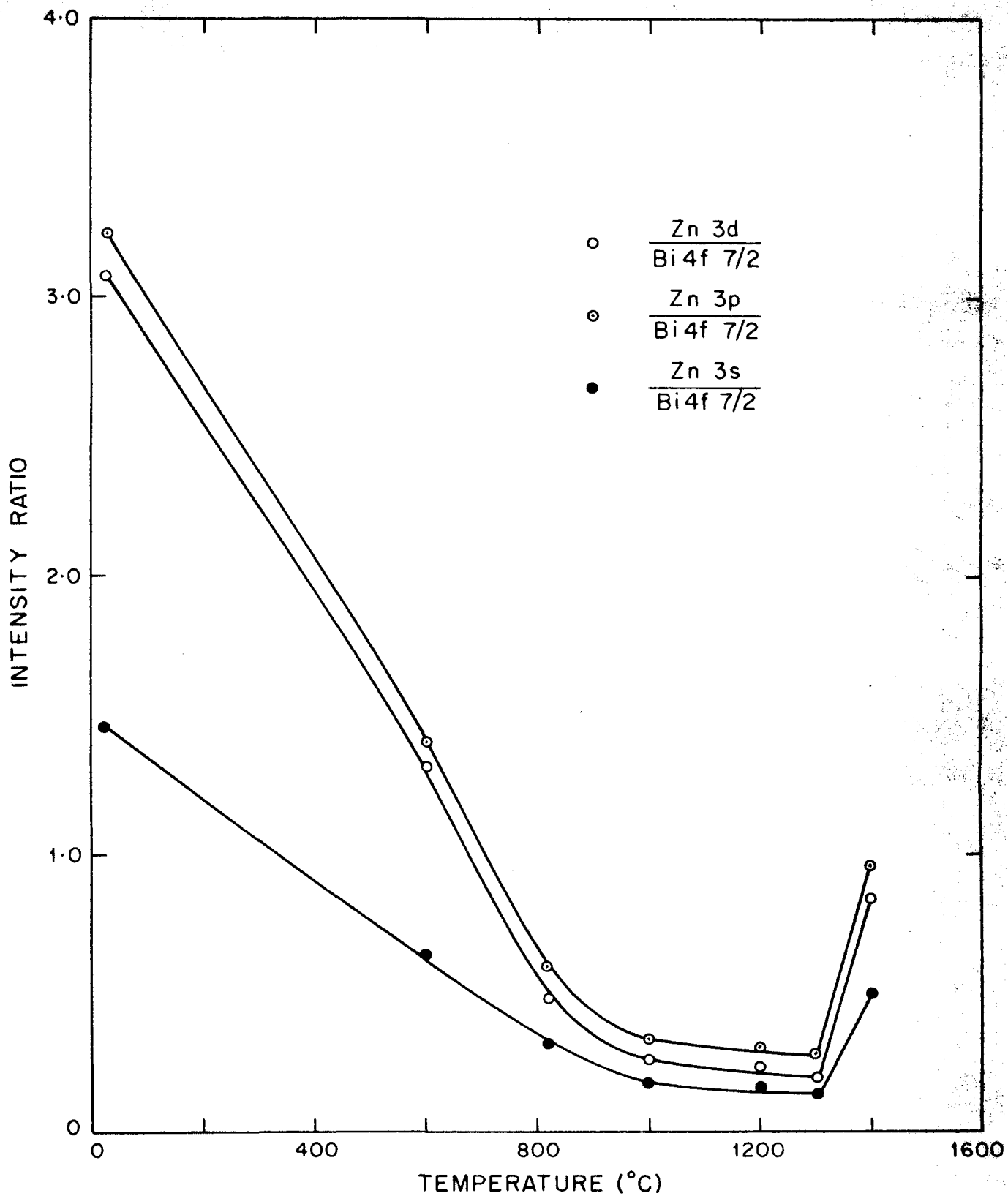


FIG. 3-16 : Zn/Bi XPS PEAK INTENSITY RATIO AS A FUNCTION OF SINTERING TEMPERATURE OF (ZBC) PELLETS.

explain this sudden increase in the intensity ratio (Zn/Bi) on the basis of the loss in Bi_2O_3 due to its evaporation from the surface.

The binding energies calculated from the XPS peak positions for Zn and Bi electrons are given in table 3.21. There is no change in the XPS binding energy of Zn and Bi electrons, similarly no kinetic energy change in Zn Auger electrons is observed. It is thereby confirmed that no valency change of zinc or bismuth has taken place after sintering.

3.3.3 Scanning electron microscopy and electron probe micro analysis

To understand the role of cobalt oxide which improves the α value nearly four times over that of the ZB system, the microstructure of these ZBC varistor pellets sintered at different temperatures is examined by SEM. The distribution of Bi_2O_3 and CoO in these pellets are also studied by EPMA. The scanning electron micrograph (X2000 magnification) of a ZBC pellet sintered at 1300°C is shown in fig. 3.17. The micrograph clearly shows that the larger grains are clearly separated by thin layers of a different phase.

Table 3.21 : XPS binding energy and XAE kinetic energy of the ZBC pellets sintered at various temperatures

Sintering temperature °C	XPS binding energy (eV)						XAE kinetic energy (eV)		
	Zn-3d	Zn-3p	Zn-3s	Zn-2p _{3/2}	Zn-2p _{1/2}	Bi-4f _{7/2}	Bi-4f _{5/2}	Zn-Auger L _{II} M _{IV} M _V	Zn-Auger L _{III} M _V M _V
PM	10.2	88.8	139.6	1021.4	1044.6	159.8	165.0	1012.1	988.9
600	10.2	88.9	139.6	1021.3	1044.5	159.7	164.9	1012.0	988.8
825	10.3	88.9	139.7	1021.4	1044.6	159.8	165.0	1012.1	983.9
1000	10.2	88.7	139.7	1021.4	1044.6	159.8	165.0	1012.0	988.8
1200	10.4	90.0	139.8	1021.6	1044.8	159.9	165.1	1012.0	988.7
1300	10.3	88.9	139.7	1021.5	1044.7	159.8	165.0	1012.0	988.7
1400	10.2	88.8	139.6	1021.4	1044.6	159.8	165.0	1012.1	988.9

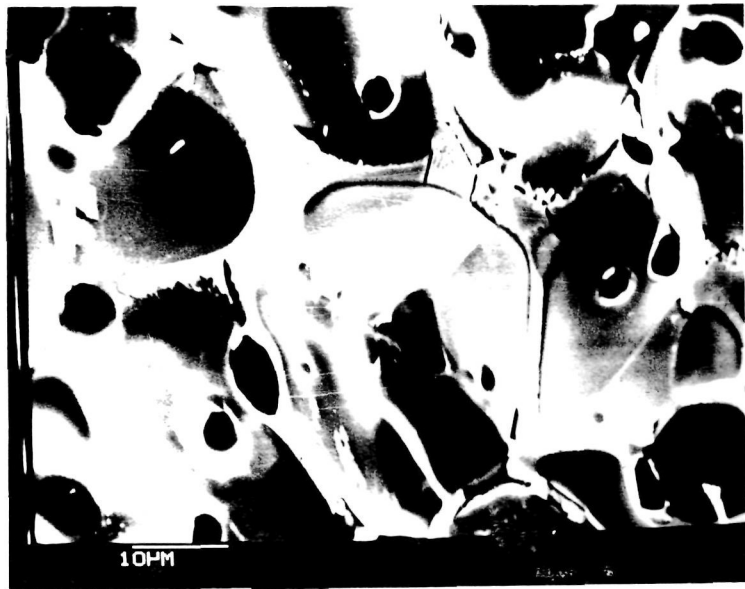


Fig. 3.17 : Scanning electron micrograph of a ZBC pellet sintered at 1300°C .

The electron probe microanalysis was carried out first by putting an electron probe on a larger grain and then on an intergranular layer. The characteristic X-ray spectra obtained are given in fig. 3.18. The X-ray integrals for Zn, Bi and Co were obtained from the characteristic X-ray spectrum which are given in table 3.22.

It is clearly seen from the Zn and Bi integrals that the big grain is ZnO and the intergranular phase is rich in Bi_2O_3 . Similarly from the micrograph (fig. 3.17) it is seen that the migration of Bi_2O_3 at grain boundary seems to be much clearer than that in the ZB pellets sintered at the same temperature (fig. 3.6). In the ZB pellet micrograph (fig. 3.6), small grains of Bi_2O_3 are distributed all over the place, whereas such grains are not seen in the micrograph of ZBC pellets (fig. 3.17). This means that the cobalt oxide helps in the formation of Bi_2O_3 intergranular layer. This may therefore be one of the reasons for the improvement in the non-linear exponent value on adding cobalt oxide.

The CoO may be dissolving in the ZnO during the liquid phase sintering. This dissolution of CoO may be changing the resistivity of ZnO grains and that may be one of the reasons for the improvement in the α -value.

For a more detailed analysis of the migration of Bi_2O_3 and also to know whether CoO is migrating on surface

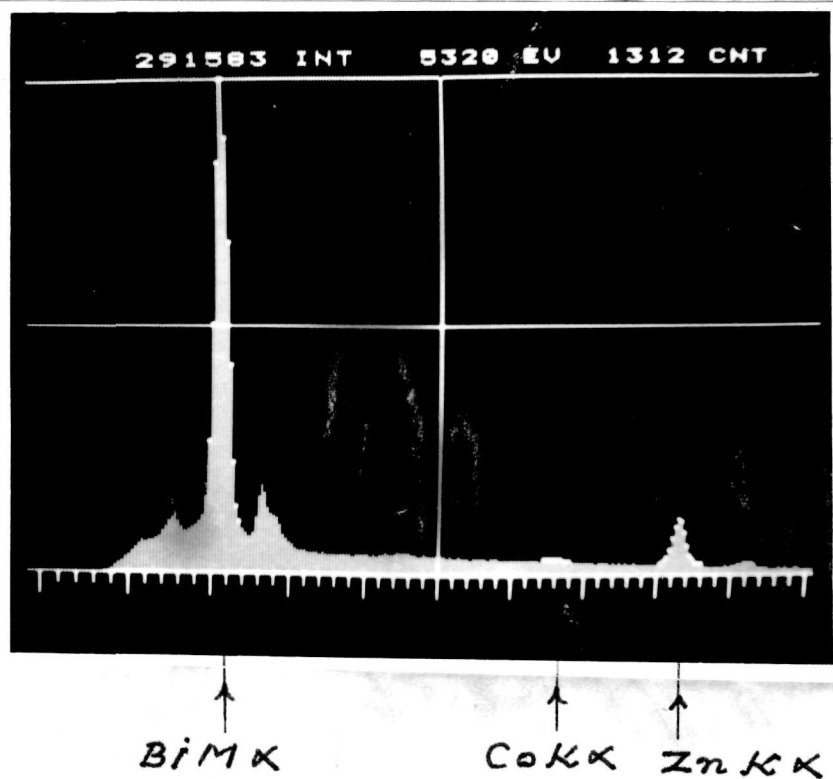


Fig. 3.18 : Energy dispersive analysis of X-rays (EDAX) of a ZBC pellet sintered at 1300°C, electron probe on-(a) total area covered in micrograph fig. 3.17 (b) big grain (c) intergranular layer.

Table 3.22 : EPMA results at various places
of a ZBC pellet sintered at 1300°C

Place of analysis	Integral			Integral ratio	
	ZnK _α	BiM _α	CoK _α	$\frac{\text{ZnK}_{\alpha}}{\text{BiM}_{\alpha}}$	$\frac{\text{ZnK}_{\alpha}}{\text{CoK}_{\alpha}}$
Total surface covered in fig.3.17	2,71,558	97,443	3,979	2.79	68.25
Probe on a big grain	2,41,992	11,368	3,481	21.29	69.52
Probe on an intergranular layer	1,21,168	3,12,120	448	0.388	270.46

at different sintering temperatures other than 1300°C, ZBC pellets sintered at various temperatures were studied by SEM and EPMA techniques. The scanning electron micrographs of the ZBC pellets sintered at different temperatures are shown in fig. 3.19. It is clearly seen from the micrographs that as the sintering temperature increases the grain size increases (the measured values of the average grain size at different sintering temperatures are given in table 3.23). The ZnO grain size slowly increases upto 1000°C and becomes maximum in the temperature range from 1200-1400°C. The intergranular layer formation is found to start from 1000°C and its thickness is maximum at 1300°C, where the maximum α -value is obtained.

The SEM micrograph of ZBC pellet sintered at 1400°C fig. 3.19(e) shows a sudden decrease in the thickness of the intergranular layer obviously due to the evaporation of Bi_2O_3 at higher temperatures ($> 1400^\circ\text{C}$). At this sintering temperature the α value is also reduced from 25 to 5. The characteristic X-ray integrals ZnK_α , BiM_α and CoK_α for ZBC pellets sintered at different temperatures and their ratios are given in table 3.23. It is clearly seen that as the sintering temperature increases, the integral of BiM_α increases (i.e. migration of Bi_2O_3 on surface increases). CoK_α X-ray integrals are however not changing much except at 1400°C. The ratio of Zn/Bi integrals is

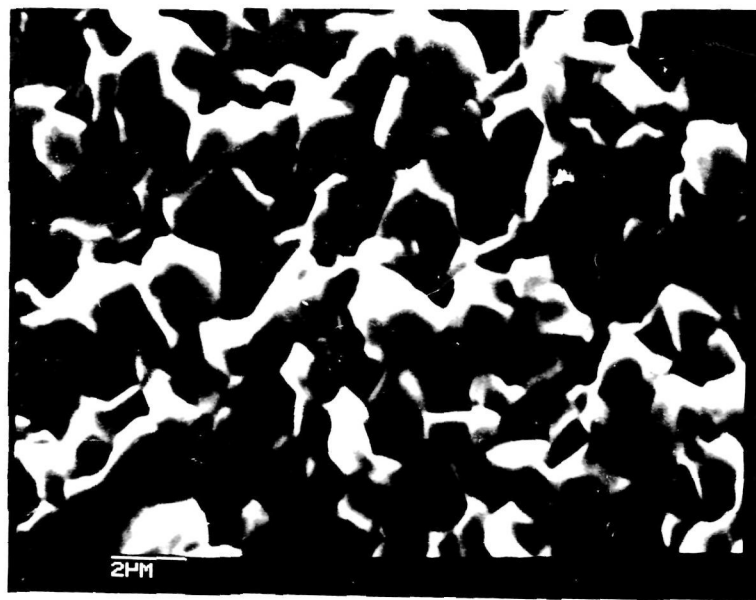
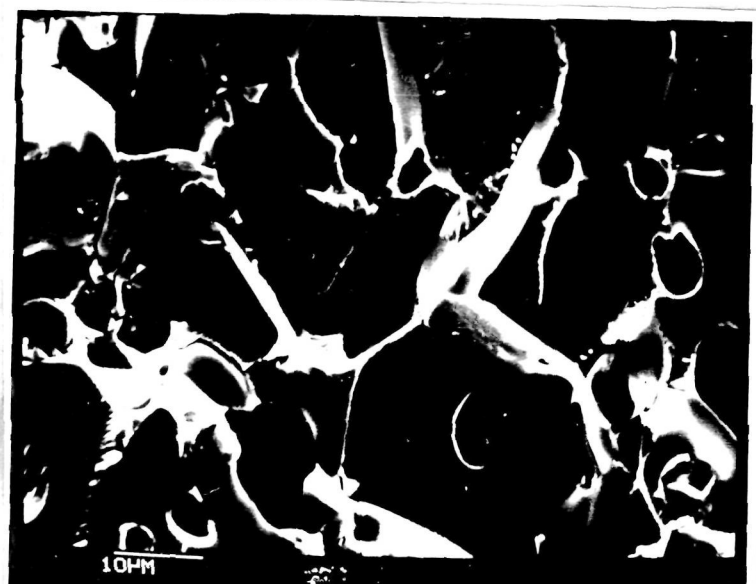


Fig. 3.19
(a)



(b)



(c)



(d)



(e)

Fig. 3.19 : Scanning electron micrographs for the ZBC pellets sintered at (a) 825°C (b) 1000°C (c) 1200°C (d) 1300°C (e) 1400°C .

Table 3.23 : XPM results and grain size of the ZBC pellets sintered at various temperatures

Sintering temperature °C	Integral			Integral ratio		Grain size (micron)
	ZnK α	BiM α	CoK α	Zn/Bi	Zn/Co	
PM	2,94,113	28,026	3,863	10.49	76.14	< 1
600	2,64,147	25,932	3,599	10.19	73.39	< 1
825	2,63,680	27,755	3,610	9.50	73.05	2-3
1000	2,62,302	33,344	3,629	7.87	72.28	4-5
1200	2,55,521	49,705	3,735	5.14	68.41	25-30
1300	2,50,847	90,247	3,737	2.78	67.13	25-30
1400	2,90,179	5,491	4,835	52.85	60.02	25-30

PM - Physical mixture before sintering

minimum at 1300°C where the α -value is also maximum. The Zn/Bi integral ratio increases suddenly at 1400°C due to evaporation of Bi_2O_3 from the ZnO grains and therefore more ZnO grain surfaces are exposed and more cobalt X-ray integrals are counted from the ZnO grains.

3.3.4 X-ray diffraction study

The 'd' values were calculated from the X-ray diffraction pattern taken for the ZBC pellets sintered at various temperatures and the results are presented in table 3.24. These data have been compared with the standard X-ray pattern to identify the various phases present. The analysis is presented in a tabular form in table 3.25. The two phases ZnO and $\gamma\text{-Bi}_2\text{O}_3$ are identified and their 'd' values are given in tables 3.26 and 3.27 respectively.

The most important feature about the addition of CoO is its efficiency in stabilizing the cubic Bi_2O_3 . It can be seen that the Bi_2O_3 converts to the cubic form even at 600°C much below the melting point. Also the proportion of the cubic phase is much more enhanced. In the ZB system, the maximum amount of the cubic phase got was 0.5 %, whereas with the help of CoO, one can get the entire amount of added Bi_2O_3 (1 %) in the cubic phase. This is also clearly seen from the electron micrograph (fig. 3.17), where CoO helps

Table 3.24 : XRD results of the ZBC pellets sintered at various temperatures

PM	600°C		825°C		1000°C		1200°C		1300°C		1400°C	
	d Å	I/I ₁	d Å	I/I ₁	d Å	I/I ₁	d Å	I/I ₁	d Å	I/I ₁	d Å	I/I ₁
3.67	2.2	3.54	1.1	3.56	1.8	-	-	-	-	-	-	-
3.23	1.5	3.17	7.8	3.18	9.0	3.21	2.8	3.21	3.2	3.22	2.5	-
2.93	5.8	2.91	2.2	2.91	1.8	-	-	-	-	-	-	-
2.79	66.6	2.78	66.6	2.79	62.4	2.79	61.3	2.79	61.9	2.79	71.0	2.80
2.71	2.9	2.69	5.6	2.70	6.3	2.67	1.6	2.66	2.0	2.67	0.9	-
2.67	1.5	-	-	-	-	-	-	-	-	-	-	-
2.58	33.3	2.57	33.3	2.58	29.2	2.58	35.9	2.58	33.3	2.58	21.4	2.59
2.46	100	2.46	100	2.46	100	2.46	100	2.46	100	2.46	100	2.47
2.12	1.8	-	-	-	-	-	-	-	-	-	-	-
1.90	18.8	1.89	21.1	1.90	18.0	1.90	18.9	1.90	29.8	1.90	16.0	1.91
1.75	1.1	1.74	2.2	1.74	2.2	1.73	0.9	1.73	1.0	1.73	1.0	-
-	-	1.64	2.2	1.64	1.4	1.64	1.4	1.64	1.0	1.64	0.5	-
1.62	37.3	1.61	40.0	1.62	37.3	1.62	30.5	1.62	34.1	1.62	27.9	1.62
1.47	23.2	1.47	27.8	1.47	20.7	1.47	18.9	1.47	15.9	1.47	14.3	1.47

Table 3.2b : The crystal phases observed by XRD in ZBC pellets sintered at various temperatures.

Phases T ^o C	ZnO	α -Bi ₂ O ₃	γ -Bi ₂ O ₃
PM	VS	S	A
600	VS	A	S
825	VS	A	S
1000	VS	A	M
1200	VS	A	W
1300	VS	A	W
1400	VS	A	VVW

- PM - Physical mixture before sintering
- VS - very strong
- S - strong
- M - medium
- W - weak
- VVW - very very weak
- A - absent

Table 3.26 : Values of 'd', 'a' and 'c' for the ZnO crystal phase in ZBC pellets sintered at various temperatures.

hkl	T°C	d values Å						
		PM	600	825	1000	1200	1300	1400
100	2.794	2.777	2.791	2.791	2.791	2.791	2.794	2.803
022	2.583	2.569	2.577	2.583	2.583	2.583	2.583	2.590
101	2.456	2.456	2.457	2.457	2.457	2.457	2.460	2.465
102	1.901	1.894	1.901	1.901	1.901	1.901	1.901	1.905
110	1.619	1.614	1.616	1.618	1.617	1.617	1.620	1.622
103	1.473	1.468	1.470	1.472	1.471	1.471	1.473	1.474

a Å		3.24	3.23	3.24	3.24	3.24	3.24	3.25
c Å		5.20	5.19	5.20	5.20	5.20	5.21	5.21

PM - Physical mixture before sintering.

Table 3.27 : Values of 'd' and 'a' for the
Y-Bi₂O₃ crystal phase in ZBC
pellets sintered at various
temperatures

hkl	T °C	d values Å					
		PM	600	825	1000	1200	1300
310	-	3.173	3.178	3.213	3.213	3.222	-
400	-	2.691	2.696	2.673	2.665	2.673	-
611	-	1.735	1.735	1.729	1.735	1.735	-

a Å	-	10.75	10.75	10.76	10.76	10.77	-

in spreading the Bi_2O_3 in the form of an uniform layer around the ZnO grains.

Another interesting feature is the lower sintering temperature in this system, which becomes quite evident on comparing the densities obtained under similar conditions for the ZB and ZBC systems. This is also connected with the stabilizing effect of CoO on Bi_2O_3 cubic phase. A phase transformation in $\alpha\text{-Bi}_2\text{O}_3$ to $\gamma\text{-Bi}_2\text{O}_3$ which sets in due to the addition of CoO may have the same effect on sintering as a molten phase. During the phase transformation the structure opens out in the same way as in a liquid phase and thereby helps in the intergrain transport and thereby in the sintering forces. A lowering in the melting point of Bi_2O_3 due to the instability imparted by the addition of CoO may not also be ruled out. In that case the enhanced sintering at a lower temperature would simply result from the appearance of the molten phase at a lower temperature.

There was no spinel phase observed in the ZBC system. Although cobalt oxide can be expected to form a spinel phase $\text{Zn}^{2+}\text{Co}_2^{3+}\text{O}_4^{2-}$, but there is no experimental evidence to support this. This requires oxidation of Co^{2+} to Co^{3+} . It is therefore likely that there are no other phases (other than ZnO and $\gamma\text{-Bi}_2\text{O}_3$) in the sintered ZBC pellets. The cobalt is dissolved in the ZnO and Bi_2O_3 and in the latter case it plays the vital role in stabilizing the $\gamma\text{-Bi}_2\text{O}_3$ which is required for varistor property.

3.4 ZnO + Bi₂O₃ + Sb₂O₃ + CoO + MnO + Cr₂O₃ (ZBSCMCr)
VARISTOR SYSTEM

For the further improvement of α -value, a fourth set of varistor samples were prepared by addition of Sb₂O₃ + MnO + Cr₂O₃ to the previous (ZBC) system. These ZBSCMCr varistor pellets sintered at various temperatures are examined in the usual way by XPS, SEM, EPMA and XRD techniques and the results are given in the following paragraphs.

3.4.1 I-V characteristics

The I-V characteristics of the ZBSCMCr varistor pellets sintered at different temperatures and measured at room temperature are plotted in fig. 3.20. The non-linear behaviour is clearly seen from these I-V plots. The α -values calculated from these plots using equation (2.2) are given in table 3.28. It is seen that the α -value increases slowly upto 825°C and then more rapidly at 1000°C onwards. It attains the maximum value equal to 50 at 1300°C. By adding Sb₂O₃, MnO and Cr₂O₃ in the ZBC system, α -value has increased from 26 to 50 in this system.

The value of the constant 'C' (V/mm at 1 mA/cm²) calculated from the I-V plots are also given in table 3.28. It decreases as the sintering temperature increases similar to the previous systems. However, the 'C' value has increased

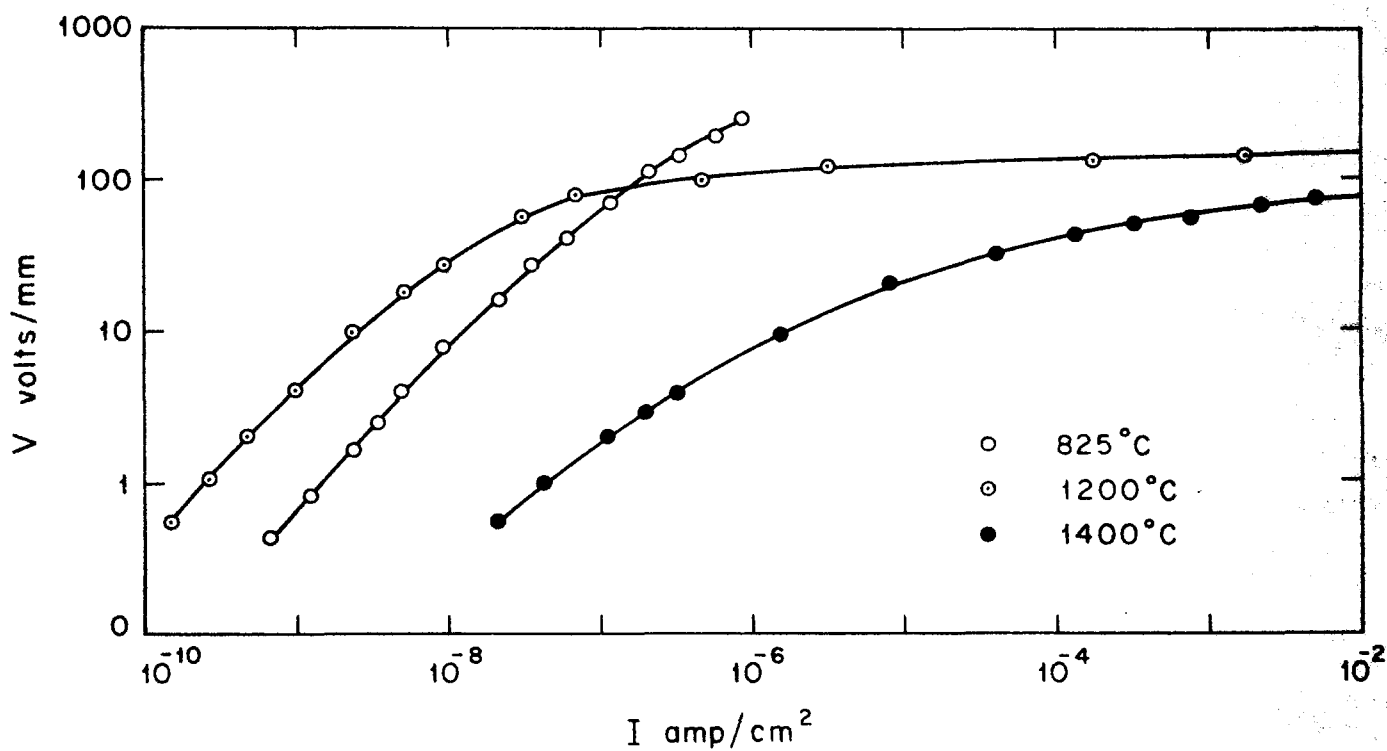
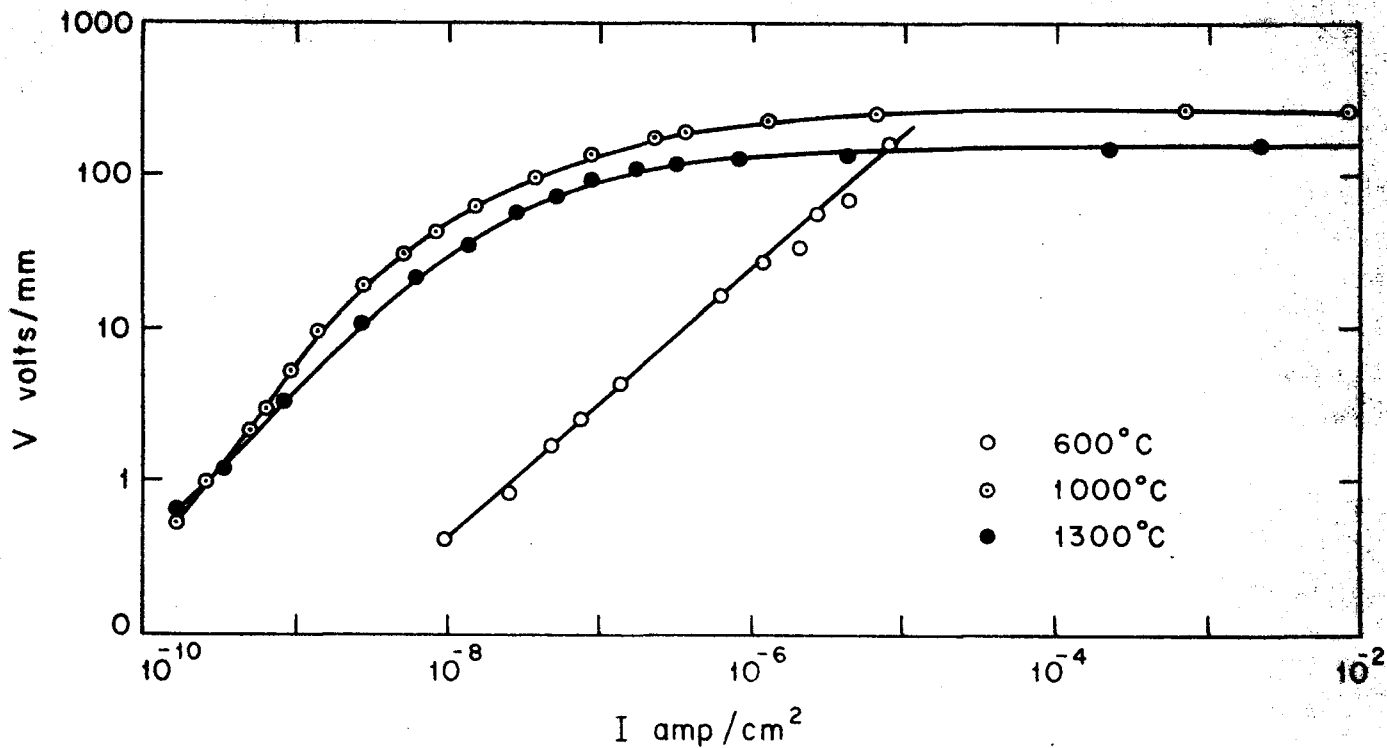


FIG. 3-20 : I-V CHARACTERISTICS OF (ZBSCMcr) PELLETS SINTERED AT VARIOUS TEMPERATURES.

Table 3.28 : Values of ' α ', ' C ' and density of the 4B5CMCr pellets sintered at various temperatures

Sintering temperature $^{\circ}\text{C}$	Non-linear exponent ' α '	Non-linear constant ' C ' (V/mm at 1 mA)	Pellet density (g/cm^3)
600	1.0	10^4 *	3.2
825	1.6	9×10^3 *	3.4
1000	45.0	240	5.2
1200	48.0	152	5.2
1300	50.0	135	5.3
1400	7.7	64	4.9

* extrapolated values.

by adding three more oxides in the ZBC system (for example at the sintering temperature of 1300°C, the C value is 135 V/mm in ZBSCMCr system as against 48 V/mm for the corresponding ZBC systems).

The density values calculated for ZBSCMCr pellets sintered at different temperatures are given in table 3.28. In this system also the density increases as the sintering temperature increases; it increases slowly upto 900°C and then rapidly beyond 1000°C and attains a maximum at 1300°C. The density at 1400°C reduces from 5.3 to 4.9 g/cm³ due to the loss of Bi₂O₃ by evaporation from the intergranular layer. In this system also it has been seen that the α -value depends on the density and it attains the maximum value at the highest density value. The α -value and density decrease at 1400°C.

3.4.2 Electron spectroscopic study

As seen from the last three systems, the X-ray photoelectron spectroscopy helped in understanding the migration of Bi₂O₃ and Sb₂O₃ on the surface of the ZnO grains; it was therefore decided to study this system also by this technique. The X-ray photoelectron spectra obtained from the pellets of this system sintered at various temperatures are given in fig. 3.21. The intensity of all the Zn peaks decreases

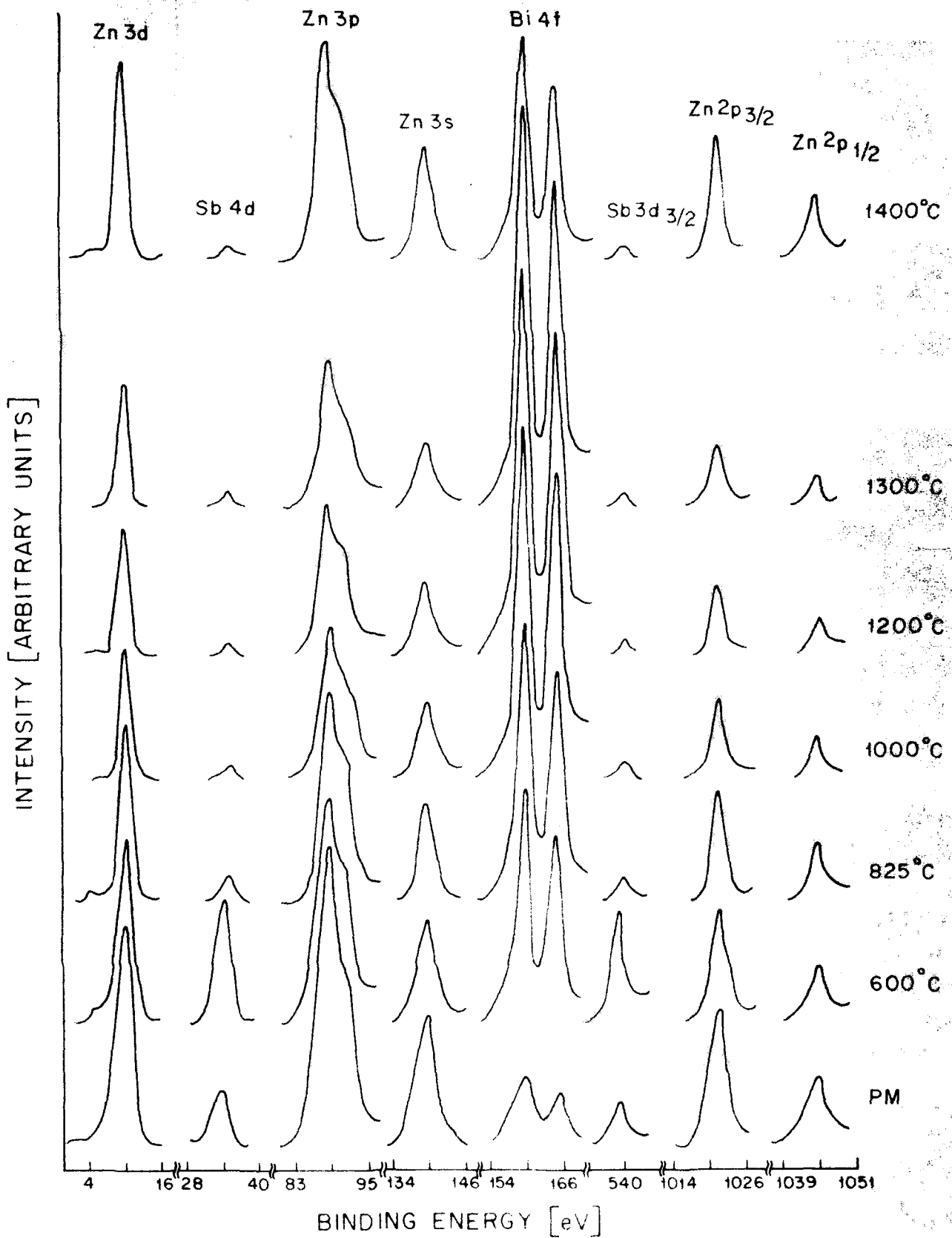


FIG. 3-21: XPE - SPECTRA FOR (ZBSCMCr) PELLETS SINTERED AT VARIOUS TEMPERATURES.

and that of Bi peaks increases as the sintering temperature increases upto 1300°C beyond which the trend is reversed. The intensity of Sb-4d and Sb-3d_{3/2} peaks increases and it is maximum at 660°C and again it starts decreasing as sintering temperature increases as observed in the ZS system [194]. The peaks of other oxides i.e. those of cobalt, manganese and chromium are not detectable even at the maximum sensitivity, therefore it is concluded that these oxides are not migrating on the surface, like bismuth and antimony oxides. This technique only detects top surface layers of 15-20 Å thickness. However, these oxides are detected by EPMA technique (results are discussed in the next pages) which can detect upto 1 to 2 micron depth.

The actual measured intensities for Zn, Bi and Sb XPS peaks are given in table 3.29, and their intensity ratios are given in table 3.30. The variation of Zn/Bi XPS peak intensity ratio as a function of sintering temperature is shown in the fig. 3.22. From these results it is clearly seen that the Zn/Bi intensity ratio is minimum at 1300°C, that means, the migration of Bi₂O₃ at the intergranular layer is again maximum like the previous ZB and ZBC pellets, and α-value is maximum at this temperature.

From the intensity of Sb XPS peaks it can be concluded that Sb migrates on the surface upto 660°C and at higher temperatures it diffuses into the ZnO grains. Furthermore

Table 3.29 : XPS peak intensities from the ZBSCMR pellets sintered at different temperatures (10^4 cps)

Sintering temperature $^{\circ}\text{C}$	Zn-3d	Zn-3p	Zn-3s	Zn-2p _{3/2}	Zn-2p _{1/2}	Zn-Auger L ₁₁₁ M ₂₂ V ₄₄	Zn-Auger L ₁₁₁ M ₂₂ V ₄₄	B1-4f _{7/2}	B1-4f _{5/2}	Sb-4d	Sb-3d _{3/2}
PM	9.0	12.2	5.3	55.0	27.5	14.1	28.8	2.8	2.2	2.2	5.1
600	7.6	9.0	4.2	46.0	23.0	10.8	24.0	9.5	8.0	5.0	13.5
825	7.2	8.7	3.9	44.0	22.0	9.9	23.4	11.3	9.3	0.9	2.7
1000	5.2	6.1	3.0	30.0	15.0	7.2	18.0	14.3	12.1	0.5	1.5
1200	5.1	6.0	2.9	28.0	14.0	6.9	17.1	15.5	12.8	0.4	1.2
1300	4.8	5.8	2.7	24.0	12.0	6.3	15.9	16.1	13.2	0.4	1.2
1400	8.0	8.8	4.5	48.0	24.0	11.1	24.3	8.8	7.1	0.4	1.2

Table 3.30 : APS peak intensity ratios for the ZBSCMCr pellets sintered at various temperatures

Sintering temperature °C	$\frac{\text{Zn-3d}}{\text{Bi-4f}} \frac{7}{2}$	$\frac{\text{Zn-3p}}{\text{Bi-4f}} \frac{7}{2}$	$\frac{\text{Zn-3s}}{\text{Bi-4f}} \frac{7}{2}$	$\frac{\text{Zn-2p}_{3/2}}{\text{Bi-4f}} \frac{7}{2}$	$\frac{\text{Zn-2p}_{1/2}}{\text{Bi-4f}} \frac{7}{2}$	$\frac{\text{Zn-Auger}}{\text{Li-MV}} \frac{7}{2}$	$\frac{\text{Zn-Auger}}{\text{Li-MV}} \frac{7}{2}$
PM	3.21	4.36	1.89	19.64	9.82	5.04	10.29
600	0.80	0.95	0.44	4.84	2.42	1.14	2.53
825	0.64	0.77	0.35	3.89	1.95	0.88	2.07
1000	0.36	0.43	0.21	2.10	1.05	0.50	1.26
1200	0.33	0.39	0.19	1.81	0.90	0.45	1.10
1300	0.29	0.36	0.17	1.49	0.75	0.39	0.99
1400	0.91	1.00	0.51	5.45	2.73	1.26	2.76

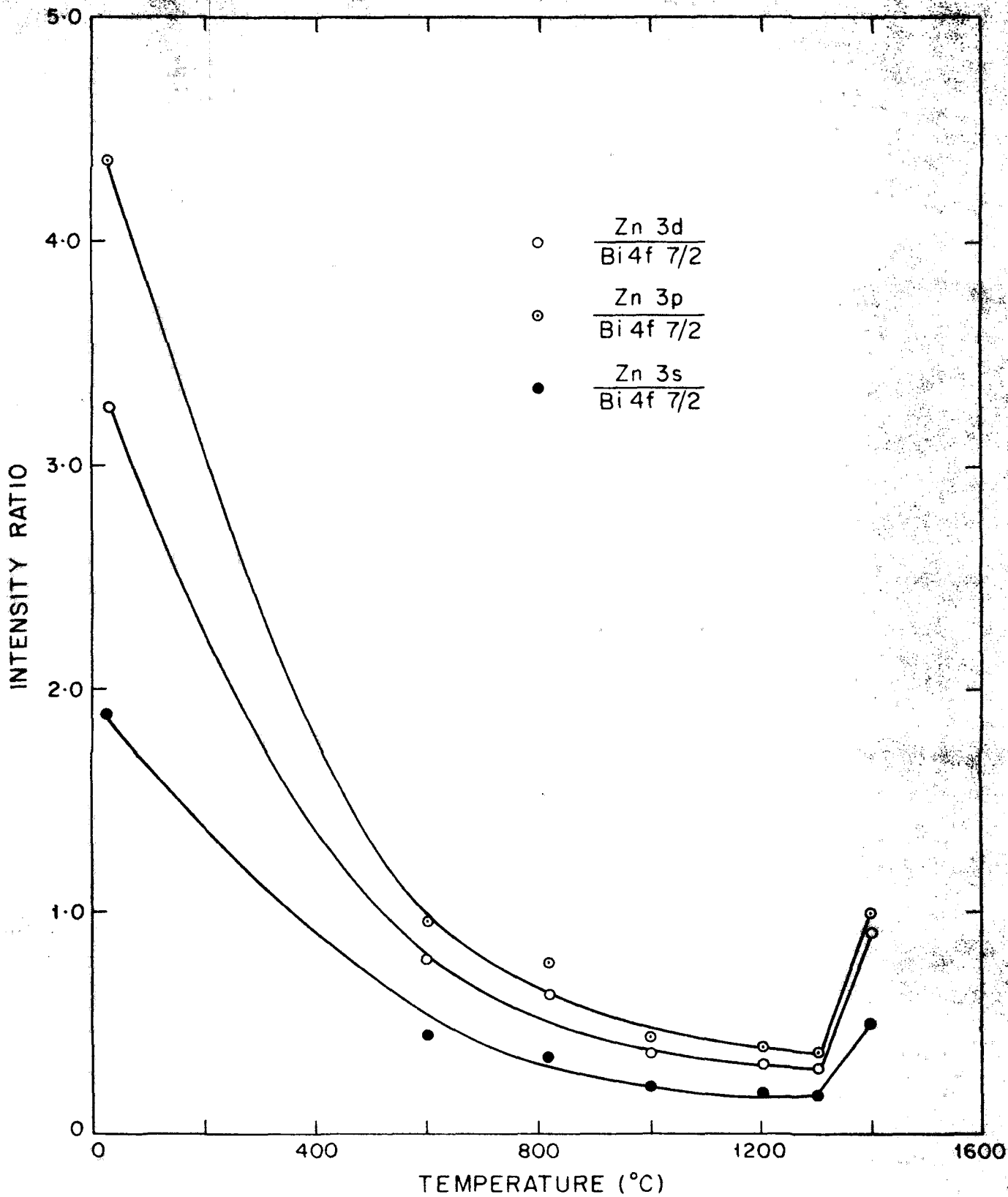


FIG. 3-22 : Zn/Bi XPS PEAK INTENSITY RATIO AS A FUNCTION OF SINTERING TEMPERATURE OF (ZBSCMcr) PELLETS.

from the binding energy shift, it may be concluded that antimony changes from Sb^{3+} to Sb^{5+} in this system also. The actual binding energies for Zn, Bi, Sb XPS peaks are given in table 3.31 and from the Sb binding energy shift it is concluded that the spinel type cubic phase having antimony in pentavalent state similar to the ZS system is formed in this system.

3.4.3 Scanning electron microscopy and electron probe microanalysis

To know the role of other oxides particularly of MnO and Cr_2O_3 added in this system to improve the α -value, the microstructure of ZBSCMO pellets was studied by SEM and distribution of these oxides is identified by the EPMA technique.

Fig. 3.23 shows the SEM micrograph of these pellets sintered at $1300^\circ C$, at which temperature the highest non-linearity is obtained. The micrograph clearly shows big grains of 10-15 microns in size, vein like structure between these grains (intergranular layer). In addition to these, small grains of size from 1 to 5 microns are also observed in this system. These small grains were absent in the previous systems.

This microstructure is characterized by the EPMA technique and the characteristic X-ray spectrum for the

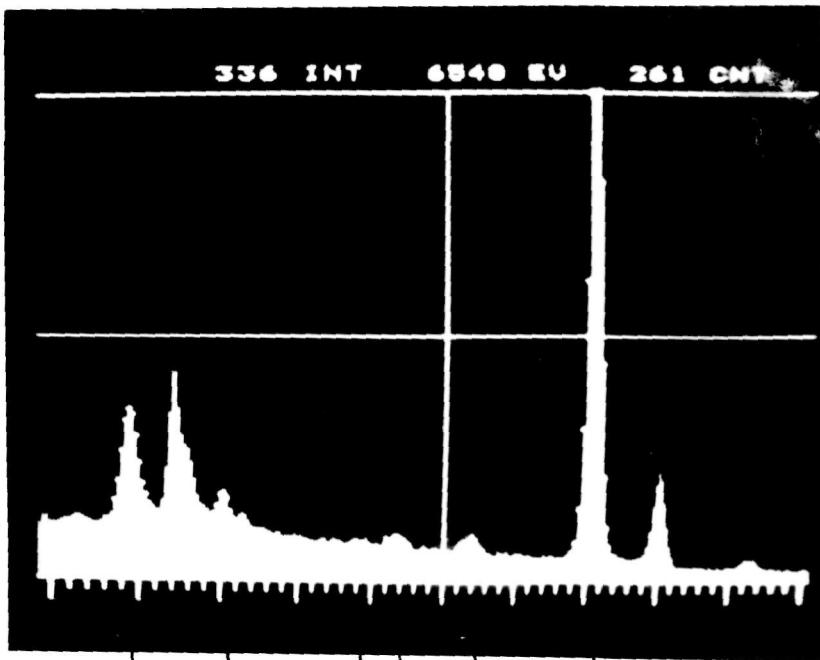
Table 3.31 : XPS binding energy and XAS kinetic energy of the ZBSCMCr pellets sintered at various temperatures.

Sintering temperature °C	XPS binding energy (eV)						XAS kinetic energy (eV)				
	Zn-3d	Zn-3p	Zn-3s	Zn-2p _{3/2}	Zn-2p _{1/2}	Bi-4f _{7/2}	Bi-4f _{5/2}	Sb-4d	Sb-3d _{3/2}	Zn-Auger L _{II} M _{IV} V	Zn-Auger L _{III} M _{IV} V
PM	10.2	88.8	139.6	1021.4	1044.6	159.8	165.0	34.2	539.2	1012.0	988.8
600	10.3	88.9	139.7	1021.5	1044.7	159.9	165.1	34.3	539.3	1011.9	988.7
825	10.2	88.8	139.6	1021.4	1044.6	159.8	165.0	34.3	539.3	1012.0	988.8
1000	10.2	88.8	139.6	1021.4	1044.6	159.8	165.0	35.0	540.0	1012.0	983.8
1200	10.4	89.0	139.8	1021.6	1044.8	160.0	165.2	35.0	540.0	1011.8	988.6
1300	10.3	88.9	139.7	1021.5	1044.7	159.9	165.1	35.0	540.0	1011.9	988.7
1400	10.2	88.8	139.6	1021.4	1044.6	159.8	165.0	35.0	540.0	1012.0	988.8



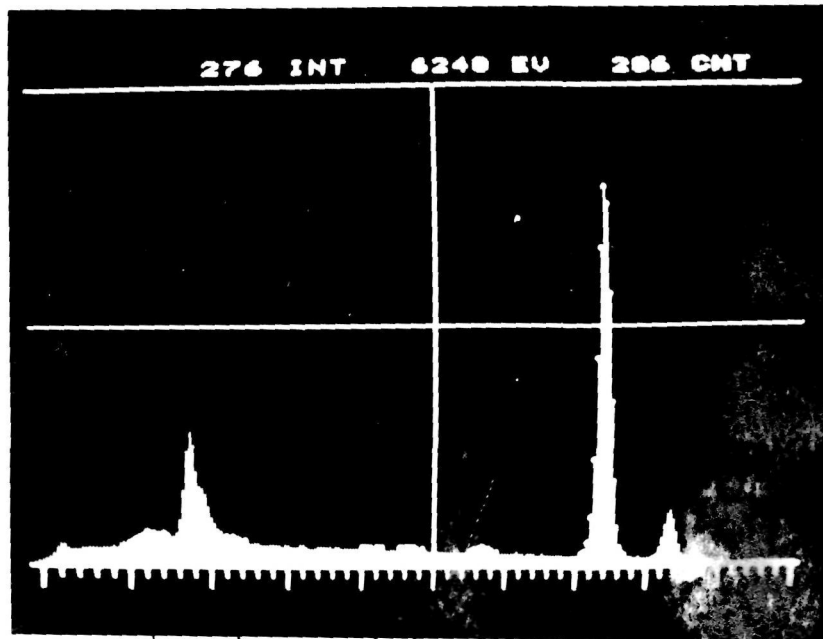
Fig. 3.23 : Scanning electron micrograph of a
(ZBSCMCr) pellet sintered at 1300°C.

total area covered in fig. 3.23 is shown in fig. 3.24(a). The characteristic X-ray spectra obtained when the probe is moved to big grain, small grain or to an intergranular layer are given in figs. 3.24(b), (c) and (d) respectively. The spectrum (fig. 3.24(a)) for the total surface shows peaks for BiM_α at 2.418 KeV, SbL_α at 3.604 KeV, CrK_α at 5.411 KeV, MnK_α at 5.894 KeV, CoK_α at 6.924 KeV and ZnK_α at 8.63 KeV. When the electron probe is placed on the big grain, the X-ray spectrum shown in fig. 3.24(b) is obtained which clearly shows a strong Zn peak and small peaks of Co, Mn. When the electron probe is moved to the smaller grains, the X-ray spectrum (fig. 3.24(c)) obtained shows clearly the Zn, Mn, Co, Cr and enhanced Sb peaks. When the electron probe is moved to an intergranular layer, the X-ray spectrum fig. 3.24(d) clearly shows enhancement of the Bi peak intensity together with small peaks of Zn, Cr and Sb. The X-ray integrals under each peak obtained by setting the energy windows (for BiM_α from 2.28 to 2.70 KeV, for SbL_α from 3.48 to 3.74 KeV, for CrK_α from 5.26 to 5.52 KeV, for MnK_α from 5.80 to 6.08 KeV, for CoK_α from 6.76 to 7.14 KeV and for ZnK_α from 8.34 to 8.96 KeV) are given in table 3.32. From these X-ray integrals at various points it is clearly seen that the big grains contain predominantly zinc oxide with some other oxides of Co, Mn and very small amount of Bi. The smaller grains also consist mainly of zinc oxide but with larger amounts of Sb, Co, Mn and Cr and small amount of Bi.



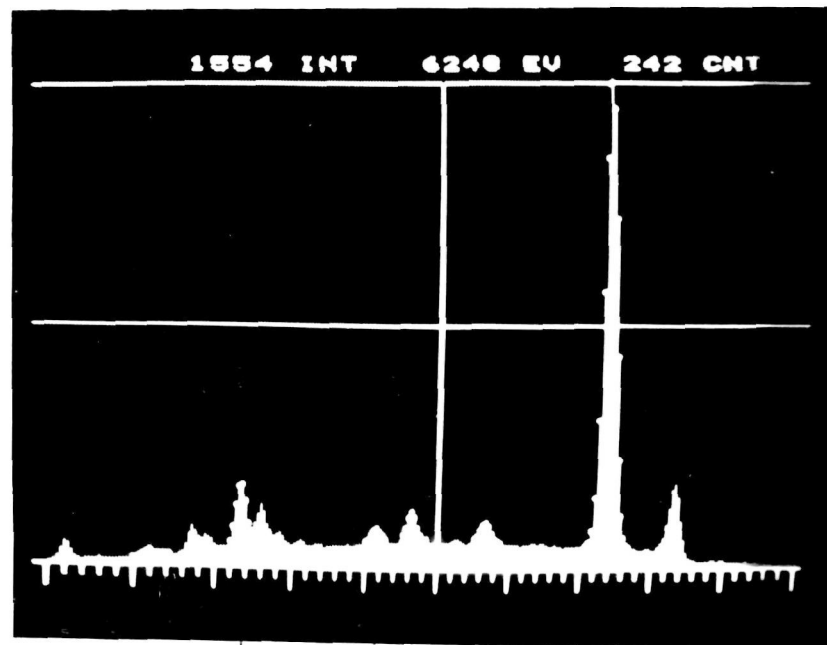
↑ ↑ ↑ ↑ ↑ ↑
 BiM_L SbL_L CrK_L MnK_L CoK_L ZnK_L

Fig. 3.24
(a)



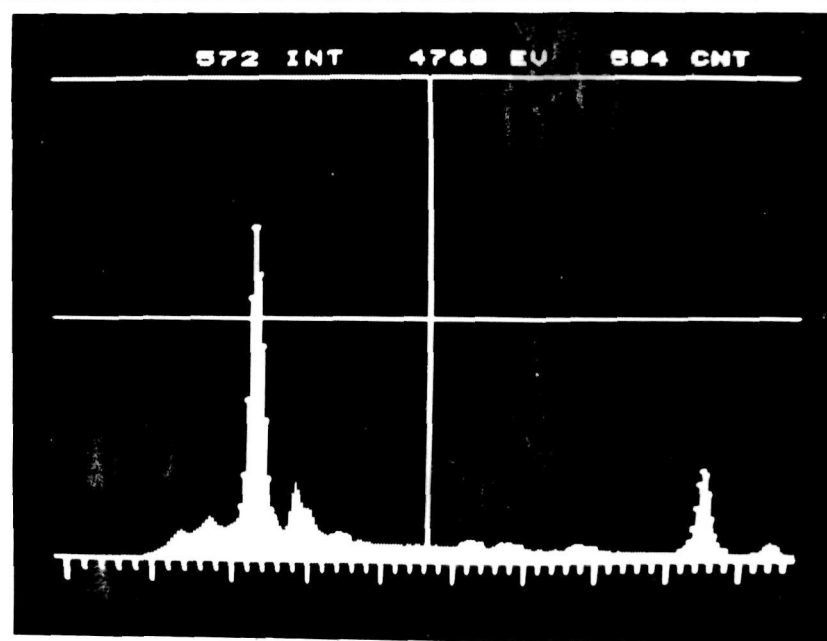
↑ ↑ ↑ ↑ ↑ ↑
 BiM_L SbL_L CrK_L MnK_L CoK_L ZnK_L

(b)



(c)

↑ ↑ ↑ ↑ ↑ ↑
 BiM_x SbL_x CrK_x | MnK_x CoK_x ZnK_x



(d)

↑ ↑ ↑ ↑ ↑ ↑
 BiM_x SbL_x CrK_x | MnK_x CoK_x ZnK_x

Fig. 3.24 : Energy dispersive analysis of X-rays (EDAX) spectra for a (ZBSCMCo) pellet sintered at 1300°C, electron probe on-(a) total surface area covered in fig.3.23, (b) big grain, (c) small grain, (d) intergranular layer.

Table 3.32 : EPMA results of ZBSCMCr pellet sintered at 1300°C
at various places

Place of analysis	INTEGRAL					INTEGRAL RATIO					
	ZnK α	BiM α	SbL α	CoK α	MnK α	CrK α	Zn/Bi	Zn/Sb	Zn/Co	Zn/Mn	Zn/Cr
Total surface area covered in fig. 3.23	2,99,595	45,202	7,153	4,406	2,142	1,248	6.62	41.88	68.00	139.86	240.04
Probe on a big grain	3,26,056	9,062	22	3,830	942	8	35.98	14821	84.04	346.1	40757
Probe on a small grain	2,24,631	6,839	89,327	8,185	13,208	8,385	32.85	2.51	27.44	17.01	26.79
Probe on an inter-granular layer.	1,63,634	328,026	947	546	224	6,125	0.5	172.79	299.70	730.51	26.00

The intergranular layer is very rich in bismuth and a small amount of Zn, Cr, Sb and a very small amount of Co and Mn. It has been also observed from the SEM micrograph (fig. 3.23) that these small grains are situated mostly at the intergranular layers but some are even on big grains, and these small grains are also coated with Bi_2O_3 rich layers.

For a detailed study of this system, pellets sintered at various temperatures are examined by SEM and EPMA techniques. The scanning electron micrographs for various sintering temperatures are given in fig. 3.25. The SEM micrographs clearly show that the grain growth increases slowly upto 825°C , more rapidly between $900-1000^\circ\text{C}$ and reaches a maximum in the range $1200^\circ-1400^\circ\text{C}$. The measured grain size is given in table 3.28, comparing the grain sizes obtained under similar conditions for the ZBC and ZBSCMcr systems. It is clearly seen that by adding other oxides in the ZBC system, the grain size has reduced approximately to half. From the SEM micrographs it is clearly seen that the formation of big grains, intergranular layer and small grains starts from the sintering temperature of 1000°C and at 1300°C it shows clear formation of intergranular layer around the big grains and also around the small grains. However at the sintering temperature of 1400°C , this intergranular layer disappears but still small and big grains remains in the microstructure. This disappearance of the intergranular layer is due to the loss of Bi_2O_3 by evaporation at 1400°C .

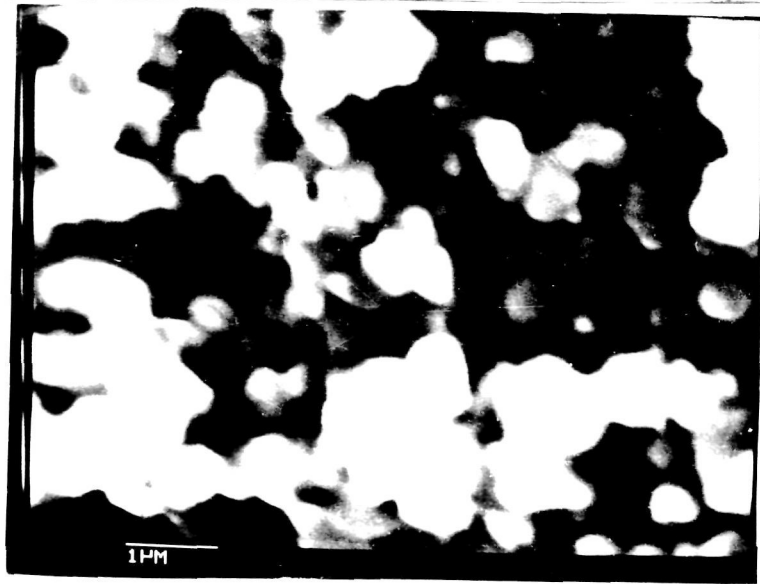
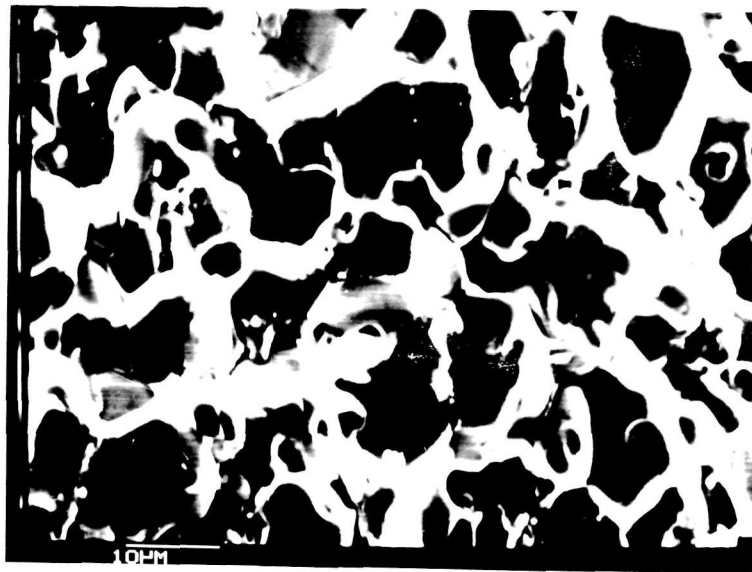
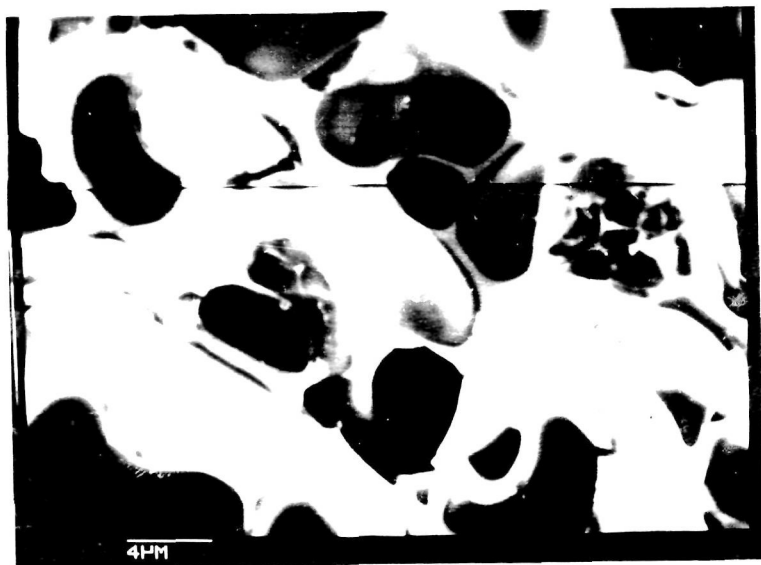


Fig. 3.25
(a)



(b)



(c)



(d)



(e)

Fig. 3.25 : Scanning electron micrographs of the (ZB30MCr) pellets sintered at (a) 825^oC (b) 1000^oC (c) 1200^oC (d) 1300^oC (e) 1400^oC.

The X-ray integrals obtained by EPMA technique for ZBSCMCr pellets sintered at various temperatures are given in table 3.33 and these are in total agreement with the XPS findings.

In short we can conclude that the improvement in the α -value due to addition of the five oxides may probably be due to the fact that the oxides of cobalt and manganese dissolving in ZnO grains thereby changing the electrical conductivity of these grains. Similarly in the intergranular layer of Bi_2O_3 , Sb_2O_3 and Cr_2O_3 might be dissolving therefore its electric conductivity might also be changing. Furthermore some additional small grains are formed from ZnO, Sb_2O_3 , CoO, MnO and Cr_2O_3 at the intergranular layer. All these factors may be improving the non-linear exponent ' α ' value in these systems but this will be well explained by the X-ray diffraction study in the following pages.

3.4.4 X-ray diffraction study

For the ZBSCMCr pellets sintered at different temperatures, the 'd' values were calculated from the X-ray diffraction data and are presented in table 3.34. These data have been compared with the standard X-ray patterns for the different phases and on that basis it has been possible to identify the various phases present. The analysis is presented in table 3.35. The following interesting

Table 3.33 : EPMA results and grain size of the ZBSCMCr sintered at various temperatures.

Sintering temperature °C	Integral						Integral ratio			Grain size (micron)		
	ZnK α	BiM α	SbL α	CoK α	MnK α	CrK α	Zn/Bi	Zn/Sb	Zn/Co		Zn/Mn	Zn/Cr
PM	99,533	7,425	2,360	1,254	516	401	13.00	40.90	76.98	187.08	240.73	< 1
600	1,28,656	11,803	3,785	1,692	714	536	10.90	33.99	76.04	180.19	240.03	< 1
825	1,49,853	17,030	4,075	2,011	893	612	8.80	36.77	74.52	167.81	244.46	< 1
1000	1,65,735	23,103	4,192	2,240	1,108	667	7.17	39.54	73.99	149.58	248.48	8 - 10
1200	1,75,840	25,484	4,399	2,496	1,248	723	7.09	41.05	70.45	144.69	243.21	10 - 15
1300	1,80,579	26,992	4,319	2,627	1,298	750	6.69	41.81	68.74	139.12	240.76	10 - 15
1400	1,93,977	800	3,799	2,891	1,462	798	242.5	51.06	67.10	132.68	243.08	10 - 15

Table 3.34 : XRD results of the Δ BSCr pellets sintered at various temperatures

$d \text{ \AA}$	600°C		825°C		1000°C		1200°C		1300°C		1400°C	
	I/I_1	$d \text{ \AA}$	$d \text{ \AA}$	I/I_1	$d \text{ \AA}$	I/I_1	$d \text{ \AA}$	I/I_1	$d \text{ \AA}$	I/I_1	$d \text{ \AA}$	I/I_1
-	-	-	-	-	4.90	1.2	4.90	2.6	4.95	3.4	4.95	1.9
3.23	15.4	3.19	4.8	-	3.19	4.7	3.15	1.1	3.20	0.9	-	-
-	-	-	-	-	3.01	7.0	3.01	5.0	3.03	5.2	3.03	2.5
-	-	-	-	2.99	23.4	3.00	7.0	5.1	3.01	3.2	-	-
2.80	61.5	2.79	59.5	2.79	70.2	2.80	51.2	2.80	52.6	2.81	51.7	2.81
-	-	2.71	3.6	-	-	-	-	-	-	-	-	-
2.67	3.9	-	-	-	-	-	-	-	-	-	-	-
2.59	30.8	2.58	31.0	2.58	28.1	2.59	32.6	2.59	30.3	2.60	34.5	2.61
-	-	-	-	-	-	2.56	10.5	2.56	15.8	2.59	22.4	2.59
2.46	100	2.45	100	2.46	100	2.47	100	2.47	100	2.48	100	2.48
-	-	-	-	-	-	2.13	1.2	2.13	2.6	2.14	3.4	2.14
1.90	19.2	1.90	20.2	1.90	18.7	1.90	18.6	1.90	15.8	1.91	19.0	1.91
-	-	-	-	1.84	7.8	1.84	1.2	1.85	0.8	1.85	0.6	-
-	-	-	-	-	-	-	-	-	-	1.75	0.8	1.75
-	-	-	-	-	-	1.64	2.3	1.64	2.6	1.65	4.3	1.65
1.62	39.0	1.62	39.1	1.62	39.0	1.62	26.0	1.62	31.6	1.63	27.6	1.63
-	-	-	-	1.57	6.2	1.57	5.0	1.58	4.0	1.58	2.0	-
-	-	-	-	-	-	1.51	3.5	1.51	5.2	1.52	5.3	1.52
1.47	23.1	1.47	26.0	1.47	20.3	1.47	18.6	1.48	21.1	1.48	17.2	1.48

Table 3.35 : The crystal phases observed by XRD
in 2BSCMOx pellets sintered at
various temperatures.

Sintering tempe- rature °C	ZnO	α -Bi ₂ O ₃	γ -Bi ₂ O ₃	Pyrochlore	Spinel
PM	VS	W	A	A	A
600	VS	W	A	A	A
825	VS	A	A	M	A
1000	VS	A	W	W	W
1200	VS	A	W	VW	M
1300	VS	A	W	VW	S
1400	VS	A	VVW	A	M

PM - physical mixture
before sintering
VS - very strong
S - strong
M - medium
W - weak
VW - very weak
VVW - very very weak
A - absent

features are worth noting. The α - Bi_2O_3 phase is present upto 600°C and at 825°C the Bi_2O_3 phase is almost absent and a new pyrochlore phase appears. From this it can be concluded that the pyrochlore phase contains all the Bi_2O_3 present in the system. Of the various possible compositions suggested for the pyrochlore phase by Inada [42, 191, 192], the one having the formula $\text{Zn}_2\text{Bi}_3\text{Sb}_3\text{O}_{14}$ appears the most appropriate. This pyrochlore phase was absent in all the three previously studied systems. Therefore to form the pyrochlore phase, the Bi and Sb oxides are required. It is thus likely that the composition of the pyrochlore system is $\text{Zn}_2\text{Bi}_3\text{Sb}_3\text{O}_{14}$ as claimed by Inada [42, 191, 192].

On raising the sintering temperature above 825°C , the pyrochlore phase disproportionates into two phases: bismuth oxide phase as γ - Bi_2O_3 and a spinel phase containing Zn and Sb oxides presumably of the composition $\text{Zn}_7\text{Sb}_2\text{O}_{12}$. It is not clear as to where the other transition metal oxides e.g. CoO , MnO and Cr_2O_3 are present but in view of what has been discussed earlier, they are at least partially present in solid solution with the Bi_2O_3 , whereby the γ -phase has been stabilised. It is also likely that these oxides are present in the form of a solid solution with ZnO and also with the spinel phase. As the temperature is raised the spinel phase increases in concentration at the cost of the pyrochlore phase.

The ZnO 'd' values have been tabulated as a function of the sintering temperature in table 3.36. The calculated 'c' and 'a' values are also given in the table. The lattice parameters remain constant upto a sintering temperature of 1200°C and then it shows a slight increase on sintering at 1300°C and 1400°C.

The spinel 'd' values have also been separately given in table 3.37 as a function of the sintering temperature. The mean lattice constant 'a' calculated from these 'd' values is given separately for each sintering temperature. The 'a' value is constant at 8.51 upto 1200°C and then shows a rise to 8.57 at 1300°C and 1400°C. These values are lower than what has been got for $Zn_7Sb_2O_{12}$ spinel phase in the ZS system. This may imply that this phase contains some smaller radius ions such as Co, Cr and Mn. A similar conclusion is arrived at on the basis of earlier EPMA results.

The 'd' values for the pyrochlore phase have also been separately presented in table 3.38. This phase is absent below 825°C and is present to the maximum extent at 825°C beyond which it gradually decomposes. Only three prominent lines were observed i.e. 222, 440 and 622, but the 2 θ measurements were accurate enough to give a reliable value of the lattice constant. The calculated values for

Table 3.36 : Values of 'd', 'a' and 'c' for the ZnO crystal phase in 2B5CMCr pellets sintered at various temperatures.

hkl	d values $\overset{\circ}{\text{\AA}}$						
	PM	600 $^{\circ}\text{C}$	825 $^{\circ}\text{C}$	1000 $^{\circ}\text{C}$	1200 $^{\circ}\text{C}$	1300 $^{\circ}\text{C}$	1400 $^{\circ}\text{C}$
100	2.796	2.786	2.789	2.800	2.801	2.813	2.813
022	2.587	2.581	2.582	2.587	2.592	2.601	2.606
101	2.461	2.454	2.459	2.465	2.471	2.477	2.481
102	1.902	1.899	1.901	1.901	1.901	1.911	1.906
110	1.620	1.617	1.618	1.620	1.620	1.626	1.626
103	1.474	1.471	1.472	1.474	1.476	1.478	1.478

a $\overset{\circ}{\text{\AA}}$	3.24	3.23	3.24	3.24	3.24	3.25	3.25
c $\overset{\circ}{\text{\AA}}$	5.20	5.19	5.20	5.20	5.20	5.21	5.21

PM - physical mixture
before sintering

Table 3.37 : Values of 'd' and 'a' for the spinel phase in ZBSCMCr pellets sintered at various temperatures.

hkl	d values $\overset{\circ}{\text{A}}$						
	PM	600 $^{\circ}\text{C}$	825 $^{\circ}\text{C}$	1000 $^{\circ}\text{C}$	1200 $^{\circ}\text{C}$	1300 $^{\circ}\text{C}$	1400 $^{\circ}\text{C}$
111	A	A	A	4.897	4.897	4.946	4.946
220	A	A	A	3.003	3.002	3.027	3.033
311	A	A	A	2.561	2.560	2.586	2.588
400	A	A	A	2.133	2.134	2.144	2.140
422	A	A	A	-	-	1.749	1.749
511/333	A	A	A	1.642	1.644	1.651	1.650
440	A	A	A	1.511	1.511	1.517	1.517
$\overset{\circ}{a}$ A	-	-	-	8.51	8.51	8.57	8.57

Table 3.38 : Values of 'd' and 'a' for the pyrochlore phase in ZBSCMCr pellets sintered at various temperatures.

hkl	d values $\overset{\circ}{\text{A}}$						
	PM	600 $^{\circ}\text{C}$	825 $^{\circ}\text{C}$	1000 $^{\circ}\text{C}$	1200 $^{\circ}\text{C}$	1300 $^{\circ}\text{C}$	1400 $^{\circ}\text{C}$
222	A	A	2.988	3.001	3.005	3.005	A
440	A	A	1.838	1.839	1.847	1.847	A
622	A	A	1.570	1.572	1.578	1.578	A
$\overset{\circ}{a}$ A	-	-	10.38 ₅	10.41	10.45	10.45	-

the lattice parameter 'a' are given in the table. This parameter also shows a gradual increase with the sintering temperature. The reported value 10.45 \AA is in good agreement with the value presented here.

It is clear that the pyrochlore phase does not have an important role to play in the non-linear behaviour of this system, because after sintering at 1300°C when this property is most enhanced, the pyrochlore phase is almost absent.

The role of the cubic transition-metal oxide such as CoO and MnO appears to be the most vital as discussed earlier. They tend to stabilise the γ -form of Bi_2O_3 which has the desired property of remaining in the form of a thin coating around the ZnO grains. If this form is not stabilized, Bi_2O_3 crystallised as the α -monoclinic form which tends to segregate as islands. These islands are clearly seen in the scanning electron micrographs of the ZB system.

This now leaves us with the spinel phase, whose useful role is not clear. The same type of spinel phase present in the ZB system had no beneficial effect at all. Even when present along with Bi_2O_3 as in the $\text{ZnO-Bi}_2\text{O}_3\text{-Sb}_2\text{O}_3$ system reported by Iida [46], the non-linear coefficient (α) value had not increased at all.

At the same time the fact remains that this system with five additives has better non-linear property as compared to the simpler cobalt containing system (ZBC) discussed earlier. The presence of spinel phase possibly acts as a grain growth inhibitor, leading to small grains of ZnO as shown by the scanning electron micrograph as compared to ZBC system ZnO grains. Also the grains are seen to be more spherical and of uniform sizes. Such effects are a common consequence of precipitated phases at the grain boundary. They inhibit grain growth during sintering. The decreased crystal size is also seen by the increased line width of XRD peaks in case of these samples sintered at 1300°C.

Although we have no means to know the resistivity of the insulating layer or of the ZnO grains, but it is felt that if the additive increases the resistivity of insulating layer and decreases that of ZnO grains then the varistor characteristics are bound to improve. It is likely that these additional additives help in that direction.

REFERENCES

- [1] C.J. Frosch : Bell Lab. Record, 32 (1964) 33.
- [2] H.F. Diemel : Bell Lab. Record, 34 (1966) 407.
- [3] R. de Proost and N. Servranckx : Electronics, (1961) 68.
- [4] M. Uno : J. Inst. Elect. Commun. Engrs., Japan, 42 (1959) 185.
- [5] M. Uno : Electronics, (1961) 44.
- [6] W.G.P. Lamb : Electron Eng., 37 (1965) 809.
- [7] C. Zener : Proc. Roy. Soc. (London), 145 (1934) 523.
- [8] K.B. McAfee, E.J. Ryder, W. Shockley and M. Sparks : Phys. Rev., 83 (1951) 650.
- [9] G.K. Teal, M. Sparks and S. Buehler : Phys. Rev., 81 (1951) 637.
- [10] F.S. Goucher, G.L. Pearson, M. Sparks, G.K. Teal and W. Shockley : Phys. Rev., 81 (1951) 637.
- [11] W.J. Pietenpol : Phys. Rev., 82 (1951) 120.
- [12] K.G. McKay : Phys. Rev., 94 (1954) 877.
- [13] New Jersey Zinc Co., New York : (1957) 100.
- [14] G. Heiland, E. Mollwo and F. Stoeckmann : Solid State Physics, Vol. 8, Academic Press, New York, (1959) 191.
- [15] W. Jacobowski and D.H. Whitmore : J. Amer. Ceram. Soc., 54 (1971) 161.
- [16] R.C. Neville and C.A. Mead : J. Appl. Phys., 41 (1970) 3795.
- [17] K. Hauffe and A.L. Vierk : Z. Phys. Chem., 196 (1950) 160.

- [18] T.K. Gupta and R.L. Coble : J. Amer. Ceram. Soc.,
51 (1968) 521.
- [19] S.K. Dutta and R.M. Spriggs : J. Amer. Ceram. Soc.,
53 (1970) 61.
- [20] W. Komatsu, Y. Moriyoshi and N. Seto : Yogyo
Kyokai Shi ; 77 (1969) 347.
- [21] W. Komatsu, H. Ooki, I. Naka and A. Kobayashi :
J. Catal, 15 (1969) 43.
- [22] T.K. Gupta : J. Amer. Ceram. Soc., 54 (1971) 413.
- [23] M. Matsuoka, T. Masuyama and Y. Iida : Japan J.
Appl. Phys., 8 (1969) 1275.
- [24] E.E. Hahn : J. Appl. Phys., 22 (1951) 855.
- [25] S.E. Harison : Phys. Rev., 93 (1954) 52.
- [26] T. Masuyama, and M. Matsuoka : Japan J. Appl. Phys.,
7 (1968) 438.
- [27] W.D. Kingery : Introduction to Ceramics (Wiley,
New York) (1963) 136.
- [28] M. Matsuoka, T. Masuyama and Y. Iida : Proc. 1st
Conf. Solid State Devices, Tokyo, 1969,
Oyts Buturi; J. Japan Soc. Appl. Phys., 39 (1970)
Suppl., p. 94.
- [29] M. Matsuoka : Japan. J. Appl. Phys., 10 (1971) 736.
- [30] M.A. Lampert : Proc. IRE.50 (1962) 1751.
- [31] E.M. Levin, C.R. Roblins and H.F. McMurdie :
Phase Diagrams for Ceramists (Amer. Ceram. Soc.
In., (1964) 127.
- [32] W.G. Morris : J. Amer. Ceram. Soc., 56 (1973) 360.
- [33] R.A. Delaney and H.D. Kaiser : J. Electrochem. Soc.,
114 (1967) 333.
- [34] E.M. Levin and A.S. Roth : J. Res. Nat. Bur. Stand.
Sect A, 68 (1964) 197.
- [35] J.H. Halford and H. Hacker, Jr. : Thin Solid Films
4 (1969) 265.

- [36] J. Wong : J. Amer. Ceram. Soc., 57 (1974) 357.
- [37] A.R. Hutson : J. Phys. Chem. Solids, 8 (1959) 467.
- [38] R. Mensfield : Roy. Proc. Phys. Soc., London, Sect. B, 62 (1949) 476.
- [39] C.N.R. Rao, G.V.S. Rao and S. Ramdas; J. Phys. Chem., 73 (1969) 672.
- [40] J. Wong : J. Appl. Phys., 46 (1975) 1653.
- [41] J. Wong : J. Appl. Phys., 46 (1975) 1827.
- [42] M. Inada : Japan. J. Appl. Phys., 17 (1978) 1.
- [43] M. Inada : Japan. J. Appl. Phys., 17 (1978) 673.
- [44] K. Eda : J. Appl. Phys., 49 (1978) 2964.
- [45] K. Eda : J. Appl. Phys., 50 (1979) 4436.
- [46] Lionel, M. Levinson and H.R. Philipp : J. Appl. Phys., 46 (1975) 1332.
- [47] Lionel, M. Levinson and H.R. Philipp : J. Appl. Phys., 47 (1976) 3116.
- [48] H.R. Philipp and L.M. Levinson : J. Appl. Phys., 47 (1976) 3177.
- [49] L.M. Levinson and H.R. Philipp : J. Appl. Phys., 47 (1976) 1117.
- [50] L.M. Levinson and H.R. Philipp : Appl. Phys. Lett., 24 (1974) 75.
- [51] J.D. Levine, C.R.C. Critical Reviews in Solid State Sciences, 5 (1975) 597.
- [52] J.T.C. Van Kemenade and A.K. Eijthaven, Ber. Dt. Keram. Ges., 52 (1975) 243.
- [53] L.M. Levinson and H.R. Philipp : J. Solid State Chem., 12 (1975) 292.
- [54] H.R. Philipp and L.M. Levinson; : J. Appl. Phys., 46 (1975) 3206.
- [55] J. Bernasconi, H.P. Klein, B. Knecht and S. Strassler : J. Electronic Materials, 5 (1976) 473.

- [56] J. Bernasconi, S. Strassler, B. Knecht, H.P. Klein and A. Menth : Solid State Commun., 20 (1976) 1052.
- [57] W.G. Morris, J. Vac. Sci. Technol., 13 (1976) 926.
- [58] J. Bernasconi, S. Strassler, B. Knecht, H.P. Klein and A. Menth., Solid State Commun., 21 (1977) 867.
- [59] K. Mukae, K. Tsuda and I. Nagasawa : Japan. J. Appl. Phys., 16 (1977) 1361.
- [60] R. Einzinger : Applications of Surf. Sci., 1 (1978) 329.
- [61] G.D. Mahan, L.M. Levinson and H.R. Philipp : Appl. Phys. Letters, 33 (1978) 830.
- [62] J.T.C. Van Kemenade and K.K. Eynthoven : Ber. Deutsch. Keram. Ges., 55 (1978) 330.
- [63] R. Einzinger : Application of Surf. Sci., 3 (1979) 390.
- [64] P.L. Hower and T.K. Gupta : J. Appl. Phys., 50 (1979) 4847.
- [65] K. Uda : J. Appl. Phys., 50 (1979) 4436.
- [66] F.A. Selim, T.K. Gupta, P.L. Hower and W.G. Carlson : J. Appl. Phys., 51 (1980) 765.
- [67] L.K.J. Vandamme and J.C. Brugman : J. Appl. Phys., 51 (1980) 4240.
- [68] K. Siegbahn, C. Nording, A. Fahlman, R. Nordberg, K. Hamrin, J. Hedman, G. Johansson, T. Bergmark, S.E. Karlsson, I. Lindgren and B. Lindberg : ESCA - Atomic, Molecular and Solid State Structure by means of Electron Spectroscopy, Almqvist and Wiksell, Uppsala, 1967.
- [69] H. Ibach, ed., Electron spectroscopy for surface analysis (Springer, Berlin, 1977).
- [70] P.F. Kane and G.A. Larrabee : eds., Characterization of Solid Surfaces (Plenum Press, New York, 1974).
- [71] J.M. Blakely, ed., : Surface Physics of Materials, (Academic Press, New York 1975).

- [72] C.A. Evans, Jr., : Anal Chem., 47 (1975) 818 A.
- [73] A.W. Czanderna, ed., : Methods and Phenomena, Methods of Surface Analysis, Vol. 1 (Elsevier, Amsterdam, 1975).
- [74] M. Prutton, : Surface Physics (Oxford Univ. Press, London, 1976).
- [75] J. Oudar : Physics and Chemistry of Surfaces, (Blackie, Glasgow, 1975).
- [76] V.D. Frechette, W.C. Lacourse and V.L. Burdick, eds., : Surfaces and Interfaces of Glass and Ceramics (Plenum, New York, 1974).
- [77] A.D. Baker, M.A. Brisk and D.C. Liotta, : Anal. Chem., 48 (1976) 281k.
- [78] D.M. Hercules : Anal. Chem., 48 (1976) 294R.
- [79] P.F. Kane and G.B. Larrabee : Anal. Chem., 49 (1977) 221k.
- [80] Surface Properties of Materials, Proc. Conf. on Surface Properties of Materials; Surface Sci., 48 (March 1975).
- [81] A General Discussion on Electron Spectroscopy of Solids and Surfaces; Faraday Discuss. Chem. Soc., 60 (1975).
- [82] Electron Spectroscopy, Progress in Research and Applications, Proc. Intern. Conf. Electron Spectry., relat. Phenom, 5 (1974).
- [83] T.A. Carlson : Photoelectron and Auger Spectroscopy (Plenum Press, New York 1975).
- [84] Proc. Third Annual Conf. Physics of Compound Semiconductor Interfaces; J. Vacuum Sci. Technol., 13 (1976) 749.
- [85] K.F.J. Heinrich and D.B. Newbury, eds., : Secondary Ion Mass Spectrometry (U.S. N.B.S. Special Publication, 427, Washington, D.C., 1975).
- [86] D.M. Hercules : Anal. Chem., 44 (1972) 106R.

- [87] A.D. Baker, M.A. Brisk and D.C. Liotta : Anal. Chem., 50 (1978) 328 R.
- [88] D. Betteridge and M.A. Williams : Anal. Chem., 46 (1974) 125 R.
- [89] D. Betteridge : Anal. Chem., 44 (1972) 100 R.
- [90] D.M. Hercules and J.C. Carver : Anal. Chem., 46 (1974) 133 R.
- [91] P.K. Ghosh, eds., : A Whiff of Photoelectron Spectroscopy (Swarn Press, New Delhi, 1978).
- [92] D. Briggs : Handbook of X-ray and Ultraviolet Photoelectron Spectroscopy, (Heyden, London, 1976).
- [93] A. Einstein : Ann. Physik, 17 (1905) 132.
- [94] P. Auger : C.R. Acad. Sci., 177 (1923) 169.
- [95] H. Robinson and W.F. Rawlinson : Phil. Mag., 28 (1914) 277.
- [96] M. de Broglie : J. de. Phys., 2 (1921) 265.
- [97] R.G. Steinhardt, Jr. and E.J. Serfass, Ann. Chem., 23 (1951) 1585.
- [98] K. Siegbahn : Alpha, Beta and Gamma Ray Spectroscopy, (North-Holland, Amsterdam, 1965).
- [99] C. Nording, E. Sokolowski and K. Siegbahn, Ark. Fys., 13 (1958) 483.
- [100] D.W. Turner and M.L. Al-Joboury, J. Chem. Phys., 37 (1962) 3007.
- [101] K. Maeda, T. Okawa, T. Utsuka and Y. Tada : Proc. Int. Conf. X-ray Opt. Microanal., 6 (1971) 393.
- [102] Y. Baer, G. Busch and P. Cohn : Rev. Sci. Instrum., 47 (1975) 466.
- [103] C.D. Moak, S. Datz, T.A. Carlson : J. Electron. Spectrosc. Relat. Phenom., 6 (1975) 151.
- [104] U. Gelius : J. Electron Spectrosc. Relat. Phenom., 2 (1973) 383.

- [105] J.P. Carrico : Int. J. Mass Spectrosc. Ion Phys.,
11 (1973) 409.
- [106] D. Roy and J.D. Cavette : Electron Spectroscopy
for Surface Analysis (Springer-Verlag,
Heidelberg, 1977) 13.
- [107] K. Siegbahn, C. Nordling and E. Sokolowski :
Proc. Rehovoth Conf. on Nuclear Structure,
ed. by H.J. Lipkin (1957).
- [108] E. Sokolowski : Ark. Fys., 15 (1959) 1.
- [109] S. Hanstrom, C. Nordling and K. Siegbahn : Z. Phys.,
178 (1964) 439.
- [110] J.M. Hollander, D.N. Hendrickson and W.L. Jolly, :
J. Chem. Phys., 49 (1968) 3315.
- [111] J.W. Robinson, ed., : Handbook of Spectroscopy,
Vol. I, Chemical Ruber Company (1975).
- [112] W.E. Schwartz : Anal. Chem., 45 (1973) 788 A.
- [113] M. Klasson, J. Hedman, A. Berndtsson, R. Nilsson,
C. Nordling and P. Melnik : Phys. Soc.,
5 (1972) 93.
- [114] I. Lindau and W.E. Spicer : J. Electron Spectrosc.,
3 (1974) 409.
- [115] Vinikka, Leva, Larsson, Seven : J. Electron
Spectrosc. Relat. Phenom., 7 (1975) 163.
- [116] F.G. Santibanez and T.A. Carlson : Phys. Rev. B,
12 (1975) 965.
- [117] F.R. McFeely, S.P. Kowalczyk, L. Ley, D.A. Shirley :
Phys. Lett. A ; 49A (1974) 301.
- [118] S.P. Kowalczyk, F.R. McFeely, L. Ley and D.A. Shirley :
AIP Conf. Proc., 24 (1974) 207.
- [119] B. Wallbank, C.E. Johnson, I.G. Main : J. Phys. C.,
6 (1973) 493.
- [120] L. Yin, I. Adler, T. Tsang, L.J. Matienzo, and
S.O. Grim : Chem. Phys. Lett., 24 (1974) 81.

- [121] Marion A. Brisk and A.D. Baker : J. Elect. Spectrosc.,
Relat. Phenom., 7 (1975) 81.
- [122] D.C. Frost, C.A. McDowell and R.L. Tapping :
J. Electron Spectrosc. Relat. Phenom.,
6 (1975) 347.
- [123] K.S. Kim : Phys. Rev. B., 11 (1975) 2177.
- [124] G.K. Werthiem and A. Rosencwaig : Phys. Rev.
Lett., 26 (1971) 1179.
- [125] D.P. Spears, H.J. Fishbeek and T.A. Carlson :
Phys. Rev., 49 (1974) 1603.
- [126] F. wuilleumier and M.O. Krause : Phys. Rev.,
A10 (1974) 242.
- [127] R.A. Pollak, L. Ley, F.R. McFeely, S.P. Kowalczyk
and D.A. Shirley : J. Electron Spectros.,
3 (1974) 381.
- [128] K. Siegbahn, D. Hammond, H. Fellner-Feldegg and
E.F. Bennett : Science, 176 (1972) 245.
- [129] G.J. Leigh and W. Bremser : J. Chem. Soc. Dalton,
(1972) 1216.
- [130] C.K. Jorgensen,; Chimia, 25 (1971) 213.
- [131] D.N.D. Buchanan, M. Robinsons, H.J. Guggenheim,
G.K. Wetheium and V.C. Lambrecht :
Solid State Commun., 9 (1971) 583.
- [132] D.T. Clark, D.B. Adams and D. Briggs : Chem. Commun.,
(1971) 602.
- [133] D.P. Murtha and R.A. Walton,; Inorg. Chem.,
12 (1973) 368.
- [134] B.C. Lane, J.E. Laster and F. Basolo : Chem.
Commun., (1971) 1618.
- [135] S.O. Grim, L.J. Matienzo and W.E. Swartz :
J. Amer. Chem. Soc., 94 (1972) 5116.
- [136] D. Cohen and J.E. Lester : Chem. Phys. Lett.,
18 (1973) 108.
- [137] M.V. Zeller and R.G. Hayes : J. Amer. Chem. Soc.,
95 (1973) 3855.

- [138] K.L. Cheng, J.C. Carver and T.A. Carlson :
Inorg. Chem., 12 (1973) 1702.
- [139] I. Adams, J.M. Thomas, G.M. Bancraft, K.D. Butler
and M. Barber : J. Chem. Soc. Chem. Commun.,
1972) 751.
- [140] P.A. Grutsch, M.V. Zeller and T.P. Fehlner :
Inorg. Chem., 12 (1973) 1431.
- [141] F. Holsboer, W. Beck and H.D. Bartunik :
Chem. Phys. Lett., 18 (1973) 217.
- [142] F.R. McFeely, S. Kowalczyk, L. Ley, R.A. Pollak
and L.A. Shirley : Phys. Rev., B7 (1973) 5228.
- [143] J.W. Lauher and J.E. Lester : Inorg. Chem.,
12 (1973) 244.
- [144] D.A. Huchital and A.T. McKeon : Appl. Phys. Lett.,
20 (1972) 158.
- [145] H.I. Taylor, J.P. Coad and R.J. Brook : J. Amer.
Cer. Soc., 57 (1974) 539.
- [146] J.P. Coad, J.C. Riviere, M. Guttmann and R.P. Krehe :
Acta Met., 25 (1977) 161.
- [147] H.E. Bishop and J.C. Riviere : Acta Met., 18 (1970)
813.
- [148] H. Fellner-Feldegg, U. Gelius, B. Wannberg,
A.G. Nilsson, B. Basilier and K-Siegbahn :
J. Electron Spectrosc., 5 (1974) 643.
- [149] A. Barrie : Instrumentation for electron spectro-
scopy in handbook of X-ray and ultraviolet
photoelectron spectroscopy, ed. by D. Briggs,
Heyden and Sons, London, (1977) 104.
- [150] K. Maeda and T. Ihara : Rev. Sci. Instr.,
42 (1971) 1480.
- [151] S. Aksela : Rev. Sci. Instrum., 42 (1971) 810.
- [152] B. Wannberg, G. Engdahl and A. Skolleremo :
J. Elect. Spectrosc., 9 (1976) 111.
- [153] M.M. Gellender and A.D. Baker : J. Elect. Spectrosc.,
4 (1974) 249.

- [154] I. Lindau, J.C. Helmer and J. Uebbing : Rev. Sci. Instrum., 44 (1973) 265.
- [155] H. Hotop and G. Hubler : J. Elect. Spectrosc., 11 (1977) 101.
- [156] G. Johansson, J. Hedman, A. Berndtsson, M Klasson and R. Nilsson : J. Electron Spectrosc., 2 (1973) 295.
- [157] M. Von Ardenne : Z. Phys., 109 (1938) 553.
- [158] V.K. Zworykin, J. Hillier and H.L. Shyder : ASTM Bull., 117 (1942) 15.
- [159] C.W. Oatley and T.E. Everhart : J. electron., 2 (1957) 668.
- [160] T.E. Everhart and R.F.M. Thornley : J. Sci. Instr., 37 (1960) 246.
- [161] R.F.W. Pease and W.C. Nixon : J. Sci. Instr., 42 (1965) 81.
- [162] A.N. Crewe, D.N. Eggenberger, J. Wall and L.M. Welter : Rev. Sci. Instr., 39 (1968) 576.
- [163] A.N. Broers : Rev. Sci. Instr., 40 (1969) 1040.
- [164] J. Philibert and H. Tixier : Micron, 1 (1969) 174.
- [165] D.G. Coates : Phil. Mag., 16 (1967) 1179.
- [166] K.F.J. Heinrich, C.W. Fiori and H. Yakowit : Science, 167 (1970) 1129.
- [167] H. Ahmed and A.N. Broers : J. Appl. Phys., 43 (1972) 2185.
- [168] A.N. Broers : J. Vac. Sci. Technol., 10 (1973) 979.
- [169] D.E. Newbury and H. Yakowitz : Phys. Stat. Sol. a, 20 (1973) 535.
- [170] A.R. Dinnes : in Scanning Electron Microscopy Systems and Applications 1973, Conference Series 18, Institute of Physics, London, (1973) 76.
- [171] A.N. Broers : in Scanning Electron Microscopy, IITAI, Chicago, Illinois (1974) 9.
- [172] D.E. Newbury and H. Yakowitz : Phys. Stat. Sol. a, 22 (1974) 609.

- [173] C.E. Fiori, H. Yakowitz and D.E. Newbury :
in Scanning Electron Microscopy, IITRI,
Chicago, Illinois, (1974) 167.
- [174] N.C. Yew and D.E. Pease : in Scanning Electron
Microscopy, IITRI, Chicago, Illinois, (1974) 191.
- [175] J. Lebledzik, K.G. Bukre, S. Troutman, G.G.
Johnson, Jr., and E.W. White : in Scanning
Electron Microscopy, IITRI, Chicago,
Illinois (1974) 121.
- [176] R. Castaing and A. Guinier, : in Proceedings of
the 1st International Conference on Electron
Microscopy (1950) 60.
- [177] V.E. Cosslett and P. Duncumb : Nature, 177 (1956)
1172.
- [178] L.S. Birks and E.J. Brooks : Rev. Sci. Instr.,
28 (1957) 709.
- [179] R.M. Fisher and J.C. Schwarts : J. Appl. Phys.,
28 (1957) 1377.
- [180] M.E. Haine and T. Mukey : J. Sci. Instr.,
26 (1959) 350.
- [181] R. Castaing : in Advances in Electronics and
Electron Physics, 13 (1960) 137.
- [182] H. Yakowitz : J. Metals, 15 (1963) 763.
- [183] B.L. Henke : in Advances in X-ray Analysis,
Vol. 7, Plenum Press, New York, (1964) 460.
- [184] R. Fitzgerald, K. Keil and K.F.J. Heinrich,
Science, 159 (1968) 528.
- [185] D.H. Beaman and J.A. Isasi : Anal. Chem.,
42 (1970) 1540.
- [186] J. Wong and W.G. Morris : Amer. Ceram. Soc. Bull.,
53 (1974) 816.
- [187] J. Wong : J. Appl. Phys., 51 (1980) 4453.
- [188] J.E. Castle and D. Epler : Proc. Roy. Soc. London A,
339 (1974) 49.
- [189] C.R. Brundle and A.D. Baker : in Electron Spectroscopy
Vol. II, Academic Press, London (1979).

- [190] A.F. Orchard and G. Thornton : J. Chem. Soc. Dalton, (1977) 1238.
- [191] M. Inada : Japan J. Appl. Phys., 18 (1979) 1439.
- [192] M. Inada : Japan J. Appl. Phys., 19 (1980) 409.
- [193] S.R. Sainkar, S. Badrinarayanan, S.K. Date and A.P.B. Sinha, : Surface and Interface Anal., 3 (1981) 142.
- [194] S.R. Sainkar, S. Badrinarayanan, S.K. Date and A.P.B. Sinha : Appl. Phys. Lett., 39 (1981) 66.

S U M M A R Y

In this work, metal oxide varistors have been prepared by the usual ceramic technique and investigated by photoelectron spectroscopy to find out the reasons of their unusual non-linear I-V characteristics. The metal oxide varistor is a two electrode zinc oxide based ceramic (ZnO with small addition of other oxides such as Bi₂O₃, Sb₂O₃, CoO, MnO, Cr₂O₃) device, with a highly non-linear I-V characteristic similar to back-to-back Zener diodes, but with much higher current and energy handling capabilities. These varistors are widely used in electronic circuits for absorption of transient surges and voltage stabilization.

The non-linear I-V characteristic is expressed by $I = (V/C)^\alpha$ where α is the non-linearity exponent, V is the voltage applied across the varistor body, I is the current flowing through it and C is a constant.

Although ZnO containing five additives gives a better α -value, it was considered desirable to start with a simpler system like ZnO containing single additive and then go over to the study of more complicated five additives systems. For this study four different varistor systems were prepared and investigated by XPS technique. Complementary studies by other techniques such as SEM, EPMA and

XRD have also been conducted and these studies have revealed some interesting features which are summarized in the following paragraphs.

(1) ZnO + Bi₂O₃ (ZB) VARISTOR SYSTEM

These ZB varistor pellets were sintered at various temperatures from 600 to 1400°C and I-V characteristics were measured at room temperature. The maximum α -value of 6.5 was obtained on sintering at 1300°C. The maximum density of 92.8 % was obtained at 1300°C. It has been found that the sintering and densification of pellet are important to get the maximum α -value. The XPE spectra of ZB pellets before and after sintering at various temperatures were recorded. The intensity of the Bi XPE peaks increases whereas of the Zn XPE peaks decreases due to sintering which confirms the migration of Bi₂O₃ to ZnO surface. Similar results were obtained from the fractured surface as well as from the powder samples which confirms that the Bi₂O₃ migration is not a bulk process but it is taking place at the grain boundaries of the ZnO grains. The SEM micrographs also show the big grains clearly separated by a thin layer. It was confirmed from the EPMA results that big grains belong to ZnO and the intergranular layer is rich in Bi₂O₃. No binding energy shifts in Bi

and Zn XPS peaks were observed. Similarly no extra lines were obtained in the XRD patterns which confirm no new phase has been formed after sintering. The ZnO is a good electrical conductor and the Bi_2O_3 is a highly resistive material. The voltage applied to this ZB varistor pellet is therefore concentrated at the highly resistive Bi_2O_3 intergranular layers, which is responsible for the non-ohmic property of these varistors. From the XPS, SEM and EPMA studies for the ZB pellets sintered at various temperatures, the dependence of α on the thickness of the intergranular layer is established. From the above studies the migration of Bi_2O_3 to ZnO grain boundary plays an important role to achieve the unusual non-linear property which is experimentally supported.

(2) ZnO + Sb₂O₃ (2S) VARISTOR SYSTEM

In this system the maximum α -value upto four only was obtained. Furthermore the density achieved is only 77 % on sintering at 1200°C as against 92.8 % obtained for the ZB pellets. This indicates that Bi_2O_3 is helping more in sintering and densification than Sb_2O_3 .

Contrary to the earlier observations, migration of Sb_2O_3 on ZnO grains starts even at 500°C which is maximum at 660° and again reduces above 800°C as observed by the XPS, SEM and EPMA results. Unlike Bi_2O_3 the decrease in

Sb-3d_{3/2} peak intensity is due to the diffusion into the ZnO grains and not due to the evaporation of Sb₂O₃ from the surface. The Sb-3d_{3/2} binding energy changed from 539.2 to 540 eV above 800°C. This shift of 0.8 eV confirms that the antimony changes from Sb³⁺ to Sb⁵⁺. Extra lines were observed in the XRD patterns for pellets sintered above 800°C. The extra lines are attributed to the formation of a spinel type compound with 'a' value equal to 8.577 Å. Two spinel type compounds namely ZnSb₂O₄ with Sb³⁺ and Zn₇Sb₂O₁₂ with Sb⁵⁺ were reported. Using the XPS binding energy data, the new phase is identified to be Zn₇Sb₂O₁₂ spinel.

(3) ZnO + Bi₂O₃ + CoO (ZBC) VARISTOR SYSTEM

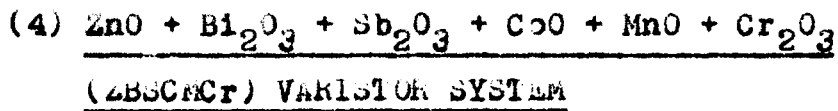
The α-value has improved from 6.5 to 25 in this system by just adding CoO to the ZB system. After sintering at 825°C the density reached 90.3 % of the theoretical density whereas for the ZB pellets the value was only 57.8 %. It is therefore concluded that the CoO also helps in sintering and the liquid phase sintering starts at a lower temperature.

In this system also the migration of Bi₂O₃ to the ZnO grain-boundary was observed by the XPS, SAM and EPMA studies. However, unlike Bi₂O₃, CoO is not migrating at grain boundary but it is found to go into the ZnO phase

during sintering. In this system also no binding energy shift of Zn and Bi XPS peaks was observed thereby confirming that no valency change of Zn or Bi had taken place after sintering.

The SEM micrograph of the ZBC pellet sintered at 1300°C shows the Bi₂O₃ migration to ZnO grain-boundary more clearly. This confirms the beneficial role of CoO on the intergranular layer which is the main reason for the improvement in the α -value.

The ZnO and Y-Bi₂O₃ phases were identified by the XRD. The α -Bi₂O₃ converts to the Y-Bi₂O₃ even at 600°C much below the melting point. The CoO is dissolved in the ZnO and plays the vital role in stabilizing the Y-Bi₂O₃ which is required for the varistor property.



In these varistor pellets the highest α -value equal to 50 was obtained on sintering at 1300°C by adding Sb₂O₃ + MnO + Cr₂O₃ in the previous ZBC system. The value of the constant 'C' has increased from 48 to 135 V/mm in this system.

The XPS results confirmed the migration of Bi₂O₃ and Sb₂O₃ to the intergranular layer as in the ZB, ZS and ZBC

systems. The XPS peaks for other oxides of Co, Mn and Cr were not detected even at the highest sensitivity, thereby it is concluded that these oxides are not migrating on the grain boundary.

Small grains of size 1-4 microns in addition to the large grains and intergranular layer were observed in the SEM micrographs of ZBSCr pellets sintered at 1300°C. From EPMA results it is clearly seen that big grains consist of ZnO with small addition of Co, Mn and Bi oxides, whereas smaller grains consist of large amount of Sb, Co, Mn and Cr and small amount of Bi. The intergranular layer is very rich in Bi with a small amount of Zn, Cr, Sb and much smaller amount of Co and Mn.

The ZnO, α -Bi₂O₃, γ -Bi₂O₃, pyrochlore and spinel phases were identified by the XRD. The α -Bi₂O₃ phase is present upto 600°C. At 825°C the Bi₂O₃ phase is almost absent and a new pyrochlore phase appears with the possible chemical composition Zn₂Bi₃Sb₃O₁₄. This phase was absent in all the three previously studied systems. Above 825°C the pyrochlore phase disproportionates into two phases : γ -Bi₂O₃ and Zn₇Sb₂O₁₂ spinel phase. As temperature is raised, the spinel phase increases in concentration at the cost of the pyrochlore phase. This pyrochlore phase does not have any important role to play in the non-linear

behaviour of this system because the highest α -value was obtained in the pellet sintered at 1300°C where this phase is almost absent. The presence of spinel phase possibly acts as a grain growth inhibitor, leading to the small grains of ZnO shown in the SEM micrographs. The other transition metal oxides, CoO, MnO and Cr₂O₃ are most vital to stabilise the Y-Bi₂O₃ which is the desired phase and remains in the form of a thin coating around the ZnO grains. These additives presumably increase the resistivity of the insulating layer and decrease that of ZnO grains due to which the varistor characteristics improve.

APPENDIX - I

List of publications of
S.R. Sainkar

- [1] X-ray photoelectron spectroscopic studies on ZnO-Bi₂O₃ varistors. Surface and Interface Analysis, 3 (1981) 142.
- [2] X-ray photoelectron spectroscopic studies on ZnO-Sb₂O₃ varistors. Applied Physics Letters, 39,1 (July 1981) 65.
- [3] A study of dilute tin alloys by X-ray photoelectron spectroscopy. J. Electr. Spect. Rel. Phenom., 24 (1981) 19.
- [4] Characterisation of thin films of Bi₂O₃ by X-ray photoelectron spectroscopy. J. Electr. Spect. and Rel. Phenom., (in press).
- [5] Scanning electron microscopic studies on intergranular layers of zinc oxide ceramics. Proceedings of Symposium on Electron Microscopy, Sardar Patel University, Vallabh Vidyanagar (January 1981).
- [6] X-ray photoelectron spectroscopic studies of some solid state devices. Proceedings of Symposium on Surface and Interface Properties in Material Science, Koorkee University, Koorkee (October 1980)
- [7] Effect of near-neighbour interactions on core electron levels in dilute tin alloys : An XPS study. Proceedings of Symposium on Surface and Interface Properties in Material Science, Koorkee University, Koorkee (October 1980).